

***ORIGIN OF SCALE-DEPENDENT
DISPERSIVITY AND ITS IMPLICATIONS FOR
MISCIBLE GAS FLOODING***

Final Scientific/Technical Report
(October 1, 2004 –September 30, 2008)

Steven L. Bryant¹
Russ T. Johns¹
Larry W. Lake¹
Thomas C. Harmon²

29 December 2008

DOE Grant # DE-FC26-04NT15534

¹The University of Texas at Austin
1 University Station
Austin, TX 78712-0228

²The University of California - Merced
P.O. Box 2039
Merced, CA 95344

DISCLAIMER

This report was prepared as an account of work sponsored by an agency of the United States Government. Neither the United States Government, nor any agency thereof, nor any of their employees, makes any warranty, express or implied, or assumes any legal liability or responsibility for the accuracy, completeness, or usefulness of any information, apparatus, product, or process disclosed, or represents that its use would not infringe privately owned rights. Reference herein to any specific commercial product, process, or service by trade name, trademark, manufacturer, or otherwise does not necessarily constitute or imply its endorsement, recommendation, or favoring by the United States Government or any agency thereof. The views and opinions of authors expressed herein do not necessarily state or reflect those of the United States Government or any agency thereof.

ABSTRACT

Dispersive mixing has an important impact on the effectiveness of miscible floods. Simulations routinely assume Fickian dispersion, yet it is well established that dispersivity depends on the scale of measurement. This is one of the main reasons that a satisfactory method for design of field-scale miscible displacement processes is still not available.

The main objective of this project was to improve the understanding of the fundamental mechanisms of dispersion and mixing, particularly at the pore scale. To this end, microsensors were developed and used in the laboratory to measure directly the solute concentrations at the scale of individual pores; the origin of hydrodynamic dispersion was evaluated from first principles of laminar flow and diffusion at the grain scale in simple but geometrically completely defined porous media; techniques to use flow reversal to distinguish the contribution to dispersion of convective spreading from that of true mixing; and the field scale impact of permeability heterogeneity on hydrodynamic dispersion was evaluated numerically.

This project solved a long-standing problem in solute transport in porous media by quantifying the physical basis for the scaling of dispersion coefficient with the 1.2 power of flow velocity. The researchers also demonstrated that *flow reversal* uniquely enables a crucial separation of irreversible and reversible contributions to mixing. The interpretation of laboratory and field experiments that include flow reversal provides important insight. Other advances include the miniaturization of long-lasting microprobes for in-situ, pore-scale measurement of tracers, and a scheme to account properly in a reservoir simulator (grid-block scale) for the contributions of convective spreading due to reservoir heterogeneity and of mixing.

TABLE OF CONTENTS

Disclaimer.....	2
Abstract.....	3
Table of Contents.....	4
Executive Summary.....	5
Results of Work During Reporting Period	
Topic 1: <i>Sensor Development</i>	7
Summary and Conclusions.....	19
Topic 2: <i>Grain-scale origin of hydrodynamic dispersio</i>	22
Summary.....	22
Introduction.....	22
Results.....	29
Discussion.....	34
Summary and Conclusions.....	35
Topic 3a: <i>Flow reversal tracer tests</i>	44
Summary.....	44
Introduction.....	44
Results.....	53
Discussion.....	56
Conclusions.....	57
Topic 3b: <i>Grain-Scale analysis of flow reversal</i>	68
Summary.....	68
Introduction.....	68
Discussion on Local Mixing Mechanism.....	71
Summary and Conclusions.....	75
Topic 4: <i>Impact of reservoir heterogeneity</i>	90
Overview of heterogeneity effect.....	90
Analytical and Numerical Investigation of Heterogeneity	
Discussion.....	97
Introduction.....	97
Results from Continuum Simulations.....	101
Results from Pore-Scale Simulations.....	102
Conclusions.....	106

Origin of Scale-Dependent Dispersivity and Its Implications for Miscible Gas Flooding

Period: October 1, 2004 –September 30, 2008

EXECUTIVE SUMMARY

Dispersive mixing has an important impact on the effectiveness of miscible floods. Despite decades of research into dispersion, it continues to present theoretical and conceptual challenges. Simulations of miscible transport processes generally assume Fickian representations of dispersion in which the dispersivity of the medium is considered constant. However, dispersivity is found to be dependent on the scale of measurement. A satisfactory method for accurate designing and performance prediction of field scale miscible displacement processes is yet to be developed.

The main objective of this project was to perform experimental and computational studies to understand the basic mechanisms of dispersion and mixing at pore scale. The work covered four primary topics: development of microsensors to enable the direct measurement of the solute concentrations at the scale of individual pores; grain-scale evaluation of the origin of hydrodynamic from first principles of laminar flow and diffusion; theoretical evaluation of the effect of flow reversal as a means to distinguish the contribution convective spreading from that of true mixing to dispersion; and numerical evaluation of the field scale impact of permeability heterogeneity on hydrodynamic dispersion.

This project yielded several important results. Foremost is the solution of a long-standing challenge, namely, a physical explanation for the scaling of dispersion coefficient with the 1.2 power of flow velocity. The model discussed in Topic 2 of this

report is the first *a priori* mechanistic prediction of this phenomenon. This represents a significant achievement and is destined to be a landmark in the study of flow and transport in porous media. Another is the demonstration that *flow reversal* enables a crucial separation of irreversible and reversible contributions to mixing. The interpretation of laboratory and field experiments that include flow reversal provides important insight, as described in Topics 3a and 3b in this report. Other advances include the miniaturization of long-lasting microprobes for in-situ, pore-scale measurement of tracers, described under Topic 1, and a scheme to account properly in a reservoir simulator (grid-block scale) for the contributions of convective spreading due to reservoir heterogeneity and of mixing, described under Topic 4.

RESULTS OF WORK DURING REPORTING PERIOD

Topic 1: Sensor Development

1. MINIATURE NITRATE SENSOR DEVELOPMENT AND TESTING

This section describes the efforts aimed at creating a miniature nitrate ion selective electrode (ISE) sensor to support the solute dispersion experiments. ISEs are potentiometric sensors, meaning that they operate by sensing a chemical potential as an electrical potential. ISE sensors have been cast as problematic experimentally due to problems with signal drift (changing calibration) due to surface chemistry changes during the course of a measurement. However, recent advances in materials science and organic chemistry have given rise to new types of conductive organic polymers, which have been used to develop a new generation of ISE-type sensors.

In this work, ISEs were fabricated by electro-polymerization of conducting polymer doped with target ion (nitrate) on a carbon electrode, a well-known method (Hutchins and Bachas, 1995). First, different types of miniaturized ion selective electrodes (ISEs) were created and tested based on conducting polymers doped with nitrate ions were created. Structures for the key chemicals used in this work are shown in Figure 1. One aspect of such ISEs that has not received much attention is their capacity to accurately measure concentrations in flowing water. We characterized this aspect of these sensors and found them to lose sensitivity rapidly in flow-through systems. In order to address the longevity problem, we tried to introduce a double layer-deposited coating process into the fabrication sequence. After attempting several types of layer applications, an insulated layer of bis-3,4-ethylenedioxythiophene (bis-EDOT) was successfully deposited atop the PPy surface in an effort to retain the dopant nitrate anions, which may be lost in flowing water. The resulting sensors exhibited good electrochemical characteristics in the laboratory. Flow-through water and soil-test bed experiments with conductive-polymer based sensors demonstrated that double-layer (Ppy+Bis-EDOT) sensor configuration was successful in improving the stability of the sensor relative to the single-layer sensor's case. However, the double-layer sensors failed to increase the longevity of the sensor beyond 1 or 2 days. Hence, after investigating the literature sources for possibility of using polyvinylchloride-based sensors with different membrane compositions for direct measurement of nitrate levels in soil we decided to change methods and use PVC membrane fabrication technology in order to obtain mini-nitrate-selective electrodes suitable for flow-through experiments.

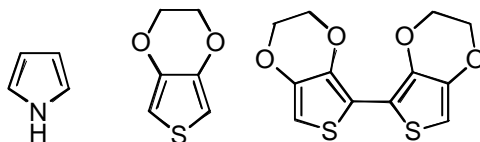


Figure 1. Monomers used in this study to create conducting polymers in single- and double-layer electrodes (L to R: pyrrole, 3,4-ethylenedioxythiophene (EDOT), and bis-3,4-ethylenedioxythiophene (bis-EDOT)).

1.1 Single-Layer (SL) Nitrate Sensors Using Nitrate-Doped Polypyrrole (PPy)

Initial efforts built on the foundational work by the UCM team using electro-polymerization on a carbon substrate to create nitrate sensors (Bendikov et al., 2005; Bendikov and Harmon, 2005a). This section describes the fabrication and calibration of these sensors, and their testing in flow-through systems.

Analytically pure or higher grade reagents purchased from Fisher Scientific or Aldrich Chemicals were used to fabricate and test the nitrate sensors. Pyrrole was refrigerated in the dark and purified by passing through an alumina (Al_2O_3) column. 1×10^{-2} M $(\text{NH}_4)_2\text{SO}_4$ was used as ionic strength adjuster for the preparation of calibration solutions. Deionized water (Millipore, Milli-Q Academic A10 System, 18.3Ω) was used to prepare all standard solutions. Soft mechanical pencil leads (2B, Staedtler 0.5 mm, ~2.5 cm long) were used as the electrode substrate. Electrochemical polymerization was carried out using a potentiostat/galvanostat (Princeton Applied Research, Model 363A). A three-electrode cell was used for preparing the modified electrode based on pencil lead as a working electrode and Ag/AgCl wire and Pt wire as reference and counter electrodes, respectively. Potentiometric measurements were conducted using a handheld multimeter (Fluke Model 111 True RMS). For longevity testing, a commercial data logger (Onset Computer Corp., Model U12) was used to observe in real time and record voltage time series. An Ag/AgCl saturated no-leak electrode (Cypress Systems Inc./ESA Model EE-0009) was used as a reference electrode in potentiometric cells.

Doped PPy electrodes were prepared by binding pencil leads to a segment of a copper wire using a flexible, thin wire. Silver paint was applied to the connection area to guarantee a good contact between pencil lead and copper wire. A 1.5 cm length of the pencil lead was immersed to a 1M pyrrole solution (1.67 g of pyrrole mixed with 25 ml of 10^{-1} M NaNO_3 solution) to perform electrochemical deposition of PPy. The total working (sensitive) surface of the electrode was 0.236 cm^2 . The solution was purged with nitrogen for at least 10 minutes before deposition to remove oxygen. The PPy was electro-polymerized using constant currents ranging from 400 to 700 μA (current densities from 1.69 to 2.97 mA/cm^2 respectively for 20 minutes, about 480-840 mC). After polymerization the electrodes were rinsed with deionized water and placed into a conditioning solution (10^{-2} M NaNO_3) for at least 24 hours prior to testing. Between the measurements electrodes were stored in the dark in 1×10^{-4} M NaNO_3 .

1.2 Double-Layer (PPy-bPEDOT) Nitrate Sensors

The main problem for practical application of PPy films is their environmental stability; PPy based sensors work well for static measurements when stored under optimal conditions, but degrade rapidly in open, flowing systems. In contrast, PEDOT-based perchlorate sensors have exhibited much greater stability (Bendikov and Harmon, 2005b). Unfortunately, our attempts to polymerize EDOT monomer in the presence of nitrate failed to yield usable quantities of PEDOT(NO_3^-). As a substitute for PEDOT, we selected bis-EDOT as an alternative monomeric unit of PEDOT (we refer to the resulting polymer as bPEDOT).

1.2.1 Double-Layer (DL) Nitrate Sensor Fabrication Materials and Method

Bis-(3,4-ethylenedioxythiophene) (bis-EDOT) was synthesized by Ullmann-coupling (Figure 2) using previously reported procedure (Sotzing *et al.*, 1997). To the best of our knowledge, bis-EDOT is the only thiophene derivative known to polymerize with nitrate as an electrolyte. While we were successful in polymerizing bis-EDOT with nitrate as supporting electrolyte, the resulting bPEDOT sensors did not respond to nitrate over a sufficiently broad range of (Figure 2).

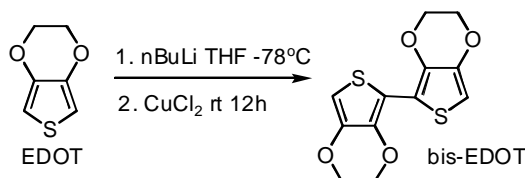


Figure 2. Synthesis of bis-ethylenedioxythiophene (bis-EDOT) after Sotzing *et al.*, (1997), which was subsequently electro-polymerized to yield the conducting polymer bPEDOT.

The inferior quality of the bPEDOT sensors led us to attempt to protect or enhance the PPy-active layer instead of seeking an alternative polymer. More specifically, we hypothesized that the PEDOT layer would protect the PPy-active layer against rapid de-doping and other degradation mechanisms, such as abrasion by environmental media. Considering that PEDOT is known as an environmentally stable polymer (Vazquez *et al.*, 2002), we tried coating the nitrate-doped PPy with PEDOT by polymerizing bis-EDOT with TBA-PF₆ in AcCN. Preliminary testing suggested that the resulting ISE was functional and, in some cases, performed better than single-layer PPy ISE. Given this result, it was decided to further investigate this strategy by first fabricating the nitrate-doped single-layer (hereafter referred to as SL) electrodes, and then polymerizing a layer the nitrate-doped bPEDOT on top of the SL electrode. The resulting PPy-bPEDOT electrode is hereafter referred to as the double-layer (DL) sensor.

The DL electrodes were prepared by first dipping SL electrodes (fabricated as described above) in acetonitrile (AcCN) for 10 seconds to minimize surface water content. The electro-polymerization solution contained 0.1 M tetrabutylammonium nitrate (TBANO₃) and 0.01M bis-EDOT in anhydrous acetonitrile. The coating was performed in nitrate electrolyte using cyclic voltammetry ($E_0 = 0.7 \text{ V}$, $E_1 = 1.1 \text{ V}$, $E_2 = -0.3 \text{ V}$, 10 cycles at scan rate 50 mV/s, $Fc/Fc^+ = 0.34 \text{ V}$) to create a nitrate-doped bPEDOT layer on top of the PPy layer. The resulting electrodes were then rinsed with DI water and conditioned for at least 24 hours in 10^{-2} M NaNO_3 . Figure 3 contains a photograph of a DL sensor and a schematic diagram of its component parts.

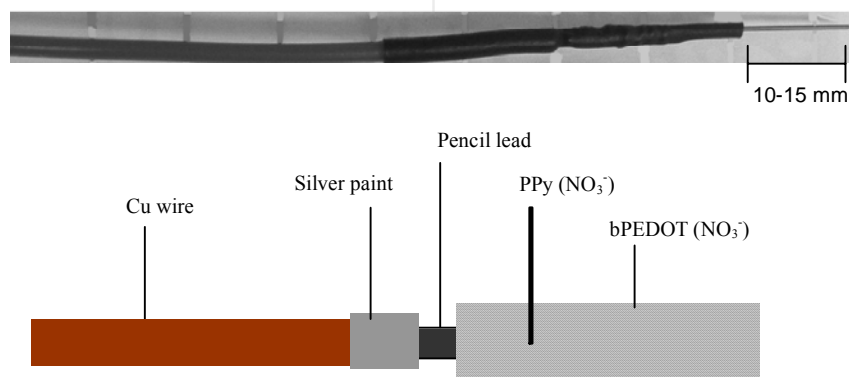


Figure 3. Photograph (top) and schematic representation (b) of the miniature DL nitrate sensor (nitrate-doped PPy coated with a bPEDOT protective sheath).

1.3 SL and DL Sensor Optimization and Calibration Results

Key preliminary results aimed at optimizing the SL and DL sensor fabrication strategies are summarized in Figures 4 and 5. We determined that a DL ISE where the bPEDOT layer was obtained by 20 CV cycles has performance inferior to DL-ISE where the bPEDOT layer was obtained by 10 CV cycles. Scanning electron microscopy (SEM) images taken for both SL and DL (10 cycles) may shed some light on this observation (Figure 4). PPy layer is characterized by a cauliflower-like morphology (Figure 4, top left) while the bPEDOT second layer (Figure 4, top right) appears as isolated zones which do not cover the entire surface and probably allows the movement of ions and preserve its sensitivity. If one compares the thickness of the layers on SEM images (Figure 4, bottom left), PPy layer (650 mC) appears to be about 6 μm while the bPEDOT layer is only about 0.2 μm .

To optimize the electro-polymerization process, we explored the effect of doped PPy sensing layer thickness in both the SL and DL versions of the sensor (Figure 5). The results indicate that the sensor based on bPEDOT alone is only slightly sensitive to nitrate, while the SL sensor with a relatively thick PPy layer (polymerization time 20 min) resulted in the best response over the range of nitrate concentrations tested. After exploring a range of fabrication combinations (PPy electropolymerization time and bPEDOT CV cycles), DL sensor configurations were discovered which did demonstrate comparable responses to the SL sensors, particularly for PPy polymerization times of 15 min or greater.

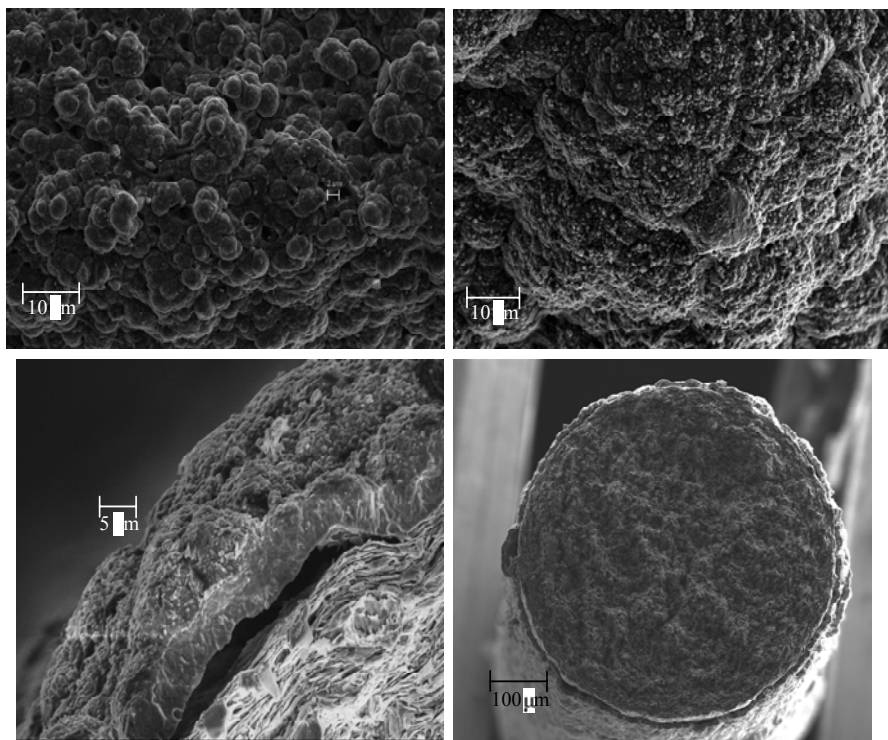


Figure 4. SEM images of pencil lead-based nitrate sensors showing the surface of SL (PPy) (top left) and DL (PPy-bPEDOT) (top right). Higher resolution images of the DL interfaces (bottom left) and a cross-section of a DL on a pencil-lead (bottom right) demonstrate the sensor geometry and the total thickness of the conductive polymer double-layer of about 6 μm .

All SL electrodes were calibrated using standard sodium nitrate solutions, then a subset was prepared for application of the second (bPEDOT) layer described in the following section. Calibration curves for optimized SL and DL sensors are plotted in Figure 6. The electrodes exhibit near-Nernstian response (better than -52 mV/decade change in NO_3^- concentration) with linear range 0.01-100 mM (0.62-6200 ppm) NO_3^- and detection limit $(3\pm 1) \times 10^{-6}$ M (0.124-0.248 ppm). Response times for the electrodes were 30-35 sec at lower nitrate concentrations (0.001 to 1 mM) and less than 20 sec for higher concentrations (1 to 100 mM).

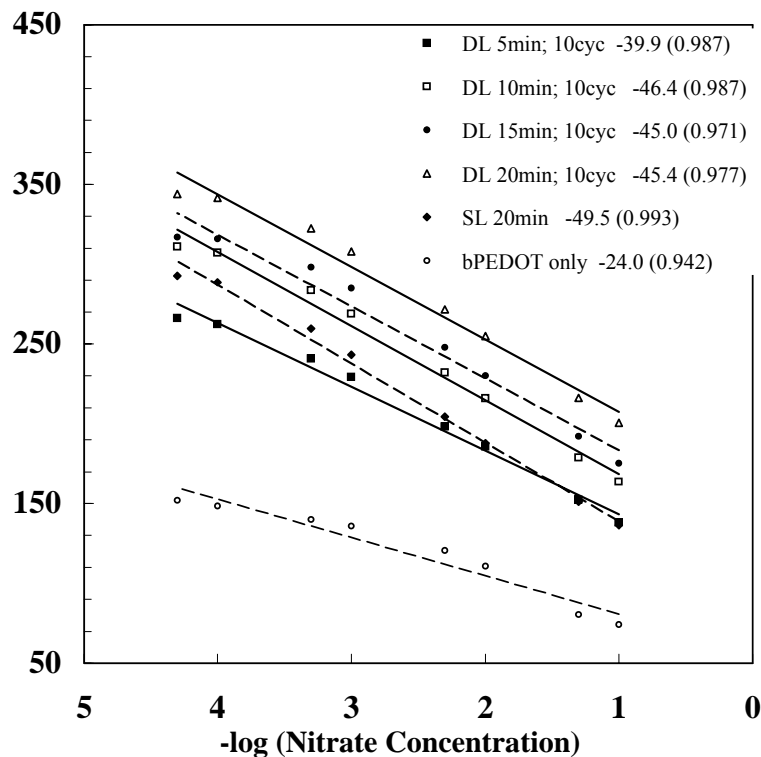


Figure 5. The influence of fabrication technique DL (PPy + bPEDOT) sensor calibrations; SL and bPEDOT-only sensor data are provided for comparison (legend values are (L to R): (1) duration of PPy electro-polymerization, (2) number of CV cycles for bPEDOT layering (for DL sensors), (3) slope of trend line, and (4) correlation coefficient (r^2)).

The stability of SL and DL nitrate sensor prototypes was tested over a period of two months with sensor storage in a 10^{-2} M NaNO_3 solution in the dark between measurements (Figure 7). Both types of sensors continued to respond in a Nernstian manner after two months. The SL appeared to lose some sensitivity at the dilute end of the calibration range. The aged DL exhibited a pronounced shift in response, but otherwise maintained its dynamic range. These results suggest that the addition of the bPEDOT layer may be protecting the underlying PPy layer against degradation over time.

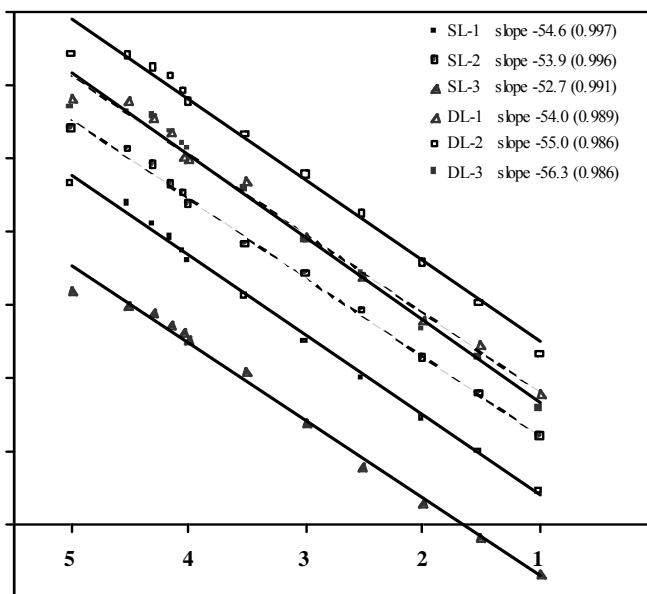


Figure 6. Calibration results for triplicate batches of SL and DL nitrate sensors with optimal fabrication conditions (current density 2.33 mA/cm^2 for 20min PPy electropolymerization for both SL and DL; 10 cyc bPEDOT layer application for DL (note: see appropriate text sections for SL and DL fabrication procedures).

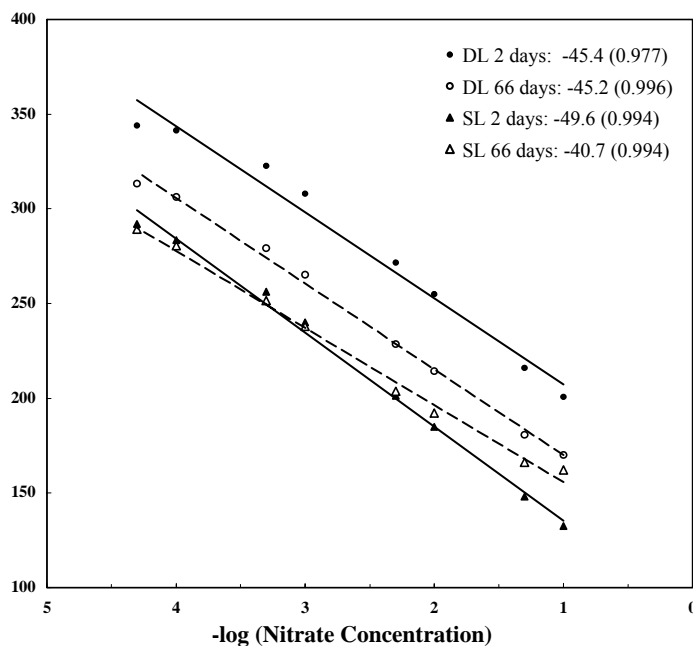


Figure 7. Testing SL and DL sensor stability under optimal storage conditions (room temperature, sealed analyte solution, in the dark); fabrications conditions described in previous figure.

1.4 Results for SL and DL Sensors in Flow-Through Systems

The results for the SL sensor response to pulsed nitrate injections in a flowing stream are plotted in Figure 8. It is worth noting that the flow field for the experiments was three-dimensional and somewhat variable causing poor reproducibility of the injection pulse geometry. Positive responses by the sensors to pulse injections were identified as substantial voltage drops (50 to 100 mV) regardless of the response geometry. Hence, the results reported here should be considered semi-quantitative with the primary intent of the experiments to identify potentially long-lasting sensors (> 3 days) under simulated environmental conditions. The recovery time (period after each spike when the potential of the electrode returns to the baseline value) was approximately 20-30 minutes (depending on the flow rate) for all electrodes suggesting that their response occurred on a shorter timescale than did the dilution rate for the flow-through system. This is evident in the differences in the two early time responses of the sensors to approximately identical to the pulse injections.

Unfortunately, neither the SL nor DL sensor configuration approached the desired longevity. Furthermore, in spite of their strong stability between calibrations, both versions of the sensor exhibited significant calibration drift during the flow-through experiments, demonstrated by the more gradual changes in voltage between spiking events.

In the early stages of the experiment (roughly the first 6 hours), the commercial and SL sensors respond similarly to two pulse injections. The commercial sensors maintain a better baseline potential in the absence of injections, however, with the SL sensors exhibiting significant upward signal drift after the second pulse followed by downward signal drift after about 12 hours. The SL sensor failed to respond to the pulse injection at approximately 19 hours. The passivation of the SL electrodes might be caused by de-doping of PPy matrix in the continuous water stream, or degradation of the PPy polymer. We attempted to analyze both freshly prepared and spent PPy membranes for nitrogen content using transmission electron microscopy (TEM), but could not sufficiently resolve nitrogen levels either samples. Thus, while the extension of longevity caused by the DL method is consistent with either the de-doping or PPy membrane degradation reasons, direct evidence of the passivation mechanism is lacking, and merits additional investigation given that environmental application of such sensors will often be in the context of flowing fluids.

The role of the bPEDOT in extending the stability or longevity of the DL electrodes was also tested in flow-through system (Figure 8). The DL sensor response dynamics differed in this case relative to the SL sensor. First and most importantly, the DL sensor maintained a steady baseline response between pulses and responded well to both nitrate pulses introduced more than 24 h after the start of the flow experiment. This result indicates that the DL configuration was successful in improving the stability of the sensor relative to the SL case. Second, while the DL sensor exhibited a similar voltage drop associated with the pulse nitrate solution injections, it also exhibited a temporary increase in voltage (relative to the baseline response) after the pulse. The SL sensor did not exhibit this latter behavior. The cause of this spike in voltage is unknown and its

duration ranged from roughly 4-6 hours after the first injection to less than an hour in subsequent injections.

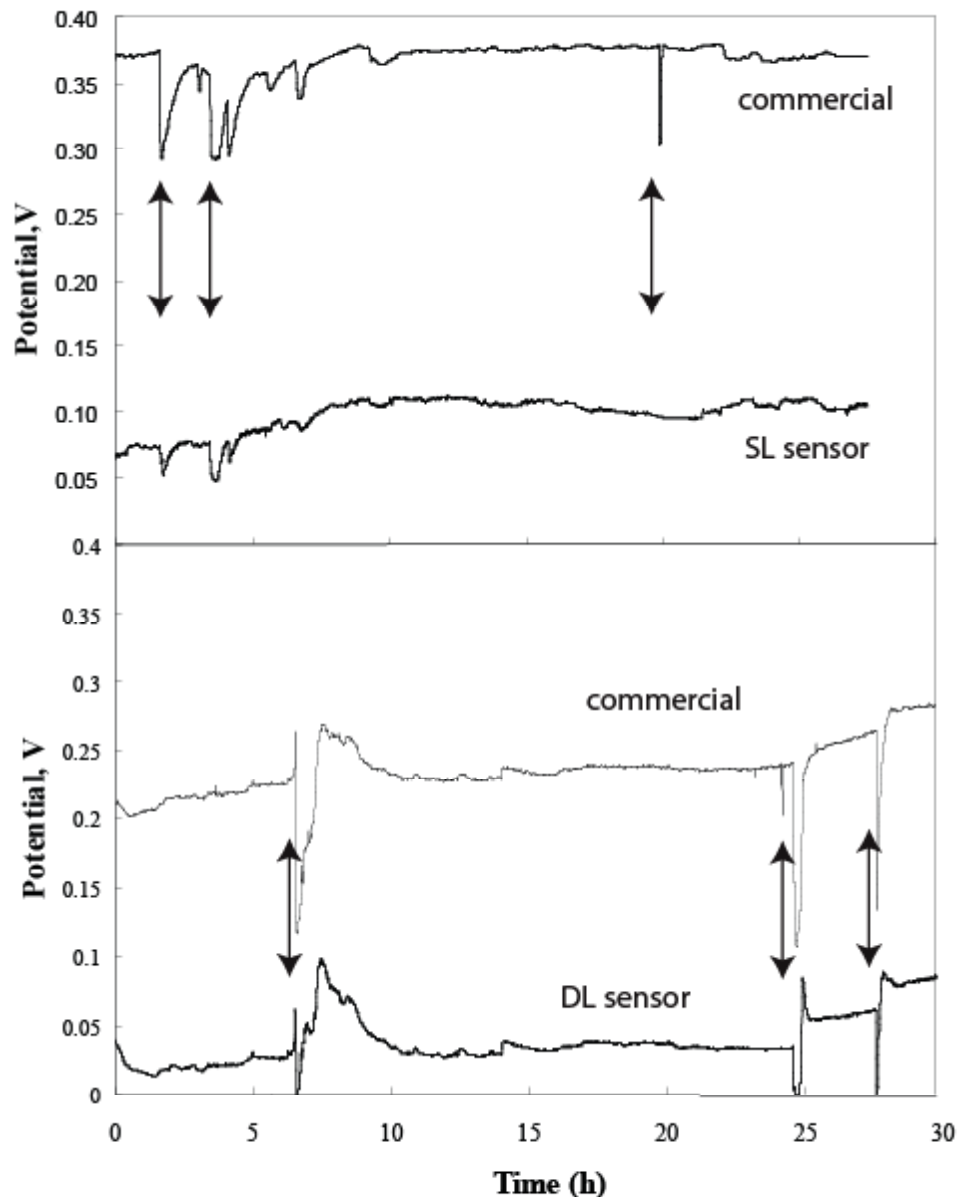


Figure 8. Continuous flow experiment with SL (PPyNO₃) (top) and DL (PPyNO₃-bPEDOT) (bottom) nitrate-selective microsensors and commercial sensors (sampling rate 30 sec; arrows denote times of pulse nitrate additions to the flowing stream).

1.5 PVC-Based Nitrate Mini-Sensors

This section describes the final effort aimed at improving the stability of the nitrate sensors, and represents a complete change of direction toward a polyvinyl chloride (PVC) based sensor. The PVC-based sensor fabrication technique is different from the

electro-polymerization technique we employed for the PPy-version of the microsensors, and is essentially the type of sensor being fabricated by industry in most cases. The advantages of the PVC-based sensors is that they are purportedly more stable than those described in the previous section for conducting organic polymers. One drawback, however, is that the fabrication process for the PVC sensors fabrication technique (evaporation) does not lend itself to the efficient miniaturization which was possible via the electro-polymerization process. Fortunately the solve evaporation strategy is used in commercial chip manufacturing and it is anticipated that these techniques could be applied to PVC-based sensors if they prove useful and stable enough for long-term deployments.

1.5.1 PVC-Based Nitrate Sensor Fabrication and Calibration

For sensors with PVC membranes, a mixture of polyvinylchloride (membrane matrix), plasticizer, and electroactive (ionophoric) substance (in this case, the quaternary ammonium ion) is dissolved in tetrahydrofuran (THF). The solvent is then evaporated off the mixture, leaving a membrane behind that is selective for nitrate. In this case, the quaternary ammonium in the PVC membrane serves as an ion exchange site, which is selective for nitrate.

The advantages of the PVC-based sensors is that they are purportedly more stable than those described in the previous section for conducting organic polymers. One drawback, however, is that the fabrication process for the PVC sensors fabrication technique (evaporation) does not lend itself to the efficient miniaturization which was possible via the electro-polymerization process. Fortunately the solve evaporation strategy is used in commercial chip manufacturing and it is anticipated that these techniques could be applied to PVC-based sensors if they prove useful and stable enough for long-term deployments.

Each PVC sensor must be coupled with commercial mini-reference electrode (ESA Inc., no leak model). The commercial (Sentek) sensors are 11 cm long and 12 mm in diameter, while each of PVC membranes is 5 cm long, 5.8 mm in diameter (Figure 9).

Figure 9. Fabricated PVC-based mini-ISE nitrate sensors (required reference electrode is not shown).



Outdoor/industrial data loggers (wired (HOBO Outdoor industrial U12-008, Onset Computer Corp.) and wireless (HOBO weather station) were used to obtain real-time data from each potentiometric cell. The mini-sensor output requires some electronic conditioning to make it compatible with the commercial dataloggers. We designed a circuit consisting of voltage follower, stabilizer (minimizes battery aging), voltage adder and 2 rechargeable batteries (2600 mAh). We successfully tested a prototypical circuit (Figure 10) and are now consulting with a commercial PCB fabrication vendor in order to design and produce small, inexpensive (on-a-chip) versions of this circuit.

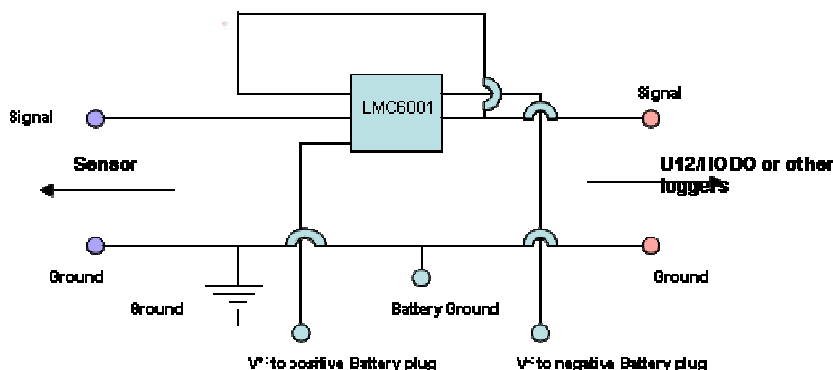


Figure 10. Basic configuration of the LMC6001 amplifier acting as a voltage follower for the PVC-based nitrate ISE sensors.

In terms of calibration, the PVC-based sensors performed as well or better than best commercial PVC sensors we located (Sentek DirectIon Sensors, UK), yielding similar calibration ranges and detection limits in all cases. However, PVC-based sensors typically exhibit some temperature-dependency with respect to calibration, and our sensors were no exception. The next section presents the results from the flow-through experiments, while the subsequent section addresses the temperature-dependency of the sensors.

1.5.2 PVC-Based Nitrate Sensor Testing in Flow-Through Systems

Given that commercial sensors are available for PVC-based nitrate sensors albeit relatively large and expensive ones, we were able to compare our sensors' performance to that of the commercial sensors in the flow-through experiments. Nitrate mini-sensors with PVC membranes showed very similar response under tap water flow conditions compared to commercially available sensors (Figure 11): both types of sensors clearly respond to nitrate standard (10^{-2} M NaNO_3) periodically introduced into the system, "home-made" mini-sensors maintained their sensitivity for 3 days of continuous exposure to tap water flow conditions. Sensors responded to incorporated nitrate standard in a similar manner: the voltage drop for CENS made sensors is 35-40 mV from the baseline, for commercial sensors it is 25-35 mV. Overall potential drift (within the baseline) did not exceed 5-7 mV for both types of sensors throughout the entire length of the experiment.

When we moved on to a soil test-bed, CENS-made sensors exhibited better response to nitrate standard pulses than did the commercially available sensor (Figures 12, 13): potential reading for both CENS-made mini-nitrate sensors return to a baseline ("recover") after sensors react to incorporated nitrate standard, commercial sensor, however, does not seem to "recover" completely (sensor reading do not come back to the baseline values).

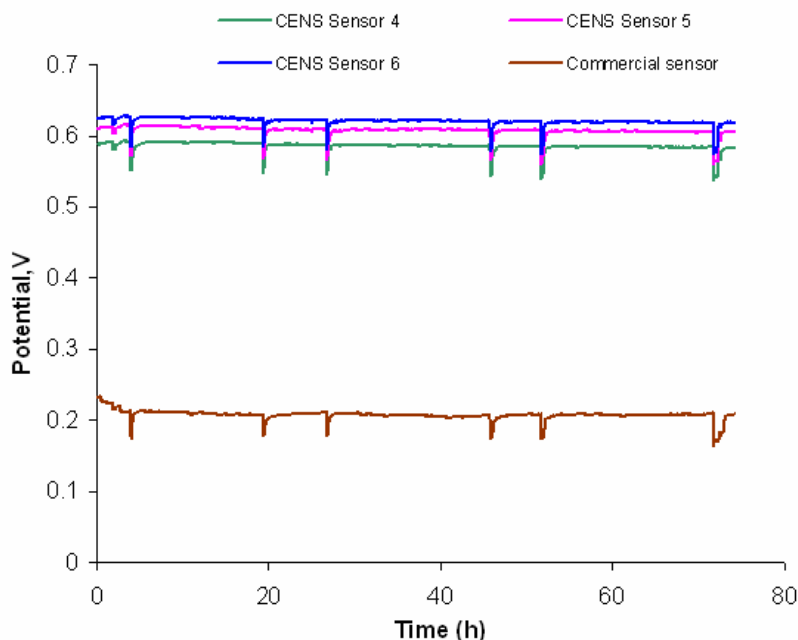


Figure 11. Testing nitrate mini-sensor prototypes under tap water flow conditions (1.5 l/min flow rate, each drop in voltage readings indicates nitrate standard addition to the flowing stream)



Figure 12. CENS made nitrate mini-sensors and commercial sensor in soil test-bed: typical laboratory setup

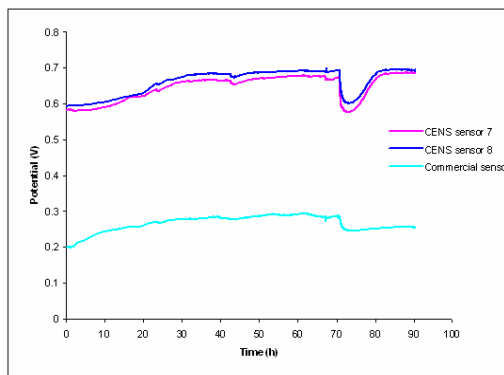


Figure 13. Results of soil test-bed experiment comparing CENS fabricated nitrate mini-sensors with PVC membranes and commercial sensor (nitrate standard was introduced to the system at roughly 72 h)

1.5.3 PVC Nitrate Mini-Sensor Temperature-Dependency

It is well-known that ISE responses are temperature dependent, and PVC-based sensors are no exception. According to Nernst equation, corresponding shifts in slope of sensor’s calibration curve for single charged ions are 2 mV per 10 °C. However, depending on the sensor materials, the actual affect of temperature changes may be greater. We undertook a laboratory investigation of the temperature dependency of

nitrate sensors by calibrating them with standards maintained over a range of temperatures. Results for multiple nitrate sensors are plotted in Figure 14.

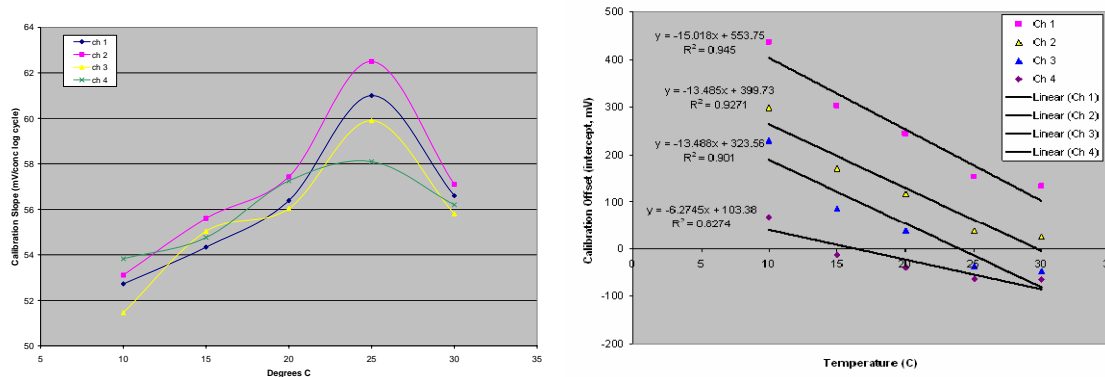
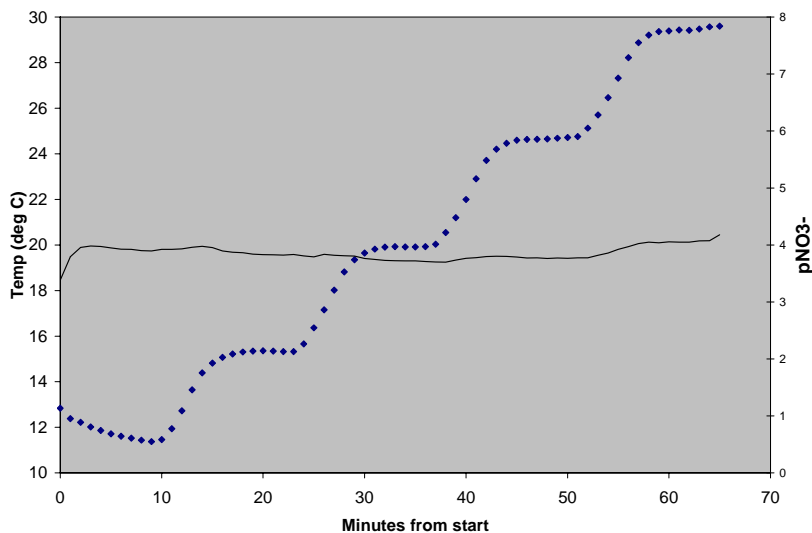


Figure 14. Calibration curve response factor (slope, plotted at left) and offset (intercept, plotted at right) for quadruplicate nitrate sensors as a function of temperatures.

The results suggest a nonlinear response of slope to temperature by the sensors, with new sensors exhibiting a more prominent temperature effect. For the intercept values, the temperature effect is more linear, with the slope inversely related to temperature. Again, the effect is more pronounced for newer sensors.

The curves in Figure 14 can be parameterized using linear or polynomial fits, and used to correct field sensor data for temperature. The results in Figure 15 validate the temperature correction algorithm.



In this experiment, the nitrate sensor was immersed in a single standard concentration while temperature was varied over a broad range (10 to 30 deg C).

Figure 15. Results from experiment to validate temperature-correction algorithm for the nitrate sensors (10^{-4} M nitrate solutions was exposed to step changes in temperature: solid line is nitrate sensor response; symbols denote temperature).

1.6 Summary and Conclusions

Ion selective electrodes (ISEs) were fabricated by electro-polymerization of conducting polymer doped with target ion (nitrate) on a carbon electrode, a well-known

method (Hutchins and Bachas, 1995). First, different types of miniaturized ion selective electrodes (ISEs) were created and tested based on conducting polymers doped with nitrate ions were created. Second, in an attempt to address stability/longevity issues with this version of the nitrate sensor, an insulating layer of bis-3,4-ethylenedioxythiophene (bis-EDOT) was deposited on the PPy surface in an effort to retain the dopant nitrate anions, which may be lost in flowing water. Third, after investigating the literature sources for possibility of using polyvinylchloride-based sensors with different membrane compositions for direct measurement of nitrate levels in soil we decided to change methods and use PVC membrane fabrication technology in order to obtain mini-nitrate-selective electrodes suitable for long-term flow-through experiments. All sensor versions were tested in batch and flow-through experiments with respect to their capacity to reproducibly quantify nitrate concentrations in static and moving systems over time.

The main conclusions with respect to the potentiometric nitrate mini-sensor development are as follows:

- Polypyrrole-based (PPy) nitrate sensors are relatively easy to fabricate and work well in batch settings, particularly if they can be stored in dilute nitrate solutions (10^{-4} M) between usages. These sensors can last up to about 6 months under these conditions.
- PPy nitrate sensors consistently fail under dynamic (flow-through) sampling conditions. The typical results will suggest reasonably accurate detection of nitrate levels in flowing water, followed by signal deterioration (sensitivity loss) on a time scale of hours. Hence, PPy nitrate sensors are unsuitable for use in most flow-through experiments.
- The cause for the loss of sensitivity in the PPy is unknown, but is suspected to be a result of significant loss of the dopant ion (nitrate) from the PPy membrane.
- Application of an insulating sheath of bis-3,4-ethylenedioxythiophene (bPEDOT) increased the longevity of the PPy based nitrate sensors by a factor of approximately 1.5 in flow through systems. However, these sensors require a significantly greater fabrication effort, which may not be worthwhile given the relatively modest absolute increase in sensor longevity they provide.
- Polyvinyl chloride (PVC) nitrate sensors based on a quaternary ammonium ionophore were successfully fabricated and show promise for use in observing nitrate in flow-through systems. These sensors are easy and inexpensive to fabricate, but require a voltage follower to condition the signal to a state that is readable by most commercial data-logging devices. An inexpensive voltage follower was designed and fabricated and has been successfully tested.

References Cited

Hutchins, RS and LG Bachas (1995). Nitrate-Selective Electrode Developed by Electrochemically Mediated Imprinting/Doping of Polypyrrole, *Anal. Chem.*, 67, 1654-1660.

- Bendikov, TA and TC Harmon (2005). A Sensitive and Highly Selective Nitrate Ion Selective Electrode from a Pencil Lead: An Analytical Laboratory Experiment, *Journal of Chemical Education*, 82(3), 439-442.
- Bendikov, TA, Kim, J and TC Harmon (2005). Development and Environmental Application of a Nitrate Selective Microsensor Based on Doped Polypyrrole Films, *Sensors and Actuators B: Chemical*, 106(2), 512-517.
- Bendikov, TA and TC Harmon (2005). Long-lived solid state perchlorate ion selective sensor based on doped poly(3,4-ethylenedioxythiophene) (PEDOT) films, *Analytica Chimica Acta*, 551, 30-36.
- Sotzing GA, Reynolds JR, Steel PJ (1997). Poly(3,4-ethylenedioxythiophene) (PEDOT) prepared via electrochemical polymerization of EDOT, 2,2'-bis(3,4-ethylenedioxythiophene) (BiEDOT), and their TMS derivatives, *Advanced Materials* 9:795-798.
- Vazquez M, Bobacka J, Ivaska A, Lewenstam A (2002). Influence of oxygen and carbon dioxide on the electrochemical stability of poly(3,4-ethylenedioxythiophene) used as ion-to-electron transducer in all-solid-state ion-selective electrodes, *Sensors and Actuators B* 82: 7-13.

Topic 2: Grain-scale origin of hydrodynamic dispersion

SUMMARY

We study dispersion in porous media by tracking movement of a swarm of solute particles through a physically representative network model. We developed deterministic rules to trace paths of solute particles through the network. These rules yield flow streamlines through the network comparable to those obtained from a full solution of Stokes' equation. In the absence of diffusion the paths of all solute particles are completely determined and reversible. We track the movement of solute particles on these paths to investigate dispersion caused by purely convective spreading at the pore scale. Then we superimpose diffusion and study its influence on dispersion. In this way we obtain for the first time an unequivocal assessment of the roles of convective spreading and diffusion in hydrodynamic dispersion through porous media. Alternative particle tracking algorithms that use a probabilistic choice of an out-flowing throat at a pore fail to quantify convective spreading accurately.

For Fickian behavior of dispersion it is essential that all solute particles encounter a wide range of independent (and identically distributed) velocities. If plug flow occurs in the pore throats a solute particle can encounter a wide range of independent velocities because of velocity differences in pore throats and randomness of pore structure. Plug flow leads to a purely convective spreading that is asymptotically Fickian. Diffusion superimposed on plug flow acts independently of convective spreading causing dispersion to be simply the sum of convective spreading and diffusion. In plug flow hydrodynamic dispersion varies linearly with the pore-scale Peclet number.

For a more realistic parabolic velocity profile in pore throats particles near the solid surface of the medium do not have independent velocities. Now purely convective spreading is non-Fickian. When diffusion is non-zero, solute particles can move away from the low velocity region near the solid surface into the main flow stream and subsequently dispersion again becomes asymptotically Fickian. Now dispersion is the result of an interaction between convection and diffusion and it results in a weak non-linear dependence of dispersion on Peclet number. The dispersion coefficients predicted by particle tracking through the network are in excellent agreement with the literature experimental data.

We conclude that the essential phenomena giving rise to hydrodynamic dispersion observed in porous media are (i) stream splitting of the solute front at every pore, thus causing independence of particle velocities purely by convection, (ii) a velocity gradient within throats and (iii) diffusion. Taylor's dispersion in a capillary tube accounts for only the second and third of these phenomena, yielding a quadratic dependence of dispersion on Peclet number. Plug flow in the bonds of a physically representative network accounts for the only the first and third phenomena, resulting in a linear dependence of dispersion upon Peclet number.

Introduction

Traditionally, mixing in single-phase flow through a porous medium is quantified by a *dispersion coefficient* obtained from the flow-averaged ("cup-mixed") effluent concentration history (Lake 1989). The dispersion coefficient describes apparent mixing because it is averaged over the entire outlet and has contributions (in inseparable form) from (i) *convective spreading* (also called *mechanical dispersion*), caused by variations in

path lengths and velocities of solute particles traveling along different streamlines and (ii) *molecular diffusion*.

Despite decades of research there remain questions about the nature and origin of dispersion. It is well accepted in the literature that convective spreading is orders of magnitude larger than diffusion. Is dispersion predominantly an artifact of convective spreading and diffusion categorically negligible (Coats *et al.* 2004), or does the role of diffusion become important in one limit or another?

The main objective of this paper is to explain core-scale dispersion from pore scale physics. We investigate dispersion by tracking the motion of a swarm of particles through granular porous medium. The flow paths through the medium are computed using a physically representative network model. We developed deterministic rules to trace solute particle's path from the inlet of the medium to its outlet. Because the rules are deterministic, the paths of solute particles are completely known in absence of diffusion. It also ensures that the flow paths are reversible, that is, upon reversal of the flow direction each particle will exactly retrace its path back to the inlet. Upon flow reversal convective spreading gets cancelled and echo dispersion is zero (Jha *et al.* 2006, John *et al.* 2008)). Our algorithm captures the essential features of convective spreading and allows us to investigate it explicitly and rigorously in a realistic pore space. To the best of our knowledge it has not been previously attempted. We show that the paths of arbitrarily close pairs of particles become independent relatively quickly even in the absence of diffusion and even after accounting for spatial correlation of pore structure.

Next, diffusion is superimposed and movement of solute particles because of combined effects of convection and diffusion is monitored. Dispersion is quantified from spatial and temporal statistics of solute particles. With this framework we can quantitatively investigate the influence of increasing diffusion on dispersion. We explain the origin of core scale dispersion in terms of the interaction between convection and diffusion. The method predicts *a priori* the correct power law dependence of dispersion coefficient on pore scale Peclet number. All our predictions are consistent with the experimental results reported in the literature. Models more sophisticated than ours, e.g. a direct solution of the Stokes (or Navier-Stokes) equation in the pore space of a granular material coupled with a solution of the convection-diffusion equation, would also predict core-scale dispersion correctly. We propose that ours is the simplest model that captures the essential physics.

Model Development

Physically Representative Network Model. Pore-network modeling is an important tool that provides a link between continuum (core) scale properties of a porous medium and the pore scale physics. In a network model the pore space is discretized into a set of pores (nodes) connected by pore throats (bonds). Since it is very difficult to explicitly capture the details of pore geometry, most of the network models reported in the literature make some simplifying assumptions. Common assumptions include same length for all the throats and regular network lattice. Throat radii are often picked randomly from an assumed distribution. For example, Acharya *et al.* (2007) and Bruderer *et al.* (2001) assumed uniform and a log-uniform distribution of throat radii respectively. Bijeljic *et al.* (2004) used a more realistic throat distribution obtained from Berea sandstone and satisfactorily predicted dispersion coefficient for a wide range of pore scale Peclet numbers.

All of the above mentioned assumptions are found to be invalid in realistic pore space, even in relatively simple porous media (Bryant *et al.* 1993). Picking bond radii randomly from a distribution disregards spatial correlation in the bond conductances. There is a strong correlation in bond conductances in a realistic porous medium, even though it exists for a short distance (Bryant *et al.* 1993). This correlation has significant impact on permeability and dispersion through the medium which cannot be neglected (Bryant *et al.* 1993, Jha 2008). Therefore, we adopt the approach of physically representative network models, which replicate the pore space more closely. In this work we use a computer generated dense random packing of 10000 spheres as a model porous medium (Thane 2006). Such packings capture essential geometric and topologic features of sediments. The radius and the center coordinates of each sphere are known which completely determines the micro-structure of the medium (Fig. 1). The radius of each sphere is 2.1918×10^{-4} m. The medium is about 34 sphere diameters long in the z -direction and 17 sphere diameters long in x and y directions. The porosity of the medium is 36%.

From this data we prepare a physically representative network model that has pore bodies located at the same spatial positions as the pores in the actual medium. Moreover, the bonds connecting neighboring pores have the same conductances as in the actual medium. Thus a physically representative network model preserves the geometry, topology and spatial correlation in flow properties. It is three dimensional and unstructured.

Evaluating Bond Conductances and Obtaining Flow Rates. Delaunay tessellation is an unambiguous way of dividing the sphere packing into cells called Delaunay cells. Delaunay tessellation groups together sets of four nearest spheres and thus a Delaunay cell in three dimensions is a tetrahedron (Fig. 2a). The vertices of a Delaunay cell lie at the centers of the four spheres forming that cell.

The interior of the cell encloses a region of void space identified as the pore body. The geometric center of the Delaunay cell can be considered as the pore center. Each face of a Delaunay cell is a plane of maximum constriction and represents a narrow entrance to the pore body (Fig. 2b). Since each cell is a tetrahedron, every pore has four faces or throats connecting it to four neighboring pores.

Two pores are connected by a path of converging-diverging cross-section (Fig. 3a). The flow conductance of the path is governed by the narrowest constriction in the path. Figure 3b shows a cell face shared by two neighboring cells (pores). The cell face represents the narrowest constriction in the flow path connecting the two pores. The figure also shows two circles that approximate the narrowest constriction. r_c is the radius of the largest circle that can be fit in the narrowest constriction and r_e is the radius of the circle having the same area as the narrowest constriction. If the constriction radius is approximated by r_c , the path (or bond) conductance is underestimated since some area available for flow in the constriction is not taken into consideration. On the other hand, if the constriction radius is approximated by r_e , the path (or bond) conductance is overestimated because for a given area a circle provides the least resistive path for viscous flow. The arithmetic average of the two radii a good estimate of the effective radius of the bond connecting the two neighboring pores $r_{eff} = (r_e + r_c)/2$ (Bryant *et al.* 1993). For the purposes of computing flow, we replace the converging-diverging

geometry of each throat with a cylindrical bond of radius r_{eff} . This idealization proves to preserve the essential features of the local flow field while enormously simplifying the flow dynamics.

The conductance of the bond connecting the two neighboring pores is given by $g = \pi r_{eff}^4 / 8\mu l$, where μ is the fluid viscosity and l is the distance between the pore centers.

A schematic of the network is shown in Fig. 4a as a network of electrical resistances. The location of every pore body (bond junction) and conductance of bonds connecting it to its neighbors have been calculated. We apply a potential gradient across the network. The side boundaries of the network are sealed. Then we write the mass balance equation at each pore. Imposing steady state (no mass accumulation at any pore) results in a set of linear equations and we can solve for potential at each pore (Fig. 4b). After knowing the potentials, the flow rate through any bond can be easily calculated as follows:

$$q = g \Delta P$$

Rules for Particle Tracking

Particle Movement in the Network in Absence of Diffusion. Bonds in a physically representative network model connect centers of pairs of adjacent pores. Since the bonds have nonzero radii, the four bonds originating at the center of a pore necessarily overlap (Fig. 5). Overlapping bonds may seem unphysical. However, bonds are not to be considered in completely literal sense. It is a way to model flow from one pore to another. We track particle movement through the network of overlapping bonds. We neglect momentum loss and mixing in the overlapping region and discount bond lengths in the overlapping region in calculation of the local Peclet numbers. This simple model yields an accurate *a priori* prediction of the permeability of the sphere packing (Bryant *et al.* 1993).

In absence of diffusion, a solute particle moves in a bond parallel to its axis. After reaching the outlet face of the bond at a pore center, the particle will enter one of the out-flowing bonds originating at that pore center. One of the most common simplifying assumptions made in particle tracking through a network model is the probabilistic choice of an out-flowing bond. A solute particle arriving at a pore body (junction of bonds) is assigned to an out-flowing bond randomly with a flow rate weighted probability. However, probabilistic choice of out-flowing bond is not realistic as it makes dispersion an irreversible process even in absence of diffusion. Moreover, it ignores spatial correlation in bond conductances which is one of the key features of the physically representative network models (Jha 2008). Therefore, convective spreading cannot be modeled correctly with this approach.

To avoid these problems we developed deterministic rules to decide an out-flowing bond and to map the entrance point of the solute particle on this bond. The rules are based on the patterns followed by streamlines and described briefly below. The physical and geometric details are less important than the principal logical feature of the rules: at every pore center the rules establish a one-to-one mapping from points on the outlet face(s) of in-flowing bond(s) to points on the inlet faces of out-flowing bond(s). Thus when the direction of flow is reversed, a particle retraces its flow path exactly in the absence of diffusion. A direct calculation of the flow field would eliminate the need for

the rules. However, it is not convenient and practical to resolve flow field accurately for the entire domain which contains about 35,000 pores.

After reaching the outlet face of the bond at a pore body, the particle immediately jumps to the inlet face of the next out-flowing bond (decided from the deterministic rules). This causes a small discontinuity in the path of the particle because of overlapping of bonds in the region near the pore body. Discontinuities are small as compared to the path length. Moreover, effect of discontinuities on particle statistics accumulated over several pores tends to get cancelled. Thus the particle statistics is not affected by these discontinuities (Jha 2008).

Particle continues its motion through successive bonds to the outlet of the network.

Deterministic Rules for Mapping a Entrance Point of a Particle on an Out-Flowing Bond

A particle enters the pore through an in-flowing bond and it leaves through an out-flowing bond. The task is to develop rules for calculating which out-flowing bond will be the exit and to map the entrance point of the solute particle on the out-flowing bond. Here we describe a simple and computationally tractable approach for this purpose.

We identify six flow configurations feasible at a pore body. In each case, we figure out splitting of streams based on the flow configuration and flow rates. This tells us a solute particle exiting an in-flowing bond at a particular point will enter which segment of which out-flowing bond. In each case we calculate some reference points that serve as guiding points to map the exact entrance position of solute particle on the out-flowing bond.

For ease of illustration and for calculating reference points, we displace all the bonds along their axes by equal distance. The displacement should be enough to remove overlap between the bonds. After identifying flow configuration and calculating reference points, all the bonds are moved back to their original location.

The bonds are numbered according to their flow rates. Inflow is assigned positive sign and outflow negative. Then flow rates are sorted in descending order along with their sign. Thus the first bond is the one carrying maximum inflow and the fourth one is carrying maximum outflow. The first bond is taken as the reference bond. The distances of the face centers of all the bonds from the face center of the first bond are calculated. The closest bond will have the biggest influence on flow.

Configuration 1: One In-Flowing and Three Out-Flowing Bonds. In this case one in-flowing bond feeds all the out-flowing bonds. Therefore, the incoming stream splits into three segments based on the flow rates of the three out-flowing bonds (Fig. 14a).

For example, in Fig. 14a the fourth bond is closest to the in-flowing bond and the third bond is the farthest. First, we find (numerically) the pair of points on the first and fourth bond faces that are closest to each other. These are reference points (reference point 1 on bond 1 and reference point 6 on bond 4). A solute particle exiting bond 1 at reference point 1 on bond 1 will enter bond 4 at reference point 6. These reference points also guide mapping of other points.

Starting with reference point 1, we mark a segment of in-flowing bond that carries same flow rate as the out-flowing bond 4. A solute particle exiting bond 1 from this segment will enter bond 4.

Similarly, we mark a middle segment of the in-flowing bond that carries the same flow rate as the farthest out-flowing bond. A solute particle exiting the in-flowing bond on the middle segment will enter the farthest bond. Solute particle exiting bond 1 on the remaining third segment of the in-flowing bond will enter the second bond.

Reference point 2 on the in-flowing face is taken as point where the line joining reference point 1 to the center of the face intersects the boundary of the first segment. Reference point 3 is diametrically opposite of the reference point 1. Reference point 4 is the point on tube 2 that is closest to reference point 3. Similarly, reference point 5 is the point on tube 3 that is closest to reference point 2.

Configuration 2: Three Bonds Flowing In, One Flowing Out. This configuration is exactly opposite of the configuration 1 (Fig. 14b). Three in-flowing bonds feed to one out-flowing bond. Therefore, the out-flowing stream consists of three segments, each segment receiving flow from one of the in-flowing bonds. The procedure described for connecting segments and calculating reference points in configuration 1 is applicable in this case also.

There are more than one possible flow configurations when we have two in-flowing and two out-flowing bonds at a pore junction.

Configuration 3: Third Bond is the Farthest and Flow in First Bond is Smaller than that in the Fourth Bond. Since flow rate in the first bond is smaller than that in the fourth bond, the fourth bond has to receive flow from both the in-flowing bonds. Since some streamlines move from bond 2 to bond 4 and streamlines cannot cross, no streamline can move from bond 1 to bond 3. Therefore, bond 3 will get all its flow from bond 2 and all of flow from bond 1 will go to bond 4.

Marking of segments and calculations of reference points is similar to that described for configuration 1.

Configuration 4: Third Bond is the Farthest and Flow in First Bond is Greater than that in the Fourth Bond. It is similar to the configuration 3, except that in this case the flow in the first bond is larger than that in the fourth bond. In this case the fourth bond receives all its flow from bond 1 and all of the second bond's flow enters the third bond. The first bond feeds to both the out-flowing bonds.

Configuration 5: Fourth Bond is the Farthest. Since flow rate in the fourth bond is greater than that in the second bond, the fourth bond receives flow from both the inflowing bonds. Since streamlines cannot cross, flow from the second bond cannot enter the third bond. Hence, all the flow from the second bond enters the fourth bond. Also the third bond receives all its flow from the first bond. As evident from Fig. 14e, bond 1 feeds to both the out-flowing bonds and bond 4 receives flow from both the in flowing bonds.

Configuration 6: The Second Bond is the Farthest. In this configuration the farthest bond is in-flowing. Or in other words, the second bond is the farthest. In this

case, both the inflowing bonds will feed to both the out-flowing ones as shown in Fig. 14f. Flow segments and reference points are calculated as described previously.

The reader is referred to Jha (2008) for calculation details.

Mapping an Incoming Point to an Out-flowing Bond

After deciding the incoming and outgoing segments of the bonds, we have to map the incoming point to a corresponding point on the outgoing section. Incoming and outgoing sections are arbitrary sections of a circle. We impose geometric rules that are physically reasonable: (i) reference point on the in-flowing segment will connect to the corresponding reference point on the out-flowing segment and (ii) center of the incoming segment connects to the center of the outgoing segment. We take center of the circular segment as its geometric center (or center of gravity). We call the vector joining the reference point to the center of the segment the “reference vector”. We mark reference vectors on incoming as well as outgoing segments (Fig. 15).

In polar coordinate system, two parameters are sufficient to describe the outgoing point (i) the angle the position vector of the outgoing point (here defined with reference to the center of the segment) makes with the reference vector and (ii) its relative radial distance from the center (defined as distance of the point from the center normalized by distance to boundary in that direction). We impose another geometric rule: these parameters for the outgoing point have the same value as that for the incoming point. Therefore, we evaluate the angle θ , the position vector of incoming point makes with the reference vector on the incoming segment and relative radial distance of the point from the boundary, r/R . Here r is the distance of incoming point from the center and R is distance from the center to the boundary of the segment. We place the outgoing point at the same θ and r/R on the outgoing section (Fig. 15). This rule provides a deterministic, one-to-one mapping between exit and entrance points.

Particle Tracking in a Bond with Convection and Diffusion. The motion of a solute particle in a bond in presence of diffusion is divided into small time steps of equal duration dt . We split each step into a convection-only displacement followed by an instantaneous diffusive jump. The magnitude of convection-only displacement is equal to the product of fluid velocity at that location and the duration of time step. The direction of convection-only step is parallel to the bond axis. In the diffusive step, particle moves in a random direction on the surface of a sphere with radius $r_{diff} = \sqrt{6D_o dt}$ (Bruderer and Bernabe 2001), where D_o is the diffusion coefficient. The particle’s diffusive displacement in Cartesian coordinate system is given by (Bijeljic *et al.* 2004): $\Delta x = r_{diff} \cos\theta \sin\varphi$, $\Delta y = r_{diff} \sin\theta \sin\varphi$ and $\Delta z = r_{diff} \cos\varphi$; where θ is uniformly distributed between 0 and 2π and $\cos\varphi$ is uniformly distributed between -1 and 1. For every time step we pick a value for θ and φ . θ is a random number between 0 and 2π . For generating φ , we pick a random number between -1 and 1 and take inverse cosine of that (Bijeljic 2007).

If during any time step the particle hits the bond wall, it is reflected back into the bond.

The algorithm for tracking particles movement through a capillary tube is validated by comparing simulations in a cylindrical tube with results with Taylor’s theory and experiments (Jha 2008). A close agreement of simulated results with Taylor’s theory validates the algorithm.

Algorithm for Particle Tracking through the Network. (1) Starting positions of a swarm of 15000 particles at the inlet face of the network are decided in advance. Particles are distributed to the inlet bonds in proportion to their flow rates. In an inlet bond, particles are distributed uniformly over its inlet face.

(2) We track one particle at a time. A particle moves with convective and diffusive steps through a bond till it reaches a pore body (bond junction). Its position is mapped to an out-flowing bond based on the deterministic rules discussed above and described in the Appendix.

We used same rules for particle tracking for all the Peclet numbers. The position of a particle at the entrance of an outlet bond depends only the flow configuration and relative flow rates at a pore center. This rule is strictly valid when solute transport is dominated by convection. A better rule to decide the out-flowing bond in diffusion dominated regime ($N_{Pe} < 4$) should be based on cross sectional areas of bonds rather than their flow rates. However, the focus of the rules is to capture the convective transport from one bond to the next and thereby account for the contribution of convective spreading.

(3) The particle continues its movement through successive bonds till it reaches the outlet of the network. Particle positions are scanned at regular time intervals. We also record the residence time of the solute particle. Dispersion coefficient is calculated from spatial as well as temporal statistics.

Results

We use the model described above to focus on the three physical features of pore-level flow and solute transport. The first is **stream splitting** of solute front at every pore which causes a sequence of independent and random velocities of solute particles in successive bonds. The second is **variation of velocity within a bond**, the consequence of momentum transfer with no-slip boundary conditions. The third is **diffusion**, the consequence of random movement of solute particles. We examine these phenomena individually and in combinations. Only when all three are accounted for do we obtain predictions consistent with the experimental observations.

Convective Spreading as a Diffusive Process. We first apply the algorithm to investigate purely convective spreading. The network flow calculation yields volumetric flow rates through each bond. We impose a plug-flow velocity profile in each bond, i.e, all particles in a bond move at the same velocity. The direction of movement is parallel to the bond axis, and the speed is $\bar{v} = q / \pi r_{eff}^2$. Diffusion is neglected. Thus only one of the physical features of interest affects this set of simulations.

Figure 6a shows paths of five different pairs of particles. The particles in each pair were initially close to each other. The rules determining the exit bond taken by a particle entering a pore constitute a mapping. The mapping is unique for each pore in the network. At the higher level, the mapping relates geometric regions: well-defined segments of the exit faces of in-flowing bonds are connected to well-defined segments on inlet faces of out-flowing bonds. At the lower level the mapping connects a single point within a geometric region on an exit face to a point within a corresponding region on an inlet face. Thus if a pair of particles reach an exit face and are in the same geometric region, they will enter the same out-flowing bond together (details in the appendix). As

the pair of particles proceeds through the network, eventually they will arrive at an exit face on opposite sides of a line separating two geometric regions on that face.

When the particles fall on opposite sides of the split stream on an exit face, they take different paths and their movements become independent of each other. They are unlikely to come together again, and their positions become uncorrelated. This is true even in the absence of diffusion. It is simply a consequence of the asymmetric splitting and rejoining of flow paths around randomly arranged obstacles, that is, the grains comprising the porous medium. This is a manifestation of convective spreading. It is useful to contrast the situation in ordered arrangements of grains. There the splitting/rejoining is symmetric, and positions of a pair of particles remain correlated regardless of their initial separation (Jha 2008). If plug flow occurs in bonds and there is no diffusion, then no independence of particle paths occurs because of convective spreading in an ordered packing.

Figure 6b shows paths of several solute particles (moving without diffusion with plug flow in bonds) starting at the same inlet pore. A particle's displacement becomes independent of other particles very quickly because of frequent splitting of flow passages. The randomness of convective spreading in porous medium is inherent in the morphology of the pore space (Sahimi *et al.* 1986).

In the conventional Fickian representation of dispersion, convective spreading is considered to be “diffusion like”, that is, a statistically random process. The sufficient conditions that convective spreading because of splitting at pore junctions can be treated like diffusion in a continuum transport equation can be stated in terms of the central limit theorem (Chandrashekar 1943, Sahimi *et al.* 1986). The central limit theorem states that the sum of a large number of independent and identically distributed random variables will be approximately normally distributed (Bear 1972). After a particle has traveled a distance greater than the correlation length in velocity, its total displacement can be considered as the sum of independent and random convective steps. Consequently after a few steps the spatial distribution of solute particles' displacements is expected to be normal (Gaussian) as per the central limit theorem and convective spreading can be considered like a diffusive process. Cenedese and Viotti (1996) and Moroni and Cushman (2001) show by three-dimensional particle tracking velocimetry experiments in bead packs that velocity components quickly become independent. Correlation lengths are of the same order as the grain dimensions. Longitudinal dispersion coefficient becomes Fickian after solute front has traversed five to six pore diameters (Manz *et al.* 1999). Though the experiments are not diffusion-free, the agreement with our simple model is encouraging.

Particle Tracking without Diffusion.

With Plug Flow in Network Bonds. Having seen the role of convective spreading with small groups of particles, we now track movement of a swarm of 15,000 particles through the same physically representative network model. Again we impose a plug-flow velocity profile in each bond of the network and neglect diffusion. The particles move from bottom to top of the domain (positive z direction). The average interstitial velocity is 5.12×10^{-5} m/s which roughly corresponds to about 0.12 grain diameters per second.

The particle positions are scanned at several time intervals. A probability distribution plot of particles' spatial positions is shown at several different times in Figs.

7a-c. For comparison, a normally distributed probability distribution plot having the same mean and standard deviation as the actual data is also plotted in each case.

The dispersion coefficient at each time is calculated from spatial statistics using $D_L = \sigma_z^2 / 2t$ where σ_z^2 is the variance of solute particle positions in the z (longitudinal) direction at time t . For verification we also compute the dispersion coefficient using the particles' residence time statistics and using a solution to the one dimensional convection diffusion equation (Lake 1989). The dispersion coefficient calculated from spatial statistics increases with time (and travel distance) and approaches an asymptotic value (Fig. 7d). The asymptotic dispersion coefficient is very close to that obtained from temporal statistics in all the cases studied. For consistency, the dispersion coefficient obtained from temporal statistics is taken as the dispersion coefficient.

It can be seen from Figs. 7a-c that particles are normally distributed at all the times. The particle velocities become independent quickly because of splitting of solute stream at each pore and randomness of pore structure. Solute particles get normally distributed as expected from the central limit theorem. The convergence of the dispersion coefficient to an asymptotic value is governed by correlation in the local pore structure. After the asymptotic value of dispersion coefficient has been obtained, purely mechanical dispersion is Fickian. The asymptotic dispersion coefficient for purely mechanical dispersion is evaluated to be $9.25 \times 10^{-9} \text{ m}^2/\text{s}$.

With Parabolic Velocity Profile in Bonds. Using the same steady state solution for flow in the network as in the preceding section, we impose a parabolic velocity profile in each bond of the network. As in the preceding section, we neglect diffusion. Thus two of the physical features of interest (stream splitting and velocity variation) affect this set of simulations. The velocity profile is taken from the classical Hagen-Poiseuille analysis of flow in a cylindrical bond of radius r_{eff} .

$$v(r) = 2\bar{v} \left\{ 1 - \left(\frac{r}{r_{eff}} \right)^2 \right\}$$

where r measures the radial distance of the particle from the bond axis.

Figure 8 shows the particle statistics for a swarm of 15,000 particles moving through the network. For early time there are two peaks in the probability distribution function. The peak at smaller displacement corresponds to solute particles initially located in the slower zone near the wall of the bonds, i.e. at $r \approx r_{eff}$. At longer distances traveled, a second peak emerges in the distribution. It corresponds to particles initially located in the faster moving core of a bond, i.e. at $0 < r < ar_{eff}$ where $a \approx 0.9$. These particles are free to move at early times and have traveled a sufficiently large distance to experience a wide range of flow velocities (Lebon *et al.* 1997). At longer times, the second peak is closer to normal distribution. However, the first peak persists at the longest time observed.

It may be argued that the dispersion coefficient is converging to an asymptotic value (Fig. 8d). However, the concentration profiles make it clear that the transport process is not Fickian. This behavior is general. If a stochastic velocity field contains regions of zero velocity, there is no purely hydrodynamic mechanism by which solute particles in these regions can reach rest of pore space. Particles in these regions cannot

have any random velocity from the velocity distribution. Therefore, central limit theorem is not applicable and the dispersion coefficient is not well defined in this case. Effect of diffusion must be considered for the transport process to become Fickian even in the limit of high Peclet number (Koch and Brady 1985, Duplay and Sen 2004).

Steady-state single-phase flow in the network is a linear process. If the overall pressure drop across the network is changed, the pressure difference between the extremities of each bond of the network changes in proportion. It follows that the velocities, flow rates and transit times in each bond also change in proportion. Hence the ratio between flow rates in different bonds that connect to the same node remain unchanged and therefore the mapping rule at the pore junction remains unchanged if average velocity changes. Consequently the dispersion coefficients are proportional to the mean velocity. Therefore, in absence of diffusion (or negligible diffusion), the mechanical dispersion depends linearly on velocity (Sahimi *et al.* 1986).

Particle Tracking with Diffusion.

With Plug Flow in Network Bonds. Next we study influence of diffusion on particle statistics and dispersion coefficient. A plug-flow velocity profile is imposed in the bonds of the network. Thus two of the three physical features of interest (stream splitting and diffusion) affect the solute transport.

Particles move with convective and diffusive steps as described previously. The time step should be small enough to prevent diffusive jumps from being larger than the bond diameter (Bruderer and Bernabe 2001). In the simulations reported here the time step was taken to be one tenth of this value (evaluated for the average bond diameter) to reduce numerical error.

Figure 9 shows effect of diffusion on solute particle statistics. It is evident that diffusion has negligible impact on particle distribution for diffusion coefficients ranging from 0 to 10^{-9} m²/s because diffusion is very small in magnitude as compared to mechanical dispersion. The dispersion coefficient remains constant in this range of diffusion coefficients. For higher diffusion coefficients, diffusion becomes significant in magnitude as compared to mechanical dispersion and therefore, variance of particle displacements increases and this increases the dispersion coefficient.

When diffusion is very small, transport is dominated by convection. However, at very low Peclet numbers when diffusion is large, our flow-rate-weighted rule for deciding an out-flowing bond captures only part of the particle dynamics at a pore center. Therefore, in this case the particle statistics deviate from normal distribution at longer times.

Figure 10 shows the *a priori* prediction of dimensionless dispersion coefficient vs. pore scale Peclet number for this case. The agreement with the experimental data from the literature is good for small and moderate Peclet number, but it is clear that the scaling is incorrect for large Peclet numbers. The experimental data suggests a power law relationship between dispersion coefficient and Peclet number with the power law coefficient β in the range of 1.1 to 1.3. The simulations yield $\beta = 1$.

The cause of the incorrect scaling is the plug-flow velocity profile in the bonds. Under this assumption there is no stretching of a solute front as it moves along a bond. Therefore, flow velocity within a bond has no interaction with diffusion: a particle making a diffusive jump to another streamline within a bond still travels at the same velocity after the jump. Thus diffusion acts independently of mechanical dispersion

(convective spreading), and the dispersion coefficient is just the sum of pure mechanical dispersion and diffusion. Consequently for small diffusion (large Peclet number), we get a linear dependence of dimensionless dispersion coefficient on pore scale Peclet number. The longitudinal dispersion coefficient for the full range of Peclet number can be expressed as:

$$\frac{D_L}{D_o} = \frac{1}{F\phi} + 0.877 \frac{v D_p}{D_o}$$

The first term in the above equation represent the contribution of diffusion and the second term is the result of convection.

With Parabolic Velocity Profile in Bonds. Finally we examine the influence on dispersion of all three physical features (stream splitting, velocity variation and diffusion) simultaneously. We repeated the simulations of the previous section but with a parabolic velocity profile in each network bond as described above.

If a bond has a velocity gradient within it, then the interaction between convection and diffusion is no longer trivial. Now a solute front stretches as it travels along a bond, and diffusion becomes a much more effective mixing mechanism. (This interaction is the basis of the familiar Taylor's dispersion (Taylor, 1953).) Because velocity now influences dispersion within a bond, the dispersion coefficient will not simply be the summation of mechanical dispersion and diffusion.

Figure 11 shows a comparison of dimensionless dispersion coefficient obtained from simulations with the experimental data. The match is excellent for the whole range of Peclet numbers. From curve fitting we get a power law coefficient of 1.23. This *a priori* quantitative prediction of dispersion coefficient and its scaling behavior indicates that the essential physics of dispersion through pore space has been captured.

We investigate the interaction of convection and dispersion more closely. Figure 12 shows effect of diffusion on particle statistics for physically representative network with parabolic velocity profile in bonds. Even a vanishingly small amount of diffusion of 10^{-13} m²/s starts moving solute particles from low velocity regions near the wall to high velocity regions. After moving out of this zone, solute particles can sample all the regions of pore space because of stream splitting. The first peak at small displacement corresponding to particles in the slow moving region near walls starts decreasing and almost disappears by 150 seconds. We get a normal distribution of solute particle positions.

This is consistent with experimental observations by Lebon *et al.* (1997). They studied dispersion at short times using a PFG-NMR technique. At short times, the displacement of the molecules is small enough that the local displacement is proportional to the local velocity component along the magnetic field gradient. At mean displacements larger than 5 bead diameters, the displacement distribution was found to be Gaussian. At intermediate displacements, the measured distribution displayed two peaks. With increasing diffusion coefficient the peak at small displacements disappears quickly (Jha 2008).

Figure 13 shows effect of increasing diffusion on dispersion. For zero diffusion there is a wide range of particle positions because of velocity gradient in the bonds. As diffusion is increased solute particles move in the radial direction in the bonds and effect of velocity gradient in bonds is reduced. This reduces the spread in solute particle

positions and therefore dispersion coefficient is reduced. This trend continues with increasing diffusion and reverses when magnitude of diffusion coefficient becomes large as compared to the mechanical dispersion. The dispersion coefficient vs. diffusion coefficient plot goes through a minimum.

Discussion

The rules for determining the exit bond taken by a particle entering a pore enable us to isolate the contribution of convective spreading to core-scale dispersion. Convective spreading, also known as mechanical dispersion, occurs simply by virtue of a stochastic velocity field in a granular porous medium. Different bonds carry different flow rates, and there is no long-range correlation of these flow rates. Thus particle positions eventually become uncorrelated as flow continues, even in the absence of diffusion. Consequently dispersion only because of convective spreading grows like N_{Pe} . However, the purely mechanical analysis is not valid in the region of zero velocity. More importantly, in the absence of diffusion, either the scaling behavior of dispersion coefficient with Peclet number, N_{Pe} is incorrect (in the limit of plug flow in bonds), or the solute transport is non-Fickian (when bonds have parabolic velocity profiles). These problems are despite having a physically representative flow field at the pore scale. Thus diffusion is essential for explaining core-scale dispersion.

The region of zero velocity near the grains of the porous medium gives rise to non-mechanical dispersion mechanisms. Non-mechanical dispersion arises when a solute molecule cannot sample all points within the pore space by convection alone. Solute particles in the boundary layer near the solid surfaces are not free to move. Diffusion is required to enable these solute particles to escape the boundary layer. Subsequently a solute particle can encounter a wide range of velocities because of stream splitting. This sampling gives rise to the Fickian behavior of dispersion (Koch and Brady 1985, Duplay and Sen 2004). Therefore, diffusion even though small in magnitude, is essential for Fickian behavior of dispersion.

A plug flow velocity profile does not have regions of zero velocity. Therefore, non-mechanical dispersion does not occur, and dispersion scales linearly with N_{Pe} ($\beta = 1$). However, in case of parabolic velocity profile in network bonds there are regions of no-flow velocity near pore-walls. Therefore, we get a non-mechanical dispersion which becomes important at high Peclet numbers and results in a mild non-linear dependence of dispersion coefficient on Peclet number ($\beta = 1.2$).

Taylor (1953) showed that in a single capillary tube, the interaction of diffusion and the parabolic velocity profile yields a much stronger dependence, of dispersion coefficient on Peclet number ($\beta = 2$). Our model invokes tubes, albeit of short length, in which a parabolic velocity profile exists. Why then does transport in the physically representative network – and in experiments – exhibit a much smaller value of β than Taylor's analysis? The reason is the asymmetric splitting and rejoining of flow paths around grains in the porous medium. Individual bonds are much shorter than the length required for Taylor's asymptotic solution to apply, and the splitting/rejoining process in a disordered medium causes convective spreading to dominate the dispersive behavior at large values of Peclet number.

Summary and Conclusions

We construct a pore-level model of single-phase solute transport that has three key features: (i) splitting of solute swarms at every pore body (ii) velocity gradient within pore throats and (iii) diffusion. Particle tracking produces the positions at every time from which statistics and subsequently dispersion can be inferred. The flow field is obtained from physically representative network model of a model sediment, a dense random packing of equal spheres. We introduce mechanistic (non-stochastic) rules to determine the bond through which a particle exits a pore. The rules are essentially geometric and depend on the network flow field (rates in individual bonds and the local configuration of inlet and outlet bonds at each pore body). They enable us to attribute the contribution of convective spreading to core-scale dispersion without requiring a detailed (sub-pore) solution of the flow field through the porous medium.

The simulations provide *a priori* (no adjustable parameters) predictions of dispersion coefficient as a function of pore scale Peclet number. The predicted trends match quantitatively the experimental data found in the literature for a wide range of Peclet numbers, including the well known empirical observation that the scaling exponent has a value of about 1.2. The agreement indicates that the key features of our model correspond to the key physical phenomena causing dispersion in porous media.

The model permits rigorous attribution of the contribution of the phenomena individually, and of the interaction between combinations of phenomena. Fickian behavior of solute transport is asymptotically observed when solute particles' displacements are independent, identically distributed and random. In the limiting case of a plug-flow velocity profile in network bonds, Fickian behavior can occur without diffusion. However, this is entirely reversible. Convective spreading and diffusion act independently of each other and dispersion coefficient is the sum of the two. In the more realistic case of parabolic velocity profile in bonds, purely convective (i.e. no diffusion) spreading is not asymptotically Fickian. Diffusion is required to move solute particles from low velocity regions near pore walls. Subsequently, stream splitting is responsible for independent, random movement of solute particles and causing Fickian behavior.

In the absence of diffusion, convective spreading in porous media results in a linear dependence of D_L on N_{Pe} . Interaction between convective spreading and diffusion results in a weak non-linear dependence of D_L on N_{Pe} , in agreement with the experimental observations.

Nomenclature

β : Power law coefficient characterizing dependence of dispersion coefficient on Peclet number.

D_L : Longitudinal dispersion coefficient, m^2/s .

D_p : Particle diameter, m.

D_o : Molecular diffusion coefficient, m^2/s .

F : Formation resistivity factor.

g : Hydraulic conductivity of a bond, $m^3/s/Pa$.

l : Length of a bond connecting two neighbors, m.

μ : Fluid viscosity, Pa-s.

ϕ : Porosity.

N_{Pe} : Pore scale Peclet number, $N_{Pe} = vD_p/D_o$.

q : Flow rate through a bond, m^3/s .

r_{diff} : Magnitude of diffusive jump, m.

r_{eff} : Effective radius of a bond, m.

r_c : Radius of the largest circle to fit in a pore throat, m.

r_e : Radius of a circle having same area as a pore throat, m.

σ_z^2 : Variance of solute particles in z -direction, m^2 .

v : Interstitial fluid velocity, m/s.

\bar{v} : Average fluid velocity through a bond, m/s.

References

- Acharya, R. C., van Dijke, M. I. J., Sorbie, K. S., Van der Zee, S. E. A. T. M. and Leijnse, A.: "Quantification of dispersion by upscaling Brownian motion of tracer displacement in a 3D pore-scale network model", *Advances in Water Resources*, 30 (2), 199 – 213, (2007).
- Bear, Jacob: *Dynamics of Fluids in Porous Media*, Elsevier, New York (1972).
- Bijeljic, B., Muggerridge, A. H. and Blunt, M. J.: "Pore-scale modeling of longitudinal dispersion", *Water Resources Research*, Vol. 40, W11501 (2004).
- Bijeljic, B.: Personal Communication (2007).
- Bruderer, C. and Y. Bernabe: "Network modeling of dispersion: Transition from Taylor dispersion in homogeneous networks to mechanical dispersion in very heterogeneous ones", *Water Resources Research* 37(4): 897-908 (2001).
- Bryant, S. L., King, P. R. and Mellor, D. W.: "Network model evaluation of permeability and spatial correlation in a real random sphere packing", *Transport in Porous Media*, 11, 53-70, (1993).
- Coats, K. H., C. H. Whitson and L.K. Thomas: "Modeling conformance as dispersion", paper SPE 90390 presented at the SPE Annual Technical Conference and Exhibition, Houston, TX, (Sep 26-29 2004).
- Cenedese, A. and Viotti, P.: "Lagrangian analysis of nonreactive pollutant dispersion in porous media by means of particle image velocimetry technique", *Water Resources Research*, 32 (8), 2329-2343, (Aug., 1996).
- Chandrasekhar, S.: "Stochastic problems in physics and astronomy", *Rev. Mod. Phys.*, 15, 1-89, (1943).
- Duplay, R. and Sen, P.N.: "Influence of local geometry and transition to dispersive regime by mechanical mixing in porous media", *Physical Review E*, 066309, (2004).
- Jha, R. K.: *Investigation of Local Mixing and its Influence on Core Scale Mixing*, Ph. D. dissertation, The University of Texas at Austin (2008).
- Jha, R.K., John, A. K., Bryant, S. L. and Lake L. W.: "Flow reversal and mixing", SPE 103054 presented at SPE ATCE held at San Antonio, Texas, (Sep. 2006). To be published in SPE Journal (Sep., 2008).
- John, A. K., Lake, L. W., Bryant, S. L. and Jennings, J. W.: "Investigation of field scale dispersion", paper SPE - 113429 presented at SPE Improved Oil Recovery Symposium, Tulsa, Oklahoma, (Apr. 2008).
- Kandhai, D., Hlushkou, D., Hoekstra, A. G., Soot, P. M. A., Van As, H. and Tallarek U.: "Influence of stagnant zones on transient and asymptotic dispersion in macroscopically homogeneous porous media", *Phys. Rev. Lett.*, 88(23), (2002).
- Khrapitchev, A. A. and Callaghan, P. T.: "Reversible and irreversible dispersion in a porous medium", *Phys. Fluids*, 15(9), 2649–2660, (2003).
- Koch, D. L. and Brady, J. F.: "Dispersion in fixed beds", *J. Fluid Mech.*, 154, 399-427, (1985).
- Lake, L. W.: *Enhanced Oil Recovery*, Prentice Hall, NJ, (1989). Available through the author.
- Lebon, L., Leblond, J. and Hulin, J. P.: "Experimental measurement of dispersion processes at short times using a pulsed gradient NMR technique", *Physics of Fluids*, 9(3), 481-490, (Mar., 1997).
- Manz, B., Alexander, P. and Gladden, L.F.: "Correlations between dispersion and structure in porous media probed by nuclear magnetic resonance", *Physics of Fluids*, 11(2), 259-267, (Feb., 1999).
- Moroni, M. and Cushman, J. H.: "Three dimensional particle tracking velocimetry studies of the transition from pore dispersion to Fickian dispersion for homogeneous porous media", *Water Resources Research*, 37(4), 873-884, (Apr., 2001).
- Perkins, T. K. and Johnston, O. C.: "A Review of Diffusion and Dispersion in Porous Media", SPE 480, SPE Journal, 3(3), 70-84 (Mar., 1963).
- Pfannkuch, H. O.: "Contribution a l' etude des deplacements de fluides miscibles dans un milieu poreux", *Rev. Inst. Fr. Pet.*, 18, 215–270,(1963).
- Sahimi, M., Hughes, B.D., Scriven, L. E. and Davis, H. T.: "Dispersion in flow through porous media, I, One-phase flow", *Chem. Eng. Sci.*, 41, 2103–2122, (1986).
- Seymour, J. D. and Callaghan, P. T.: Generalized approach to NMR analysis of flow and dispersion in porous media, *AIChE J.*, 43, 2096, (1997).
- Stõhr, M.: *Analysis of flow and transport in refractive index matched porous media*, Ph.D. thesis, Univ. of Heidelberg, Heidelberg, Germany, (2003).
- Taylor, G.: "Dispersion of soluble matter in solvent flowing slowly through a tube." *Proc. Roy. Soc. (London)* A219: 186-203. (1953).
- Thane, C.: *Geometry and Topology of Model Sediments and Their Influence on Sediment Properties*, M.S. Thesis, The University of Texas at Austin (2006).

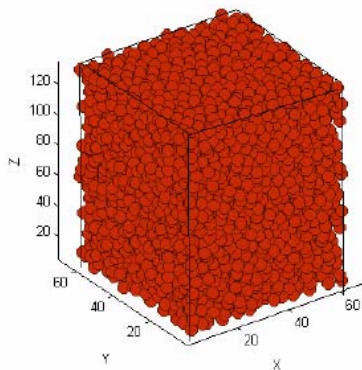


Fig. 1—A dense random packing of 10000 spheres. The radius of each sphere is 2.1918×10^{-4} m. The coordinates on x, y and z axes are in units of 10^{-4} m.

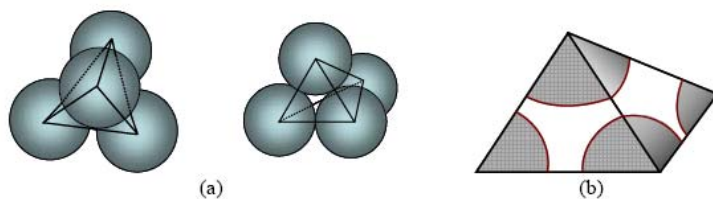


Fig. 2—Delaunay tessellation grouping together four nearest neighboring spheres. The vertices of the tetrahedra correspond to the centers of the spheres. (b) A Delaunay cell having sand grains and void space. The body of the cell can be visualized as pore body.

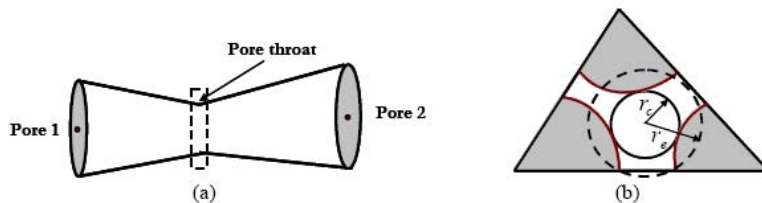


Fig. 3—(a) A converging-diverging path connecting two neighboring pores. (b) The faces are areas of narrowest constriction (throats) that connect the cell to neighboring cells. r_c is the radius of the largest circle that can fit in the constriction. r_s is the radius of the circle having same area as that of the void space. The arithmetic average of r_c and r_s is a good estimate of the equivalent radius of the bond that describes its hydraulic conductivity.

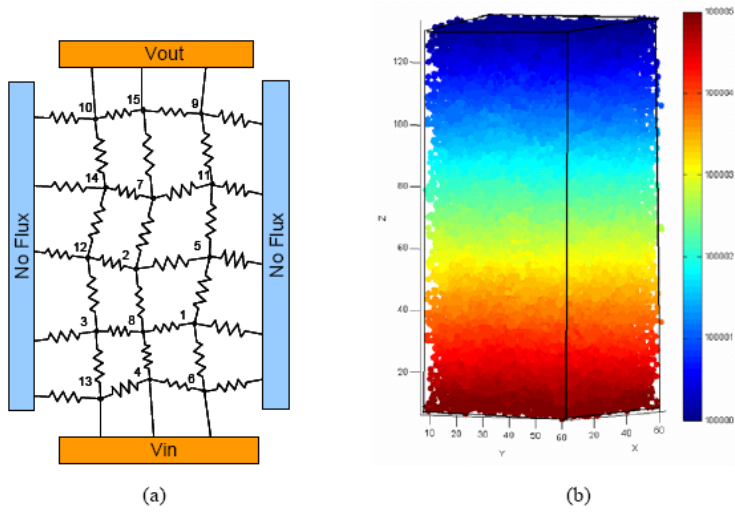


Fig. 4—(a) A schematic diagram for the physically representative network as a network of resistances. (b) The flow-potential at each pore in the network for steady-state, single-phase flow in the z direction, with no-flow boundaries on the side faces. The coordinates on x , y and z axes are in the units of 10^{-4} m.

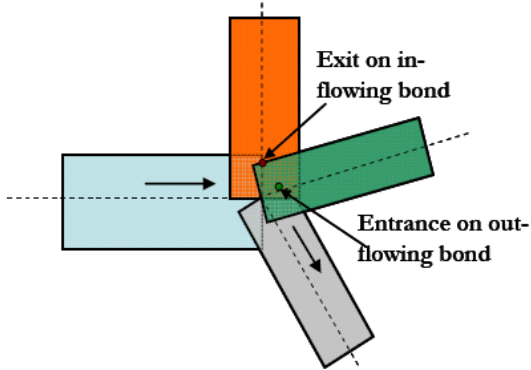


Fig. 5—Intersecting bonds at a pore body. An exit point on an inflowing bond is mapped on an entrance point on an out-flowing based on deterministic rules.

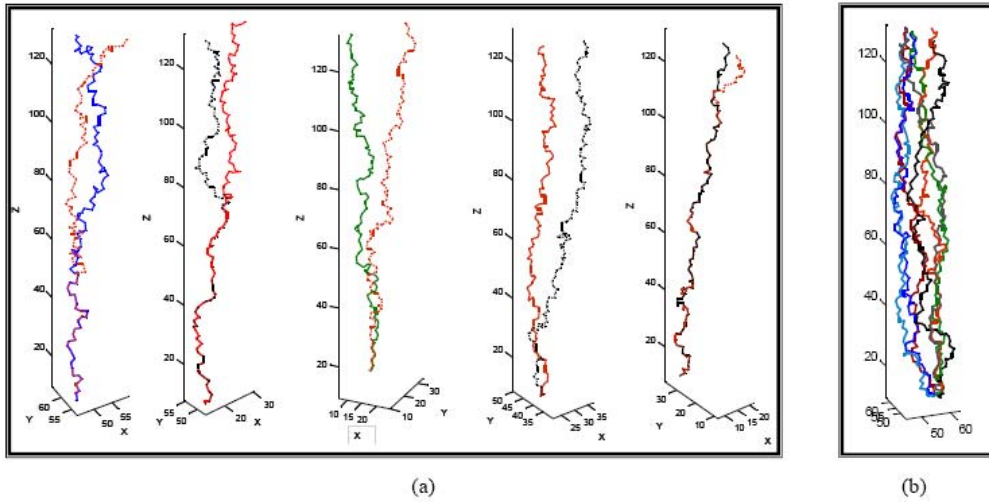


Fig. 6—(a) Paths of five different pairs of neighboring particles, each beginning in the same pore, but not at the same mathematical point. Flow is from bottom to top, with sealed sides. Bonds have plug-flow velocity profiles (no radial gradient in velocity) and diffusion is zero. Particle paths split their paths after traveling together for some number of pores. (b) Paths of several particles starting at different positions in the same pore. Particles' paths are independent of each other. If each convective step is independent and has same global statistics, solute particle displacements will be normally distributed.

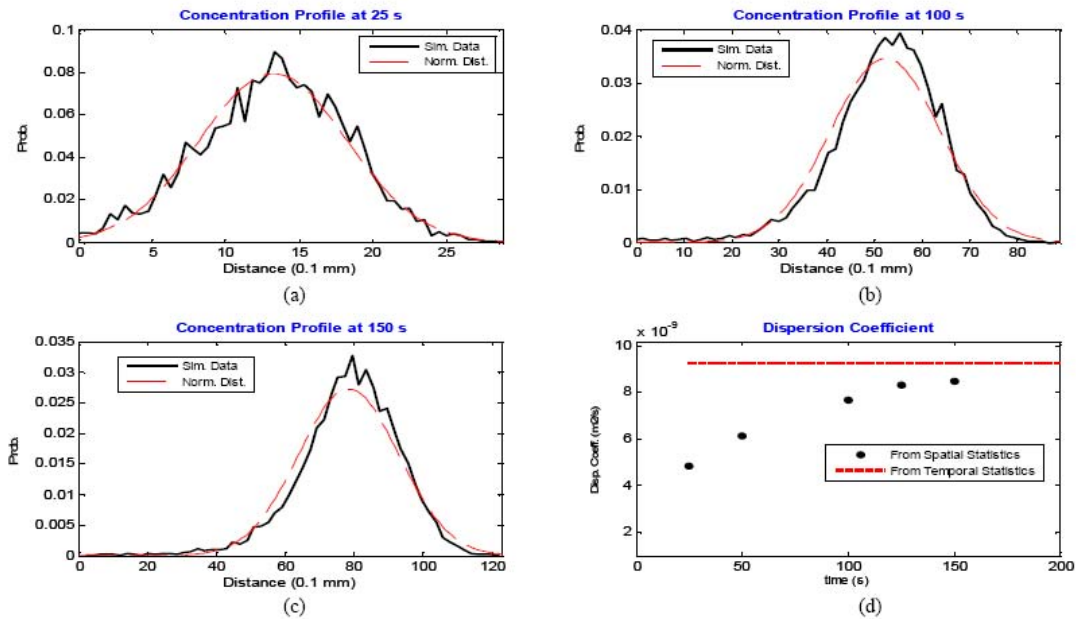


Fig. 7—(a)-(c) Scanned spatial distribution of solute particles traveling through the physically representative network for plug flow in the network bonds and $D_0 = 0 \text{ m}^2/\text{s}$. Normally distributed curves having the same mean and standard deviation as the actual data are also shown for comparison. (d) Dispersion coefficient as evaluated from spatial (dots) statistics for several times. The dotted line represents the dispersion coefficient obtained from temporal statistics. The asymptotic dispersion coefficient obtained from spatial statistics is very close to that obtained from temporal statistics.

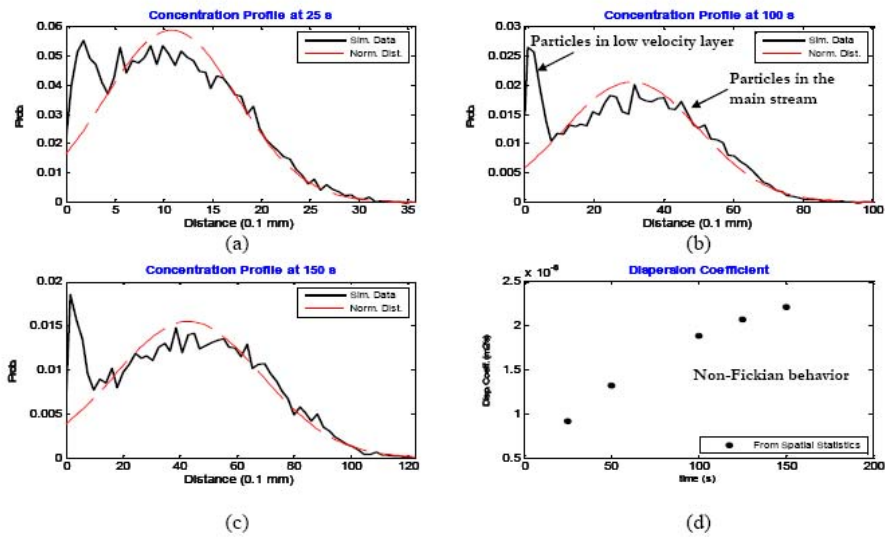


Fig. 8—(a)-(c) Scanned spatial distribution of solute particles for parabolic flow in network bonds and $D_0 = 0 \text{ m}^2/\text{s}$. The first peak in the distribution at small distance corresponds to particles in the slow velocity regions near the pore walls. Other particles that are free to move form a second peak. Dispersion is not Fickian in this case. (d) Dispersion coefficient as evaluated from spatial statistics.

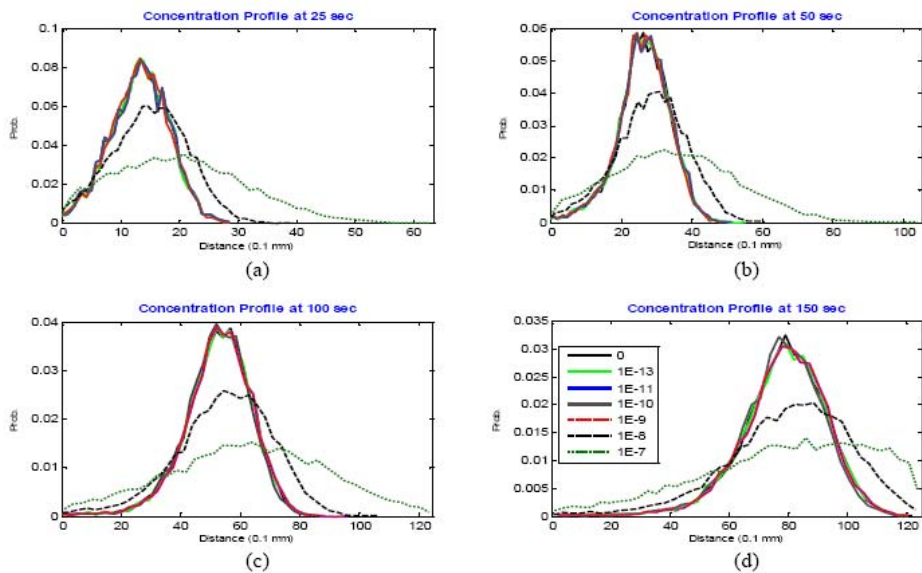


Fig. 9—Effect of diffusion on spatial statistics of solute particles for plug flow profile in bonds. Diffusion has negligible impact unless its magnitude becomes significant as compared to mechanical dispersion. All diffusion coefficients shown in the legend are in m^2/s .

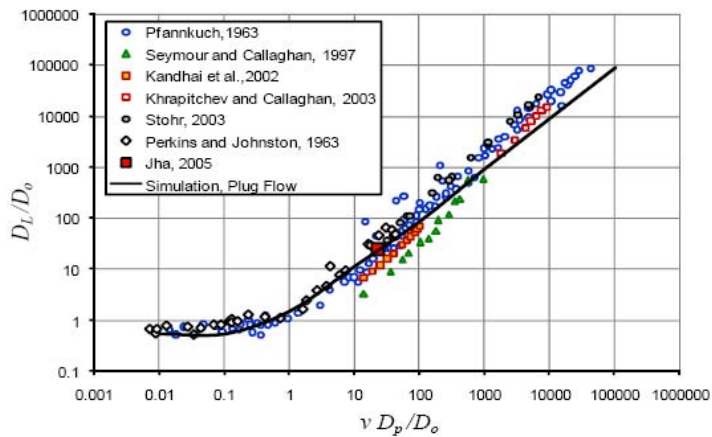


Fig. 10—Comparison of dimensionless dispersion coefficients simulated with plug flow in bonds in a physically representative network of bead pack (radius 2.1918×10^{-4} m) and experimental data in the literature.

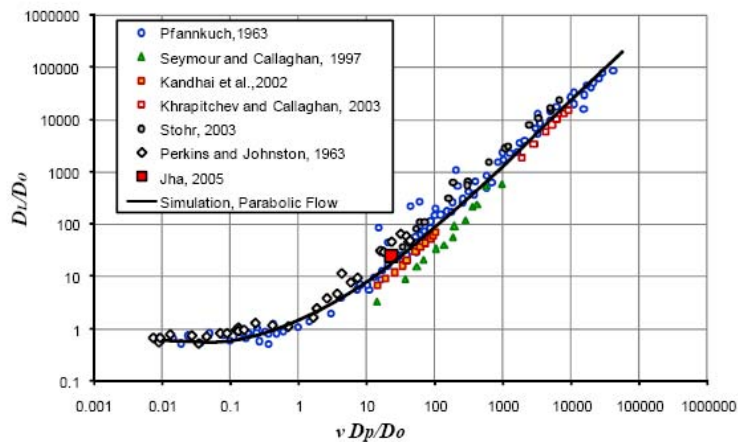


Fig. 11—Comparison of dimensionless dispersion coefficient simulated with parabolic flow in bonds and experimental data in the literature. The simulated data quantitatively matches with the experimental data for all range of Peclet numbers.

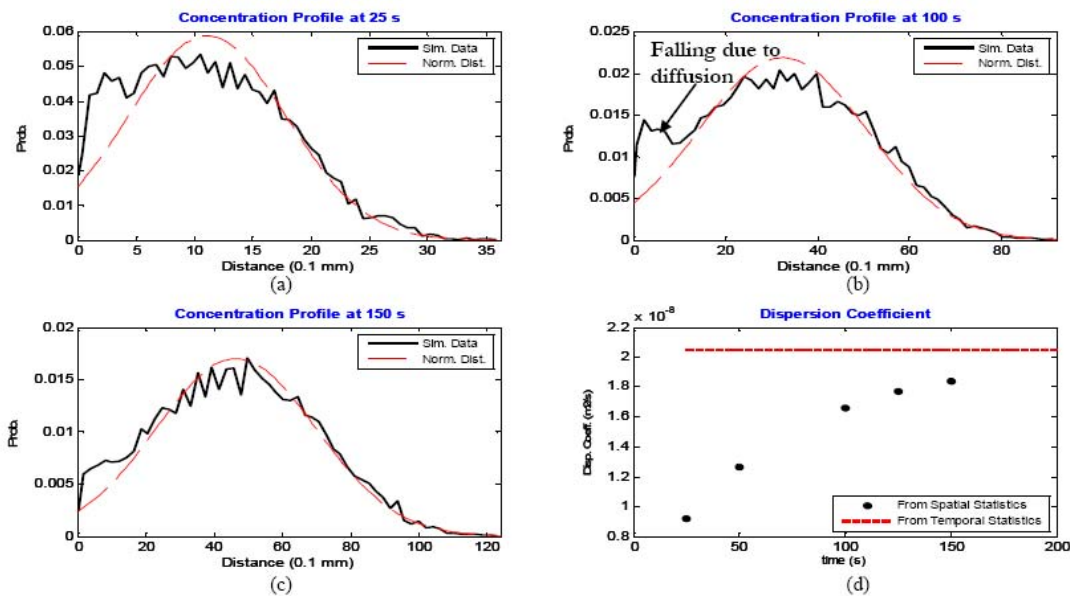


Fig. 12—(a)-(c) Scanned spatial distribution of solute particles for parabolic flow in the network bonds and $D_0 = 10^{-13} \text{ m}^2/\text{s}$. The first peak corresponds to particles in the slow velocity regions near the pore walls starts falling because of diffusion. Dispersion is asymptotically Fickian at large times. (d) Dispersion coefficient as evaluated from spatial statistics.

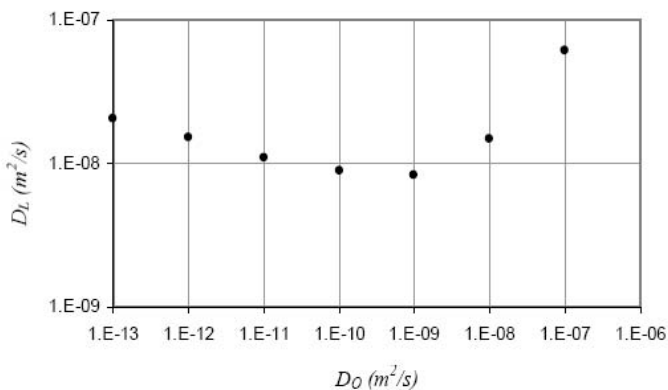


Fig. 13—Change in dispersion coefficient with diffusion coefficient for parabolic velocity profile in bonds. Dispersion coefficient decreases with diffusion unless diffusion becomes significant in magnitude as compared to mechanical dispersion.

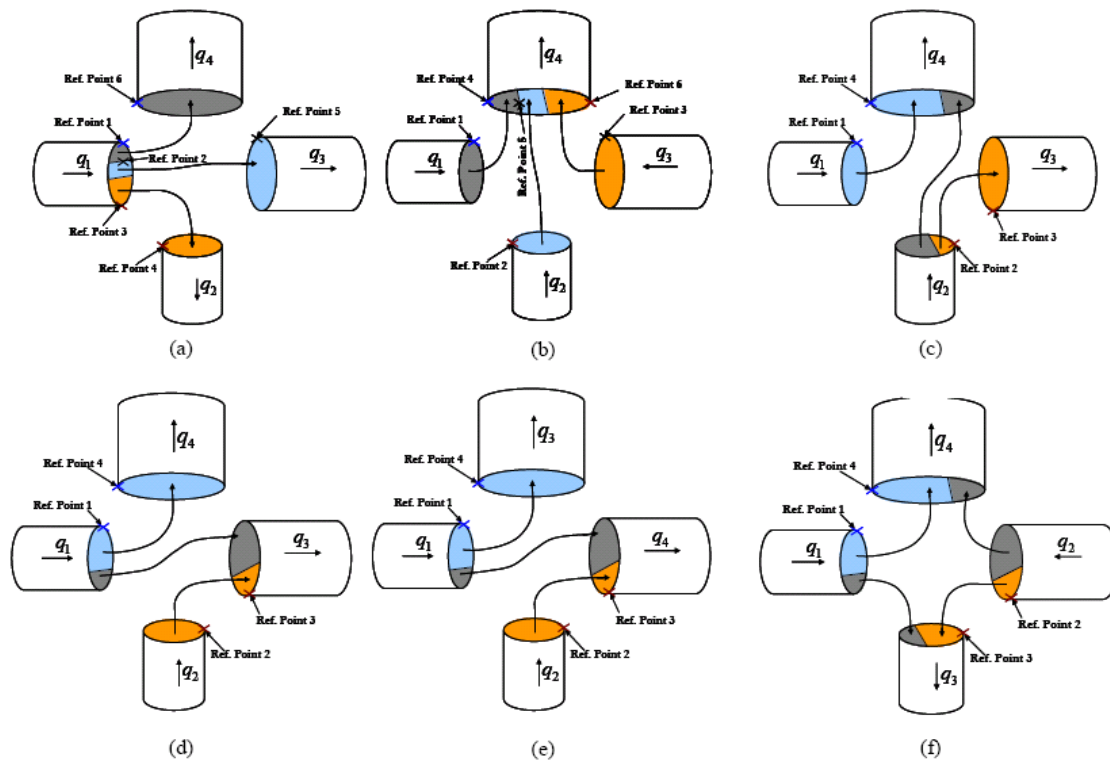


Fig. 14—Flow configurations at a pore body.

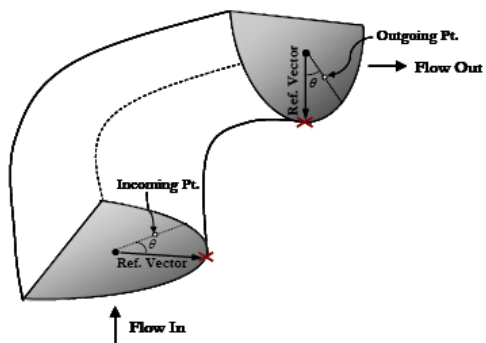


Fig. 15—Marking the outgoing point based on reference angle and relative radial distance of the incoming point.

Topic 3a: Flow reversal tracer tests

SUMMARY

Dispersivity data compiled over many lengths show that values at typical interwell distances are about two to four factors of ten larger than those measured on cores. Such large dispersivities may represent significant mixing in the reservoir or they may be a result of convective spreading driven by permeability heterogeneity. The work in this paper uses the idea of flow reversal to resolve the ambiguity between convective spreading and mixing. We simulate flow reversal tests for tracer transport in several permeability realizations using particle tracking simulations (free from numerical dispersion) on three-dimensional, high resolution models at the field scale.

We show that convective spreading, even without local mixing, can result in dispersion-like mixing zone growth with large dispersivities because of permeability heterogeneity. But for such cases, the dispersivity estimated on flow reversal is zero. With local mixing (diffusion or core scale dispersion) the dispersivity value on flow reversal is non-zero and also much larger than typical core values. Layering in permeability, while increasing the convective contribution to transport, also enhances mixing by providing larger area in the transverse direction for diffusion to act. This suggests that in-situ mixing is an important phenomenon affecting the transport of solutes in permeable media even at large scales. Dispersivity values increase with scale mainly because of the increase in the correlation in the permeability field but they could also apparently appear to do so because the Fickian model fails to capture the mixing zone growth correctly at early times.

The results and approach shown here could be used to differentiate between displacement and sweep efficiency in field scale displacements, to ensure accurate representation of dispersive mixing in reservoir simulation and to guide upscaling workflows. The flow reversal concept motivates a new line of inquiry for lab and field scale experiments.

1. Introduction

Dispersion is the in-situ mixing of chemical components as they are transported through porous media. It results from the combined effects of molecular diffusion and fluid velocity gradients (Taylor, 1953). The recovery efficiency of processes like miscible gas or chemical flooding depends partly on the mixing which an injected slug undergoes. For example, Solano *et al.* (2001), performing a range of one dimensional and two dimensional simulations of enriched gas floods, show that the recovery difference between the cases studied could be up to 8% of the original oil in place depending on the degree of dispersion. Similar observations have been made by others (Haajizadeh *et al.*, 1998; Jessen *et al.*, 2002; Moulds *et al.*, 2005). Dispersion is also an important effect in water injection where mineral scales are formed by mixing of injected and reservoir brines (Sorbie and MacKay, 2000; Delshad and Pope, 2003), in the underground storage of gases where mixing of the injected and in-situ gas changes the quality of the stored gas (Verlaan, 1998), and in proposed methods of enhanced natural gas recovery by injecting anthropogenic CO₂ (Oldenburg *et al.*, 2001).

Modeling any of the above processes requires an accurate estimation of the degree of mixing and its impact, relative to other transport mechanisms, at the length scale under consideration (core, grid block size or interwell distance). This is straightforward for a

homogeneous system e.g. a single bounded flow unit where the results from the core scale are easily translated to the field scale. In heterogeneous media, despite considerable work done over the years, significant ambiguity exists in addressing this problem. Dispersivities measured using interwell tests show values at the field scale that are two to four factors of ten larger than those at the core scale. But these values were obtained by treating the flow unit as one homogeneous. One dimensional analytical models were used to match the effluent concentrations because the permeability description was unknown or because computational considerations necessitated an upscaled description. So, such large dispersivity values could be a result of convective **spreading** because of permeability heterogeneity (which causes widely varying arrival times of injected chemical at the well, followed by mixing within the well). Alternatively, they could be the consequence of significant **mixing** or dilution in the reservoir (driven by diffusion).

In this paper, we present concepts and results that address fundamental aspects of this issue. Using high resolution simulations of tracer transport in three-dimensional heterogeneous permeable media, we

- Demonstrate the application of flow reversal to distinguish between spreading and mixing. The concept is described in Section 2.3. In Section 4.2 we show that, in certain cases, permeability variations alone can cause dispersion-like behavior (even in absence of diffusion). But with a flow reversal test, the dispersivities estimated in such cases are zero indicating no mixing.
- Show the influence of permeability heterogeneity (variance and auto correlation lengths), permeability anisotropy, core scale dispersivity and residence time on in-situ mixing (Section 4.3-4.7). We compare the dispersivities estimated from our simulations to those measured from field tests (Section 4.8). We argue that a large value of dispersivity is not always the result of averaging unknown permeability heterogeneity as commonly understood. There could be a significant amount of mixing occurring in the reservoir.
- Show that the dispersivity estimated using the traditional (forward flow) approach is not much affected by changes in degree of diffusion or core scale dispersion. But this does not imply that the effects of diffusion are negligible. In such cases, the dispersivity value obtained on flow reversal are always non-zero and also much larger than typical core scale values (Section 4.4). We argue that this is the effect of transverse mixing across streamlines which has been neglected in previous works.
- Show that dispersivity values increase with increase in the correlation lengths of the permeability field (Section 4.7 and 4.8). This also increases the amount of mixing as indicated by the dispersivities estimated from flow reversal tests.
- Show that dispersivity values can also appear to increase with scale because of the inadequacy of the Fickian dispersion model in capturing the early time behavior of the injected solute (Section 4.7 and 4.8)

We consider tracer transport in a porous medium with uniform porosity and spatially varying permeability under single phase, incompressible flow at constant density. The tracer is assumed to be volumeless and without adsorption. The transport calculations are free from numerical dispersion. Section 2 expands on the problem description and provides the basis of our approach. The computational scheme used is described in Section 3. Section 4, shows the evolution of longitudinal dispersivities for

various cases. In Section 5, the implications of our results are discussed and compared with existing works.

2. Concepts and Definitions

2.1 Diffusion and Dispersion. Diffusion is the spontaneous net movement of particles driven by a concentration gradient. The mechanism of diffusion is Brownian motion and is described by Fick's law:

$$\frac{\partial c}{\partial t} = D_{mol} \frac{\partial^2 c}{\partial x^2} \quad (1)$$

Here c is the local (point scale) concentration of the injected chemical and D_{mol} its diffusion coefficient. Diffusion increases entropy, decreases Gibbs free energy and is the fundamental mechanism responsible for mixing. By mixing we mean dilution or reduction in local concentrations. Convection (or spreading) is the movement of particles by the motion of the carrier fluid. This is sometimes termed advection. Spreading implies redistribution of local concentrations. Both mixing and spreading involve the distribution of solute in a solvent but in mixing the volume occupied by the solute increases whereas in spreading the volume occupied by the solute remains the same.

G.I. Taylor (1953) analyzed the mixing of a solute introduced into a solvent slowly flowing in a circular capillary tube. He showed that when certain conditions are met, a quasi-equilibrium is established where convection and diffusion interact in a manner with the net effect appearing as if the solute were in plug flow despite the radial variations in velocity. The radial concentration variations are almost zero making the local and averaged concentrations the same. This phenomenon could be characterized as an unsteady diffusion process governed by the same equation (Eq. 1) but with an effective diffusion coefficient whose value depends on the flow profile and is much larger than D_{mol} . This phenomena is termed dispersion. It must be noted that in the absence of diffusion, such a condition would never be reached. In this paper, we use the term dispersion to imply enhanced diffusion or mixing. The same idea applies to transport in porous media (Aronofsky and Heller, 1957) with the dispersion coefficient for an isotropic medium now being a tensor:

$$D = (\alpha_l |V| + D_{mol}) I + \frac{\alpha_l - \alpha_t}{|V|} VV \quad (2)$$

where D is the dispersion coefficient of the porous medium, I is an identity matrix and V is the average fluid velocity vector. The value of D_{mol} is adjusted for the porous medium. α_l and α_t are the longitudinal and transverse dispersivities which are assumed to be fundamental constants for the medium (Bear, 1961). In experiments done on homogeneous sand columns it was found that α_l is of the order of magnitude of the average grain size and α_t is about ten to thirty times smaller than α_l (Perkins and Johnston, 1963). The longitudinal dispersivities of consolidated media are about a centimeter (Arya, 1988).

Dispersion entails averaging. In using Eq. 1 for dispersion, we have tacitly invoked the continuum hypothesis. Local scale now implies the scale of the representative elementary volume (Bear and Verruijt, 1987). At the continuum scale, the dispersive flux captures the combined effect of diffusion and velocity variations. The dispersion coefficient is governed by averaged velocities and it describes averaged

concentrations. Its magnitude of the dispersion coefficient is largely governed by the velocity variations. Without them, the coefficient of dispersion would be the same as that of molecular diffusion (adjusted for the geometry of the porous medium). But without diffusion, there would be no dissipation occurring at the local scale and the dispersive flux would simply be representing the convective spreading caused by local velocity variations.

So, following Lake (1989), the transport equation for a chemical component in a homogeneous one-dimensional porous medium, expressed in dimensionless terms, is

$$\frac{\partial C_D}{\partial t_D} = \frac{1}{N_{Pe}} \frac{\partial^2 C_D}{\partial x_D^2} - \frac{\partial C_D}{\partial x_D} \quad (3)$$

where the C_D is the concentration (limited between 0 and 1) at any point normalized to the injection concentration. The chemical is injected uniformly over the entire inlet face. The dimensionless time (pore volumes injected) is

$$t_D = \frac{qt}{AL\phi} = \frac{Vt}{L} \quad (4)$$

Dimensionless distance (limited between 0 and 1) is

$$x_D = \frac{x}{L} \quad (5)$$

The dimensionless measure of the degree of convective to dispersive transport is the Peclet number:

$$N_{Pe} = \frac{VL}{D_l} \quad (6)$$

where D_l is the longitudinal dispersion coefficient. A high Peclet number (>500) yields a sharp displacement front and a low number (<100), a more spread out one. Defining the dimensionless mixing zone length as

$$\Delta x_D = (x_{C_D=0.9} - x_{C_D=0.1}) / L \quad (7)$$

the analytical solution to Eq. 3 (to its first order approximation) can be manipulated to give

$$\Delta x_D = 3.625 \sqrt{\frac{t_D}{N_{Pe}}} \quad (8)$$

which, using Equations 6 and 2, can also be expressed as

$$\Delta x_D = 3.625 \sqrt{\left(\frac{\alpha_l}{L}\right) t_D} \quad (9)$$

Hence an experiment where the mixing zone grows with square root of time can be matched using the Fickian model for dispersion. In a discrete sense, considering the solute to be an ensemble of particles, the mixing zone represents the standard deviation of the particle x-locations. So another way of restating the above is that an experiment where the particle x-variance grows linearly with time can be matched with the Fickian model for dispersion.

2.2 Dispersion and Reservoir Heterogeneity. Consider a miscible displacement in a homogeneous flow unit of length 100 m. If the dispersivity were say 1 cm (core measured value), the Peclet number would be 10,000. This would result in a

dimensionless mixing zone of 0.03625 at one pore volume injected (Eq. 8), an insignificant fraction of the length. For a heterogeneous medium of the same length, composed of many such rock types, the key question is what value of dispersivity should be used to estimate the mixing zone size if Eq. 3 were to be used. Dispersivities are inferred for such cases in the field using interwell tracer tests (see for example Chrysikopoulos *et al.*, 1990). Data compiled from results of such tests published over the past few decades (Schulze-Makutch, 2005) are shown in Fig. 1. This data set represents many formation types and length scales. Despite the scatter, dispersivities appear to increase with system length. At 100 m, the range of dispersivities is 5-50 m. This means that the smallest possible dimensionless mixing zone size at one pore volume would be 0.81 which is quite large. But does this mean that there is significant mixing taking place?

Probably not, because the displacements during the tests are unlikely to be entirely in the dispersive mixing regime. The use of Eq. 3 to interpret them is probably incorrect because this counts the contribution of convective spreading (because of permeability variations) as a dispersive mixing effect. But it must be noted that some of the measurements used point samples from sources injecting at small flow rates (Arya *et al.*, 1988). Also, velocities in typical field displacements are about 1 ft/D (about 3×10^{-4} cm/s). At this rate the effects of molecular diffusion, acting over the long travel times between wells, could compound and lead to significant reduction in local concentrations. Layering increases the convective contribution to transport but, by increasing the area available in the transverse direction, also increase the dilution of the solute (Lake and Hirasaki, 1981).

So, the question of how much mixing takes place in a heterogeneous medium at the field scale has no clear answer. If all the heterogeneity could be represented explicitly and local mixing be modeled only by diffusion or core scale dispersion, then the question would be irrelevant. But even if the computational resources were available for such an undertaking, one must consider the cost of collecting and assimilating data at such a fine scale. As long as upscaled descriptions are in use, one must address this issue. Our work is set in this context.

2.2 Convection, Dispersion and Flow Reversal. We use the idea of flow reversal to distinguish between mixing and spreading. For an incompressible fluid, in the absence of temperature effects (which cause changes in local fluid viscosity) and turbulence effects (which cause temporal variations in the local flow field), the local velocities reverse themselves on reversing the boundary conditions (Flekkoy, 1997). With no diffusion, the concentration history observed on flow reversal at the inlet would be same as the original input. For this case, particles return back on the same streamline. Convective reversibility has been well illustrated in unmixing demonstrations for circular Couette flow (Heller, 1960; Taylor, 1972), for slow, laminar flows between disordered arrays of cylinders (Hiby, 1960, Flekkoy *et al.*, 1996) and for neutrally buoyant particles in dilute suspensions (Cox and Mason, 1971).

We assume convective reversibility at low Reynolds number flows in porous media. Numerical simulations have validated this assumption (Jha *et al.*, 2006) but it has not been experimentally demonstrated. If mixing occurs, then particles jump across streamlines and the concentration history on flow reversal is dispersed. Any initial solute

distribution, once mixed, cannot be reconstructed by reversing the direction of the flow. Referring to Fig. 2, the traditional approach of estimating the dispersivity of a medium is using a slug or a step change in concentration (as shown) with a constant flow direction. This is termed a transmission experiment and can be interpreted using Eq. 3. All the values in Fig. 1 are transmission dispersivities. One could perform the same experiment but reverse the flow direction before the injected solute reached the forward outlet. This is termed an echo test. The effluent is recovered at the inlet face. Assuming no experimental artifacts, if mixing was not occurring then the effluent concentration history would also be a step change (same injection). If mixing were occurring, then on flow reversal the fluids would continue mixing (not unmix) and a variation in concentrations would be seen in the effluent history. In this paper, we use Eq. 3 to also estimate echo dispersivities. A zero echo dispersivity (or dispersion coefficient) would imply no mixing and only convection. An echo dispersivity value equal to the transmission value would imply well mixed transport (effective diffusion).

Hulin and Plona (1989) and Rigord *et al.* (1990) studied the reversibility of tracer dispersion in careful experiments on bead packs and sandstones. They observe that homogeneous porous materials do not exhibit convective reversibility: the echo dispersion (after flow reversal) is the same as transmission dispersion over a wide range of Peclet numbers. In heterogeneous materials, they observe echo dispersion to be less than transmission, implying that the equilibrium condition to ensure the use of Eq. 3 was not met. They argue that a small amount of diffusion is sufficient to cause irreversibility. Heller (1972) also points out the influence of diffusion on mixing and reversibility. Mahadevan *et al.* (2003), estimating echo dispersivities from single well tracer test data, observed values in the range of 0.1-1 m at a length scales in the range of 10-50 m. These are much larger than the range of core scale values (Fig. 3). This suggests that mixing could be significant even at the field scale. There is some uncertainty in the use of the tracer data because of fluid drift and transient flow effects during the test. Also, the corresponding transmission values for their cases are not available for comparison. In this work, we use numerical simulations to investigate the significance of dispersive mixing at the field scale and test their observations over a range of reservoir descriptions.

3. Computational Approach

3.1 Overview. We simulate transmission and echo tests for tracer injection in field scale heterogeneous media. The degree of local mixing is varied from zero (purely convective) to core scale dispersion (well mixed). The dispersivities inferred from the simulations are compared with core scale dispersivities (input values) and the field data (Fig. 1) to make our conclusions.

A three-dimensional Cartesian grid is used. The grid spacing is uniform and grid cells are equidimensional. We controlled the system size and aspect ratio by changing the number of cells in each direction. Primary input variables are the medium dimensions, the permeability field, the flow boundary conditions and the degree of local (now meaning at the scale of a grid cell) mixing (diffusion and/or core scale dispersion). The permeability field is characterized by a correlation structure (having a short range and long range component), variance and anisotropy. We assume that sub-cell permeability variations are negligible and local dispersion, when introduced, implies mixing. For each case, we generate the permeability field, compute the flow field and then use the flow velocities in the transport calculations. A Lagrangian particle tracking scheme is used to

model the transport of tracer through the computed flow field. The details of each individual step are described in the following sections.

Our computing environment was a Linux cluster at the Texas Advanced Computing Center at the University of Texas. Each compute node is a Dell Power Edge 1955 blade containing two Xeon Intel Duo-Core 64-bit processors running at 2.66GHz and 8 GB of memory. The peak performance is rated at about 10 GFLOPS/processor core.

3.2 Permeability field generation. The correlation structure is modeled with a sum of short and long-range structures

$$\gamma(h) = s_{short}\gamma(h, r_{short}) + s_{long}\gamma(h, r_{long}) \quad (10)$$

where γ is the semi variance of the permeability at distance h (a vector), s is the variance or sill parameter and r is the range parameter (a vector). Each structure is described by an exponential semivariogram,

$$\gamma(h, r) = s \left[1 - \exp\left(-\frac{h}{\|r\|}\right) \right] \quad (11)$$

We used this model because measurements on outcrops typically show multiple scales of variability (Tidwell and Wilson, 2000; Willis and White, 2000; Jennings *et al.*, 2000). A stochastic simulation technique based on spectral transforms is used to generate permeability field realizations. The input correlation structure is converted into a covariance function, which is sampled on the grid used for the flow calculations. The fast Fourier transform (FFT) algorithm is used to produce the amplitude spectrum of the permeability covariance function. This is multiplied by the FFT of an uncorrelated Gaussian noise and inverted to produce a realization which has a standard normal distribution. This data is transformed to a lognormal distribution of the desired mean and variance. The z -direction permeabilities are multiplied by the desired anisotropy ratio. All the points in the permeability realization thus produced are globally conditioned. The method is fast even for large number of grid points simulated. This approach is detailed in Appendix C of Jennings *et al.* (2000).

3.3 Flow field generation. The flow equation solved is

$$\nabla \cdot u = 0 \quad (12)$$

where the Darcy velocity is

$$u = -\frac{k}{\mu} \nabla p \quad (13)$$

Constant pressures are specified on the boundary cell faces in the x -direction and the transverse boundaries are closed to flow. Thus the principal direction of flow is aligned with the x -axis. The fluid viscosity is 1 cp and density 1 g/cm³ (both constant). The permeabilities are assigned directly to the cell faces instead of cell centers to avoid a change in variability because of harmonic averaging with neighboring cells (Romeu and Noetinger, 1995). The overall pressure gradient of 1 psi/m is imposed and the mean permeability is set at 1700 md to produce an average x -velocity close to 1 m/d for all cases.

The code we used to compute the flow field is Parssim (Arbogast, 1998), developed by the Center for Subsurface Modeling of the Institute for Computational Engineering and Sciences at The University of Texas at Austin. It is designed to accurately simulate incompressible, single phase flow and reactive transport of chemical components through porous media (Arbogast *et al.*, 1996). Parssim uses a logically rectangular cell-centered finite difference procedure to discretize the flow equation. For large problems it has the option of using multiple processors to compute the solution based on a domain decomposition approach. This was the main advantage of using Parssim apart from the flexibility of easily specifying pressure boundary conditions on entire boundaries.

The velocities at each cell face obtained from Parssim are written to separate files, which are used as an input in the transport calculations. At the desired time of flow reversal the velocity direction is reversed instantaneously. The magnitudes of the velocities are constant throughout the transport simulation.

3.4 Transport calculations. We use a random walk particle tracking method to simulate tracer transport. This method has been used successfully by the hydrology community to simulate mass transport (Tompson and Gelhar, 1990). Convection is modeled by integrating particle displacement in the local velocity field over a given time step. Dispersion is modeled by an appropriately scaled particle Brownian motion. Further details of this approach and our implementation are in the Appendix. The code's solution was in good agreement with known analytical solutions: the convection-dispersion equation and Taylor's dispersion in a rectangular duct (John, 2008). Most of our simulation runs were completed in about 3 hours for the cases described below.

Compared to finite difference and finite element methods, this method has certain features which made it an appropriate choice for this problem: it is free from numerical dispersion, is stable in problems dominated by advection and is much more computationally efficient because each particle calculation is done independently. The mean distance traveled by the particle ensemble in our setup is limited by the arrival of the particles at the outlet boundary. This meant that a flow domain much larger than the desired distance of investigation was required, especially in highly heterogeneous cases. Also, for the flow reversal cases, it proved convenient to choose the center of the domain as the origin of the particles. This eliminated the possibility of particles exiting through the inlet boundary.

Particle Tracking Calculations

The idea of applying the random walk particle tracking method to solute transport problems is based on an analogy between the convection-dispersion equation for solute transport and the Fokker-Planck equation for diffusion (Uffink, 1990; Risken, 1989). The mass of the injected solute is represented by a finite number of particles. The particles are displaced in space by the action of a velocity field (convection) and Brownian motion (dispersion). The tracking in three dimensions is based on the equation

$$X_p(t + \Delta t) = X_p(t) + A(X_p, t) \cdot \Delta t + B(X_p, t) \cdot Z \sqrt{\Delta t} \quad (\text{A.1})$$

where X_p is the particle position vector [L], A is a drift vector [L/T], B is a tensor [L/T^{1/2}] defining the strength of diffusion and Z is a vector of independent normally distributed random numbers with zero mean and unit variance. To simulate tracer

transport, choose A and B such that the mass density of the particles satisfies the convection-dispersion equation

$$\frac{\partial(\phi c)}{\partial t} + \nabla \cdot (\phi v c) - \nabla \cdot (\phi D \cdot \nabla c) = 0 \quad (\text{A.2})$$

where D is the local dispersion tensor given by

$$D = (\alpha_l |v| + D_{mol}) I + \frac{\alpha_l - \alpha_t}{|v|} v v \quad (\text{A.3})$$

and α_l and α_t are the longitudinal and transverse dispersivities, respectively. D_{mol} is the molecular diffusivity of the porous medium. It has been shown that Eq. A.1 satisfies Eq. A.2 by setting A and B as (LaBolle *et al.*, 1996)

$$A = v + \nabla \cdot D + \frac{1}{\phi} D \cdot \nabla \phi \quad (\text{A.4})$$

$$2D = B \cdot B^T \quad (\text{A.5})$$

When computing A, we neglect the gradients in D and the gradients in porosity are zero because of the constant porosity assumption. The drift term (Eq. A.4) hence consists of only the velocity term. The velocities are obtained from the flow simulation step (Section 3.3). To compute the convective displacement, we integrate over the local velocity field for a given time step. Only the face centered velocities and cell centered gradients are used in this calculation. To be consistent with the fluid flow equation, we take each component of the velocity to vary linearly within a cell in its respective direction (Pollock, 1988).

$$v_x = g_x x + v_o \quad (\text{A.6})$$

where x is the distance of the particle from the cell face, v_o is the velocity at the cell face and g_x is the gradient in the x-velocity. At any particle location

$$\frac{dx}{dt} = v_x \quad (\text{A.7})$$

Starting with the particle at location 1 (distance from the cell face in x-direction being x_1), the new location x_2 can be found by integrating Eq. A.7 over a time step size of Δt

$$\int_{x_1}^{x_2} \frac{dx}{g_x x + v_o} = \int_0^{\Delta t} dt \quad (\text{A.8})$$

or

$$\frac{1}{g_x} \ln \left| \frac{g_x x_2 + v_o}{g_x x_1 + v_o} \right| = \Delta t \quad (\text{A.9})$$

This gives

$$x_2 = \frac{1}{g_x} \left[v_o \left(e^{g_x \Delta t} - 1 \right) \right] + e^{g_x \Delta t} x_1 \quad (\text{A.10})$$

Similar expressions apply for the y and z components of the particle position inside a cell. If the particle crosses a cell boundary in a given time step then these expressions are modified to account for the change in cell velocities and gradients (John, 2008). We found this approach to be more accurate and efficient in highly heterogeneous realizations compared with approaches which treat the velocity as constant over a given time step.

To compute the dispersive displacement, we first estimate D using the approach suggested by Tchelepi [1994]. An orthogonal co-ordinate axes system, aligned in the direction of v , is temporarily setup at the current particle location. In this system, D reduces to its diagonal form making it much simpler to solve Eq. A.5 for B . The dispersive displacements are computed in this system and transformed to the global co-ordinate system. Boundary conditions were enforced using a reflection condition on the y and z faces and by ensuring that the particles don't exit the system in the x -direction. This ensures global mass conservation.

To generate uniform deviates, we use a random number generator routine adapted from Press *et al.* (1992) which has a long period ($>10^9$). The time step size is chosen to limit the particle displacement to 1/1000th of the cell size. In all our simulations we use a uniform grid with equidimensional cells.

Particles are introduced uniformly over the entire y - z face at the center of the flow domain. As they are transported, statistics of particle x -positions are computed at desired time intervals. The dispersion coefficient is estimated as

$$D_l = \frac{\sigma_x^2}{2t} \quad (\text{A.11})$$

where σ_x^2 is the x -variance of the particle ensemble. To calculate the dispersivities, we assume that Eq. 2 holds true

$$\alpha_l = \frac{D_l}{|V|} \quad (\text{A.12})$$

where the mean velocity of the ensemble is computed from its mean position

$$V = \frac{\mu_x}{t} \quad (\text{A.13})$$

4. Results

4.1 Overview. We set up several cases by varying the following parameters: permeability variance, correlation lengths, anisotropy and tracer travel time (mean penetration distance). The base case dimensions are 2048 m \times 64 m \times 64 m with cell size of 1 m \times 1 m \times 1 m. This is populated with an uncorrelated permeability field (range 1 m in all directions) with variance (natural logarithm of permeability) of 1.0 and no anisotropy ($k_z = k_x$). The longitudinal dispersivity in each cell is set to be 0.01 m (following the trend in Fig. 1) and the transverse dispersivity (in y and z directions) is set to be a tenth of that (Perkins and Johnston, 1963). These values are constant for all cells. The coefficient of molecular diffusion is 1.0×10^{-4} m²/d (about the same as that of brine-water at room temperature). Ten thousand particles were used for the transport simulations.

4.2 Mixing and Spreading. For the case with uncorrelated permeabilities, Fig. 4 shows the particle positions at selected times during forward and reverse flow. The particle cloud spreads out in the x-direction as it moves forward and on flow reversal the cloud returns back to the origin (in terms of its mean position). Statistics of the particle positions are processed first to get the rate of change of variance with time (Fig. 5) from which we get the evolution of the longitudinal dispersivity with mean position of the particle cloud (Fig. 6). In forward flow, the dispersivity for the case with local mixing ($D_{mol}=1.0\times 10^{-4}$ m²/d, $\alpha_l=0.01$ m and $\alpha_t=0.001$ m within each cell) grows and reaches an asymptotic limit of 1m (transmission value) at a distance of 100 m. For this case, on flow reversal, the particle variance decreases first but then grows again with time. The particles do not return to their origin and there is a finite variance of the particle cloud at the end of the flow reversal experiment (the mean position of the cloud is the same as the initial position). The dispersivity estimated on flow reversal (echo value) is about 0.6 m (much larger than the input value of 0.01 m).

The same simulation sequence (forward and reverse flow) was repeated with the same velocity field but without local mixing ($D_{mol}=0$, $\alpha_l=0$ and $\alpha_t=0$ in each cell). The behavior during forward flow is the same as the case with local mixing as can be seen by the evolution of particle variance (Fig. 5). But, on flow reversal, the particles now return back to their origin and the echo dispersivity estimated is zero. If only the transmission results were available, then one would interpret both scenarios in the same way, i.e. one would conclude that both cases were in the transport regime where mixing was occurring. Both cases would be characterized by a dispersivity value of 1.0 m. But in the case with no local mixing, it is the spreading of the tracer because of the velocity field, which has resulted in dispersion-like behavior. There is no dissipation or dilution occurring within each cell. It is the behavior on flow reversal that shows the fundamental difference in the transport mechanism.

Crucially, the echo dispersivity for the case with local mixing is also much larger than the input dispersivity. This suggests that the variations in the velocity field significantly enhance mixing. If this were not so, then the echo dispersivity should have been close to the core scale (input) value. The transmission and echo dispersivities would lie in the overall trend of measured dispersivities (Fig. 1).

4.3 Effect of Correlation Structure. We continue with the same reservoir size and introduce correlation in the permeability fields. Two new cases are simulated by introducing a long range component in increasing proportions (refer to Eq. 10) to the uncorrelated case described above. In the first, the proportion of permeability variance in the long range structure is 20%, in the second it is 80%. The long range component has a range of 250 m in the x-direction and 5 m in the transverse directions. Sample cross sections are shown in Fig. 7. The increase in layering as the long range structure becomes dominant is apparent.

The results of the particle tracking simulations are shown in Fig. 8 plotted on a logarithmic scale. The short scale result is the same as described in Section 4.2. With the introduction of more of the long range component, the transmission dispersivity increases from 1 m to about 50 m at a length of 200 m. Neither long range case seems to have reached an asymptotic limit at this length scale because the dispersivities are still

increasing at the end of the forward flow simulation. The transmission dispersivity grows almost linearly with time. The striking feature of the flow reversal is the similar increase in magnitudes of echo dispersivities of the long range cases. Compared to a value of 0.6 m for the uncorrelated case, we now observe values that are as large as 5 m for the same total travel time. This reinforces the point made in Section 4.2: flow field variations strongly enhance the macroscopic effect of local mixing. However the ratio of echo to transmission dispersivities is much less than that of the short range case. For the uncorrelated case it was 0.6 (0.6 m/1.0 m) for the long range cases it is around 0.1 (5.0 m/50.0 m). This means that the convective contribution to particle variance is much larger than that for the uncorrelated case.

4.4 Effect of Local Mixing. To estimate the sensitivity of mixing at large scales to local mixing, we simulated the cases again with three levels of input (within cell) mixing levels: a) only diffusion, $D_{mol}=1.0\times 10^{-4}$ m²/d b) diffusion and core scale dispersion, $D_{mol}=1.0\times 10^{-4}$ m²/d, $\alpha_l=0.01$ m and $\alpha_t=0.001$ m in each grid cell c) diffusion and larger core scale dispersion, $D_{mol}=1.0\times 10^{-4}$ m²/d, $\alpha_l=0.05$ m and $\alpha_t=0.005$ m in each grid cell. The dispersivities estimated are shown in Fig. 9. The transmission behavior is almost unaffected by the degree of local mixing (within each cell) because in this direction the contribution of spreading dominates. The echo dispersivities increase with increasing local mixing but the change is not substantial. This does not mean that local mixing can be neglected; without local mixing the echo dispersivities would be zero as in Fig. 6. No dilution would be taking place, local concentrations would be large.

4.5 Effect of Permeability Variance. The results from two cases, both having the same correlation structure (20% long range + 80% short range variance) but one having a smaller variance (0.3 measured on the natural logarithm of the permeability) compared to the other (1.0) are compared in Fig. 10. The low variance case had a transmission dispersivity of 5.4 m which is smaller than that of the high variance case (13.5 m) but its echo dispersivity is much lower at 0.27 m (5% of transmission) compared to 1.88 m (14% of transmission).

4.6 Effect of Permeability Anisotropy. For the same correlation structure (20% long range + 80% short range variance), we compare the results of two cases in Fig. 11. One case has no permeability anisotropy ($k_z = k_x$) and the other with a low value of vertical permeability ($k_z = 0.0001 k_x$). Both have similar transmission dispersivities but the echo dispersivity of the case with anisotropy is less than that without anisotropy. Note that we have not changed the values of the input dispersivities with change in anisotropy.

4.7 Effect of Travel Time. All of the simulations presented so far have been for a fixed simulation time (number of days injected). The cases were repeated with shorter injection periods giving results which sample shorter lengths of the model. In Fig. 12, we combine the results of a set of simulations done for the case of long range correlation in the permeability field. The transmission dispersivities from all the cases overlap and are merged. Echo dispersivities increase with penetration distance. Even for the shortest penetration distance (about 10 m) the echo dispersivity (about 0.1 m) is much larger than the input value. The same data for the uncorrelated permeability case is presented

alongside for comparison. The echo dispersivity value at short penetration distance is about the same. The trend of increasing echo dispersivities is seen but here the value at the largest penetration distance is much closer to its corresponding transmission value.

4.8 Comparison with Measured Dispersivities. The simulated dispersivities are compared with the overall trend of field dispersivities in Fig. 14. Both echo and transmission value fall well within the trend. Given only the transmission value and the unknown reservoir description, it would be difficult to infer whether the transport regime was mixing or spreading. Three possibilities arise. First, the transport is in the pre-asymptotic regime and the value of dispersivity has not plateaued. Here the interplay between convection and diffusion has not reached equilibrium. Typical field cases would be in this regime. If the tracer test were run for a longer distance on the same medium then a (different) plateau value might be reached. Second, transport is asymptotic but is locally convective. Here, the dispersivity value is unique but it does not represent mixing or dilution. Third, transport is in asymptotic regime and is well mixed. Here, the dispersivity value is unique and represents large mixing zones.

The ambiguity in interpreting a transmission dispersivity value on the plot is reduced if the corresponding echo dispersivity is known. All echo dispersivities are greater than core scale values implying that mixing is significant at the field scale. The case with longest correlation length has the highest dispersivity value (both echo and transmission). This indicates that convection is enhancing the degree of mixing.

5. Discussion

The most important observation in our work is that significant mixing may occur in field scale displacements even in heterogeneous formations. Field scale miscible displacements need not be entirely in the convective regime as usually assumed. All the echo dispersivities in our simulations are much larger than input values of core- or grid-block-scale mixing and are comparable to field measured values. This corroborates the observations of Mahadevan *et al.* (2003). The key learning is that heterogeneity, while increasing the convective contribution, also increases the amount of mixing in the transverse direction. This effect, while smaller than in the longitudinal direction, is not negligible because it is compounded over the long travel times, resulting in significant dilution of the injected concentration. This suggests that numerical methods based on streamline formulations should be used with caution for miscible transport problems. Moreover, common practice in reservoir simulation uses numerical dispersion as a surrogate for physical dispersion. This can overestimate or underestimate the degree of mixing, depending on how the numerical dispersion compares the physical dispersion occurring in that volume.

Another observation is that dispersion-like behavior can be caused by heterogeneity alone but this does not imply mixing. Other works (e.g. Coats *et al.* (2004)) have made similar observations. This is the effect of the travel time distribution caused by the random geometry of a disordered porous medium in three dimensions. Furthermore, transmission dispersivities are weakly affected by the degree of local mixing. But this does not imply that local mixing can be neglected. If there were no local mixing, then echo dispersivities would be zero. We never observe this because diffusion is always present and for homogeneous isotropic media it gets significantly enhanced. Even with only diffusion as the local mixing mechanism, we observe echo dispersivities

comparable in magnitude to transmission values. Most of the works done on modeling solute transport using stochastic theories are based on the assumption of no local mixing or infinite local Peclet number (Gelhar, 1986, Dagan, 1990, Rubin, 2003). While they might match averaged concentration histories, such theories would not be a good predictor of local concentrations (Kitanidis, 1994; Kapoor and Gelhar, 1994).

Flow reversal provides an unambiguous test to distinguish between spreading and mixing. Another approach to resolve this ambiguity is to measure local concentration histories at multiple points and compare them with the averaged well head concentration history (Cirpka and Kitanidis, 2000a). This approach has been used to interpret an intermediate scale lab experiment based on artificially created heterogeneous media (Jose *et al.*, 2004). Cirpka and Kitanidis (2000b) show an approach to utilize the results of streamtube based tracer transport for the study of mixing-controlled reactive transport.

We have still not directly addressed the practical issue of how to model mixing at the field scale when using an upscaled description. Our results show the need to capture not only the effect of heterogeneity on mixing but also the pre-asymptotic (non-Fickian) transport behavior. Miscible displacements in typical reservoirs are not expected to reach an asymptotic limit that can be described by a unique dispersivity value. Approaches based on continuous time random walks and fractional derivative formulations of the dispersive flux term have been proposed to address this issue (Benson *et al.*, 2000, Berkowitz *et al.*, 2000). Echo dispersivities do indicate the degree of mixing but we do not propose to use them as an input value. So how to best represent the sub grid effects in coarse scale simulation? Of the many approaches have been proposed to this end (Barker and Fayers, 1994; Efendiev *et al.*, 2000; Leonormand, 1996 to name a few), the most promising may be by Berentsten *et al.* (2007). They generalize Taylor's description and derive a one dimensional upscaled model for tracer transport in single phase stratified flow that captures the evolution of the dispersive flux in both early and late time scales.

6. Conclusions

1. Dispersive mixing is significant in field scale miscible displacements even in heterogeneous formations. Permeability layering increases the area available for transverse mixing and this effect gets compounded over large travel times.
2. Flow reversal (echo) tests can be used to distinguish between convective spreading and dispersive mixing. Echo dispersivities estimated from our simulations are comparable in magnitude with the corresponding transmission values. They follow the overall measured trend (Figure 13). This suggests that the large value of dispersivities observed in Figure 1 need not be the result of averaging unknown permeability heterogeneity as commonly understood.
3. Transport in typical reservoirs is usually in the pre-asymptotic regime where Fickian model for dispersion fails to capture the mixing zone growth accurately.
4. Purely convective transport, in certain cases, can also appear to have a dispersion-like behavior. It would be incorrect to model this using a dispersive flux term.

Nomenclature

A	Cross sectional area of the medium, L^2
C	Average concentration, M/L^3
C	Local concentration, M/L^3
D	Dispersion coefficient, L^2/T

D_{mol}	Molecular diffusion coefficient, L^2/T
G	Velocity gradient, $1/T$
h	Lag distance, L
k	Permeability, L^2
L	Length of the medium, L
N_{Pe}	Peclet number
p	Pressure, M/LT^2
q	Average flow rate, L^3/T
r	Semivariogram range, L
s	Semivariogram sill
t	Time, T
u	Flux vector, L/T
V	Average fluid velocity, L/T
x	Distance in x-direction, L
X	Particle position vector, L
Z	Vector of standard normal random numbers

Greek symbols

ϕ	Porosity
Δ	Increment
α	Dispersivity, L
γ	Semi-Variance, L^2
μ	Fluid viscosity, M/LT
μ_x	Mean penetration distance, L
σ	Standard deviation
\square	Local fluid velocity, L/T

Superscripts and Subscripts

D	Dimensionless
l	Longitudinal (to mean flow direction)
o	Cell face
p	Particle
Pe	Peclet Number
t	Transverse (to mean flow direction)
x	X-direction
z	Z-direction

References

- Arbogast, T.,(1998). User's guide to Parssim1: The parallel subsurface simulator, single phase. Center for Subsurface Modeling, Texas Institute for Computational and Applied Mathematics, The University of Texas at Austin: Austin, Texas. p. 84.
- Arbogast, T., *et al.*(1996). Computational methods for multiphase flow and reactive transport problems arising in subsurface contaminant remediation. *Journal of Computational and Applied Math.* 74: p. 19-32.
- Aronofsky, J. S. and J. P. Heller (1957). A diffusion model to explain mixing of flowing miscible fluids in porous media. *Transactions of the American Institute of Mining Engineers* 210: 345-349.
- Arya, A., *et al.* (1988). "Dispersion and reservoir heterogeneity." *SPE Reservoir Engineering* (February): 139-147.
- Barker, J. W. and F. J. Fayers (1994). "Transport coefficients for compositional simulation with coarse grids in heterogeneous media." *SPE Advanced Technology Series* 2(2): 103-112.
- Bear, J. (1961). "Some Experiments in Dispersion. *Journal of Geophysical Research*" 66: 2455.
- Bear, J. and A. Verruijt (1987). *Modeling Groundwater Flow and Pollution*, Springer, New York.
- Benson, D. A., S. W. Wheatcraft, *et al.* (2000). "Application of a fractional advection-dispersion equation." *Water Resources Research* 36(6): 1403-1412.
- Berentsen, C. W. J., C. van Kruijsdijk and M. L. Verlaan. (2007). "Upscaling, relaxation and reversibility of dispersive flow in stratified porous media." *Transport in Porous Media* 68(2): 187-218.
- Berkowitz, B. *et al.* (2000). "Anomalous transport in laboratory-scale, heterogeneous porous media." *Water Resources Research* 36(1): 149-158.

- Chrysikopoulos, C. V., P. V. Roberts and P. K. Kitanidis (1990). "One-Dimensional Solute Transport in Porous Media With Partial Well-to-Well Recirculation: Application to Field Experiments." *Water Resources Research* 26(6): 1189-1195.
- Cirpka, O. A. and P. K. Kitanidis (2000a). "Characterization of mixing and dilution in heterogeneous aquifers by means of local temporal moments." *Water Resources Research* 36(5): 1221-1236.
- Cirpka, O. A. and P. K. Kitanidis (2000b). "An advective-dispersive stream tube approach for the transfer of conservative-tracer data to reactive transport." *Water Resources Research* 36(5): 1209-1220.
- Coats, K.H., C.H. Whitson, and L.K. Thomas (2004). "Modeling conformance as dispersion." presented at the 2004 SPE Annual Technical Conference and Exhibition, Sep 26-29, Houston, TX, United States.
- Cox, R. G. and S. G. Mason (1971). "Suspended Particles in Fluid Flow Through Tubes." *Annual Review of Fluid Mechanics* 3(1): 291-316.
- Dagan, G. (1990). "Transport in heterogeneous porous formations: spatial moments, ergodicity, and effective dispersion." *Water Resources Research* 26(6).
- Delshad, M. and G.A. Pope (2003). "Effect of dispersion on transport and precipitation of barium and sulfate in oil reservoirs." presented at the SPE International Symposium on Oilfield Chemistry. 5-7 February 2003, Houston, Texas.
- Efendiev, Y., L. J. Durlofsky and S. H. Lee (2000). "Modeling of subgrid effects in coarse-scale simulations of transport in heterogeneous porous media." *Water Resources Research* 36(8): 2031-2041.
- Flekkoy, E. G. (1997). "Symmetry and reversibility in mixing fluids." *Physics of Fluids* 9(12): 3595-3599.
- Flekkoy, E. G., T. Rage, *et al.* (1996). "Hydrodynamic irreversibility in creeping flow." *Physical Review Letters* 77(20): 4170-4173.
- Gelhar, L. W. (1986). "Stochastic subsurface hydrology from theory to applications." *Water Resources Research* 22(9): 1358-1458.
- Gelhar, L. W. *et al.* (1992). "A critical review of data on field-scale dispersion in aquifers." *Water Resources Research* 28(7): 1955-74.
- Haajizadeh, M., *et al.* (1999). "On the Importance of Dispersion and Heterogeneity in the Compositional Simulation of Miscible Gas Processes." presented at the SPE Asia Pacific Improved Oil Recovery Conference. 1999. Kuala Lumpur, Malaysia.
- Heller, J. P. (1960). "An Unmixing Demonstration." *American Journal of Physics* 28: 348.
- Heller, J. P. (1972). "Observations of mixing and diffusion in porous media." in the proceedings of the 2nd International Symposium on Fundamentals of Transport Phenomena in Porous Media, Guelph University, Ontario, Canada. vol. 1:1-26.
- Hiby, J. W. (1962). "Longitudinal and transverse mixing during single-phase flow through granular beds." in the Proceedings of the Symposium on the Interaction Between Fluids and Particles, London, Institution of Chemical Engineers.
- Hulin, J. P. and T. J. Plona (1989). "Echo tracer dispersion in porous media." *Physics of Fluids A: Fluid Dynamics* 1(8): 1341-7.
- Jennings, J.W., S.C. Ruppel, and W.B. Ward (2000). "Geostatistical analysis of permeability data and modeling of fluid-flow effects in carbonate outcrops." *SPE Reservoir Evaluation and Engineering*, 2000. 3(4): p. 292-303.
- Jessen, K., E.H. Stenby, and F.M. Orr Jr. (2002). "Interplay of Phase Behavior and Numerical Dispersion in Finite Difference Compositional Simulation." presented at the SPE/DOE Thirteenth Symposium on Improved Oil Recovery, Apr 13-17 Tulsa, OK, United States.
- John, Abraham K.: *Dispersion in Large Scale Permeable Media*. Ph.D. dissertation. The University of Texas, Austin. (In progress).
- Jose, S. C., M. A. Rahman and O. A. Cirpka (2004). "Large-scale sandbox experiment on longitudinal effective dispersion in heterogeneous porous media." *Water Resources Research* 40(12): W12415.
- Kapoor, V. and L.W. Gelhar (1994). "Transport in three-dimensionally heterogeneous aquifers 1. Dynamics of concentration fluctuations." *Water Resources Research*, 1994. 30(6): p. 1775-1788.
- Kitanidis, P.K. (1994). "The concept of the dilution index." *Water Resources Research*. 30(7): p. 2011-2026.
- LaBolle, E.M., G.E. Fogg, and A.F.B. Tompson (1996). "Random-walk simulation of transport in heterogeneous porous media: Local mass-conservation problem and implementation methods." *Water Resources Research* 32(3): p. 583-594.
- Lake, L.W. (1989). *Enhanced Oil Recovery*. Prentice Hall, New Jersey.
- Lake, L.W. and G.J. Hirasaki (1981). "Taylor's dispersion in stratified porous media." *SPE Journal*, 21(4): p. 459-468.
- Lenormand, R. and B. Wang (1995). "A stream tube model for miscible flow." *Transport in Porous Media* 18(3): 263-282.
- Mahadevan, J., Lake, L. W. and R. T. Johns (2003). "Estimation of true dispersivity in field-scale permeable media." *SPE Journal* 8(3): p. 272-279.
- Moulds, T.P., *et al.* (2005). "Pt. McIntyre: A case study of gas enrichment above MME." *SPE Reservoir Evaluation and Engineering* 8(3): p. 182-188.
- Oldenburg, C.M., K. Pruess, and S.M. Benson (2001). "Process modeling of CO₂ injection into natural gas reservoirs for carbon sequestration and enhanced gas recovery" *Energy and Fuels* 15, 293-298,

- Perkins, T. K. and O. C. Johnston (1963). "A review of diffusion and dispersion in porous media." SPE Journal 3(3): 70-84.
- Pollock, D. W. (1988). "Semianalytical computation of path lines for finite-difference models." Ground Water 26(6): 743-750.
- Press, W. H., et al. (1992). *Numerical recipes in C: the art of scientific computing*. Cambridge University Press, New York.
- Rigord, P., A. Calvo and J. P. Hulin (1990). "Transition to irreversibility for the dispersion of a tracer in porous media." Physics of Fluids A: Fluid Dynamics 2(5): 681-7.
- Risken, H. (1996). *The Fokker-Planck Equation: Methods of Solution and Applications*. Springer, New York.
- Romeu, R.K. and B. Noetinger (1995). "Calculation of internodal transmissivities in finite difference models of flow in heterogeneous porous media." Water Resources Research 31(4): p. 943-960.
- Rubin, Y. (2003). *Applied Stochastic Hydrogeology*. Oxford University Press, New York.
- Schulze-Makuch, D. (2005). "Longitudinal dispersivity data and implications for scaling behavior." Ground Water 43(3): 443-456.
- Solano, R., R.T. Johns, and L.W. Lake (2001). "Impact of reservoir mixing on recovery in enriched gas drives above the minimum miscibility enrichment." SPE Reservoir Evaluation and Engineering 4(5): p. 358-365.
- Sorbie, K.S. and E.J. Mackay (2000). "Mixing of injected, connate and aquifer brines in waterflooding and its relevance to oilfield scaling." Journal of Petroleum Science and Engineering, 27(1): p. 85-106.
- Taylor, G. I. (1953). "Dispersion of soluble matter in solvent flowing slowly through a tube." Proceeding of the Royal Society (London) A219: 186-203.
- Taylor, G. I. (1972). *Low Reynolds Number Flows*. The National Committee for Fluid Mechanics Films. Chicago, IL, Encyclopedia Britannica Educational Corporation. See also : <http://web.mit.edu/fluids/www/Shapiro/ncfmf.html>
- Tchelepi, H. A. (1994). *Viscous fingering, gravity segregation and permeability heterogeneity in two-dimensional and three dimensional flows*. PhD Dissertation, Department of Petroleum Engineering, Stanford University.
- Tidwell, V. C. and J. L. Wilson (2000). "Heterogeneity, permeability patterns, and permeability upscaling: Physical characterization of a block of Massillon sandstone exhibiting nested scales of heterogeneity." SPE Reservoir Evaluation and Engineering.
- Tompson, A. F. B. and L. W. Gelhar (1990). "Numerical simulation of solute transport in three-dimensional, randomly heterogeneous porous media." Water Resources Research 26(10): 2541-2562.
- Uffink, G. J. M. (1990). *Analysis of dispersion by the random walk method*. PhD Dissertation, Delft Technical University.
- Verlaan, M.L., et al. (1998). "Effect of shales on mixing in underground gas storage." in Proceedings of the 1998 SPE Gas Technology Symposium, Mar 15-18. Calgary, Can: Soc Pet Eng (SPE), Richardson, TX, USA.
- Willis, B. J. and C. D. White (2000). "Quantitative Outcrop Data for Flow Simulation." Journal of Sedimentary Research 70(4): 788-802.

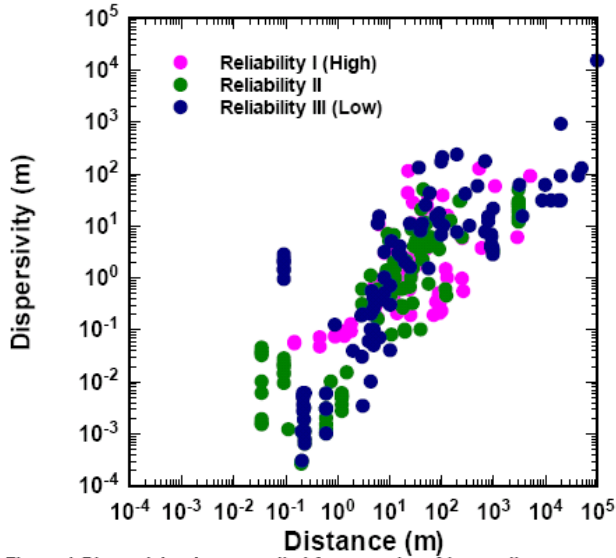


Figure 1 Dispersivity data compiled from results of interwell tracer tests done over several formation types and a range of length scales (Schulze-Makuch, 2005 and references therein). The reliability classification is from Gelhar *et al.* (1992). Dispersivities increase with distance and reach values about four factors of ten larger than lab measured ones. The effect of heterogeneity (layering) in such large values is unknown. The trend at large distances suggests a leveling off.

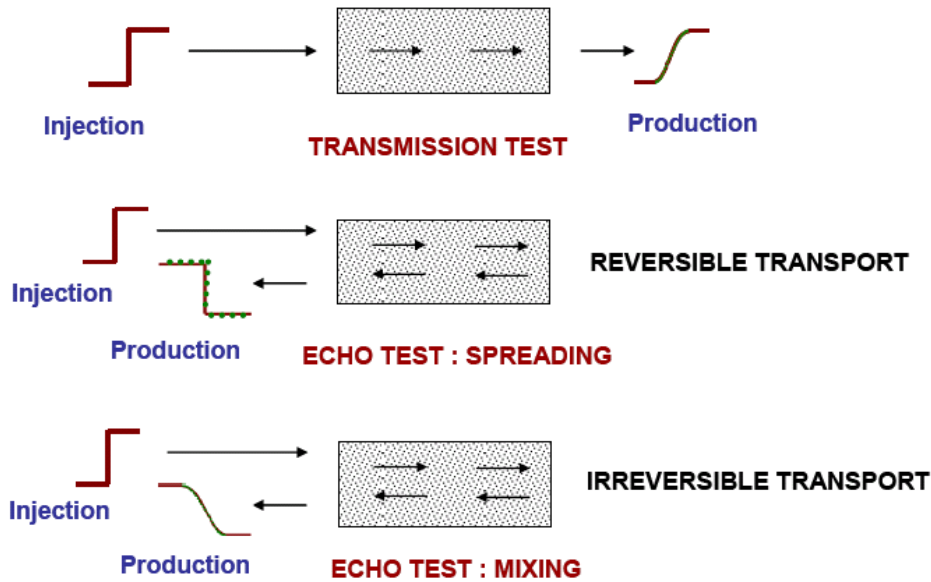


Figure 2 Sketch showing the use of flow reversal to distinguish between spreading (convective transport) and mixing (dispersive transport). If the flow is laminar and slow (low Reynolds number) then ideal reversibility in flow field can be assumed, in absence of diffusion, the tracer concentration history on flow reversal will be same as that originally injected.

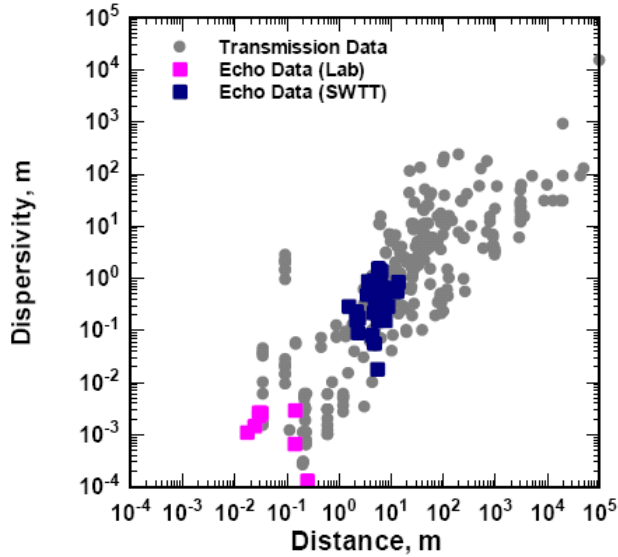


Figure 3 Comparison of field measured dispersivities with echo dispersivity data estimated from lab tests (Hulin and Plona, 1989; Rigord *et al.*, 1990) and those history matched from single well tracer tests (Mahadevan *et al.*, 2003). Echo dispersivities fall on the overall trend and the ones at the field scale (>100m) are much larger than lab scale values suggesting the possibility of significant mixing in field scale displacements.

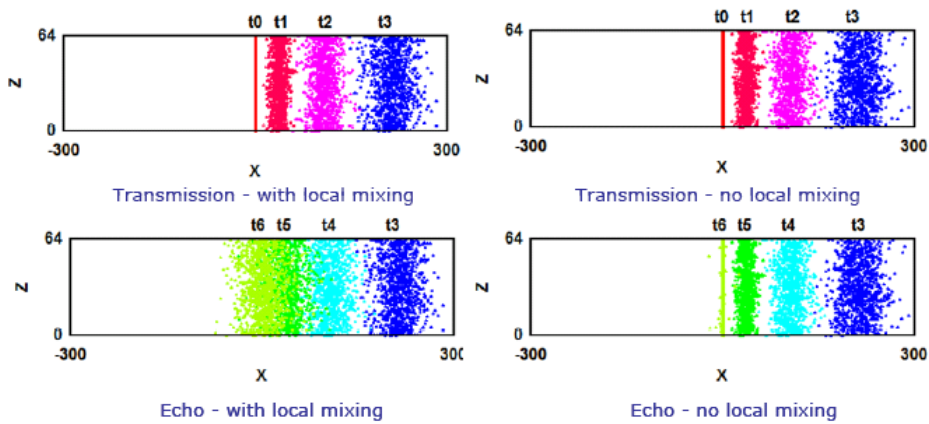


Figure 4 Example of particle tracking calculations. The figures in the top row show the progression of the ensemble of particles for the uncorrelated permeability case during forward flow (transmission) at successive times (t_0 is the initial condition). The figures in the bottom row show the particle positions during flow reversal (echo) with increasing time. In the left column, local mixing is included ($D_{mol} = 1.0 \times 10^{-4} \text{ m}^2/\text{d}$, $\alpha_l = 0.01 \text{ m}$ and $\alpha_g = 0.001 \text{ m}$ within each grid cell) and on the right there is no local mixing ($D_{mol} = 0$, $\alpha_l = 0$, and $\alpha_g = 0$). With no local mixing, particles return to their initial positions (compare t_6 and t_0). The transmission profiles (top row) are quite similar whereas the echo profiles (bottom row) are different.

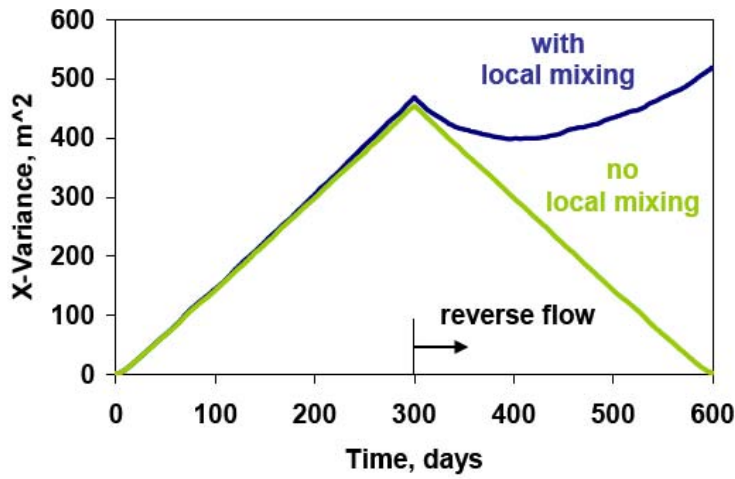


Figure 5 Evolution of the variance of the particle x-positions (taken over an ensemble of 10,000 particles) with travel time for the uncorrelated permeability case. During forward flow period (upto 300 days), the variance increases almost linearly with time. After flow reversal, for the case with no local mixing ($D_{mol} = 0$, $\alpha_i = \alpha_i = 0$), the particles retrace their paths and the variance returns to zero. With local mixing, there is a short period of convective reversal after which the particle cloud grows again.

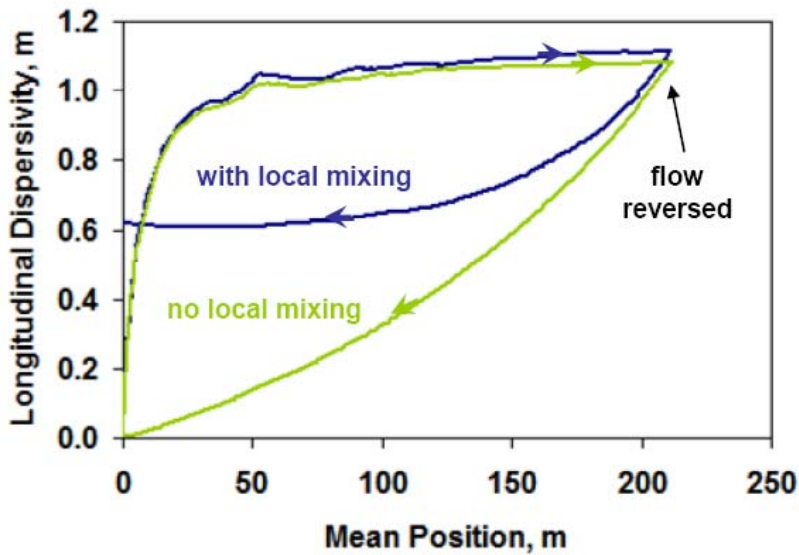


Figure 6 Evolution of the longitudinal dispersivity with distance traveled for the uncorrelated permeability case. This is computed from the statistics of the particle ensemble. The mean velocity is about 0.75 m/d. The dispersivity estimated in the forward flow (transmission) case is almost the same with and without local mixing (0.01 m). On flow reversal, the echo dispersivity for the case with local mixing is about 0.6 m which is much larger than the input value (0.01 m).

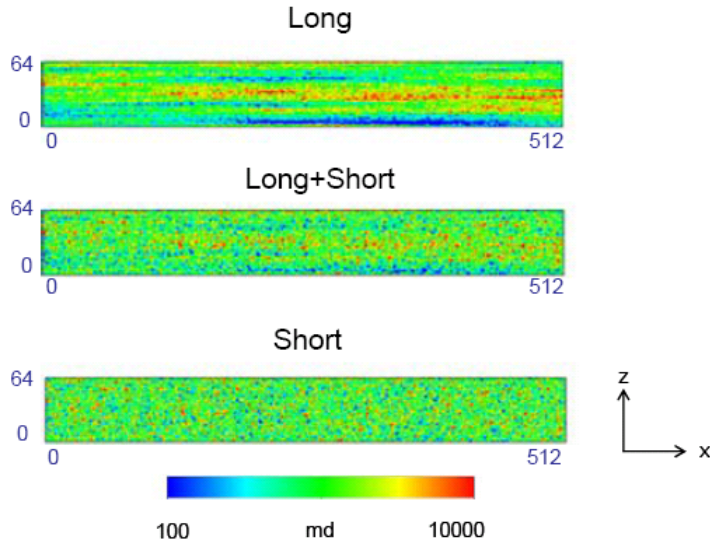


Figure 7 Cross sections of a single realization of the permeability field showing the effect of changing correlation structure. As the proportion of the long range component is increased, the amount of layering is more pronounced. The short scale structure has a range of 1 m in all directions. The long range structure has a range of 250 m in the x-direction and 5 m in y and z directions. The contribution of the short scale structure to the overall variance is 100 %, 80% and 20% from bottom to top. The figures are plotted with no vertical exaggeration. The actual reservoir dimensions used in the flow field simulation is 2048 m x 64 m x 64 m. Size of each grid cell is 1 m x 1 m x 1 m.

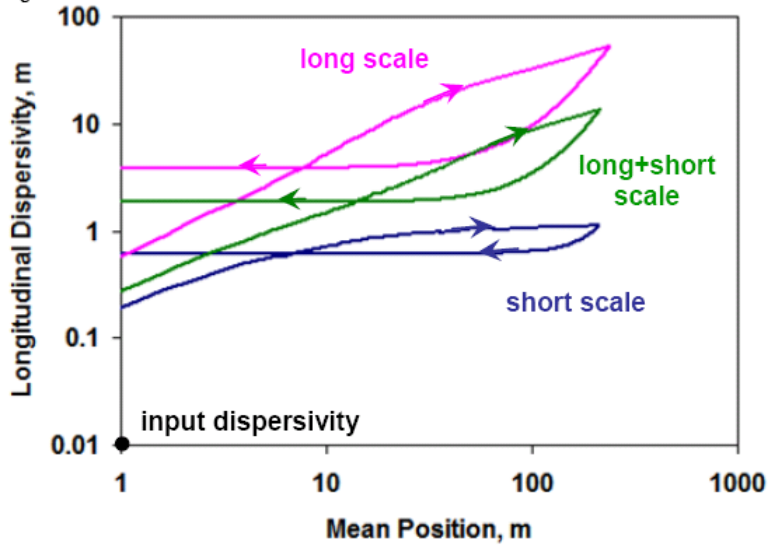


Figure 8 Evolution of the longitudinal dispersivity for cases with changing correlation structure (Figure 7). Layering significantly increases the transmission dispersivity and enhances the mixing as seen by the increase in echo dispersivities. The dispersivities on flow reversal are much larger than the input value ($D_{me} = 1.0 \times 10^{-4} \text{ m}^2/\text{d}$, $\alpha_l = 0.01 \text{ m}$ and $\alpha_c = 0.001 \text{ m}$).

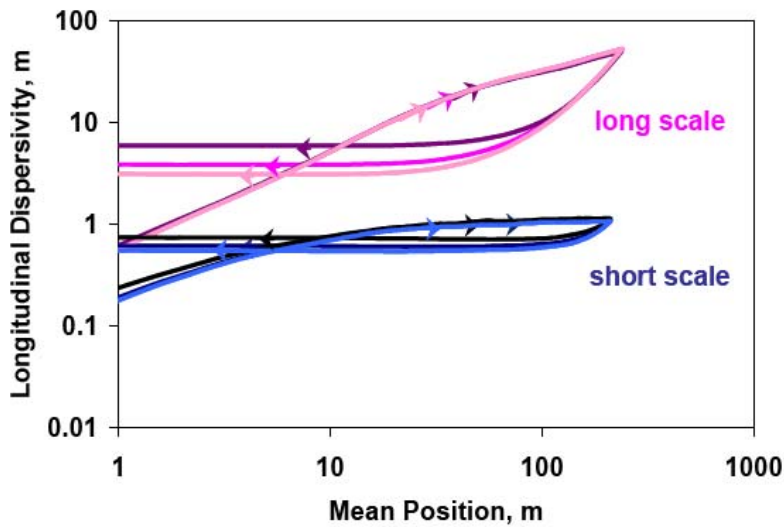


Figure 9. Comparison of the effect of local mixing on longitudinal dispersion for two cases - uncorrelated permeability (lower set of curves in shades of blue) and long range correlation (upper set of curves in shades of pink). The three results around each case corresponding to increasing levels of local mixing : only diffusion ($D_{mol}=1.0\times 10^{-4} \text{ m}^2/\text{d}$), diffusion+dispersion ($D_{mol}=1.0\times 10^{-4} \text{ m}^2/\text{d}$, $\alpha_L = 0.01 \text{ m}$, $\alpha_T = 0.001 \text{ m}$), diffusion+dispersion ($D_{mol}=1.0\times 10^{-4} \text{ m}^2/\text{d}$, $\alpha_L = 0.05 \text{ m}$ and $\alpha_T = 0.005 \text{ m}$). There is almost no change in transmission dispersivities and little change in echo values. If diffusion were absent, all echo dispersivities would return to zero as in Figure 6.

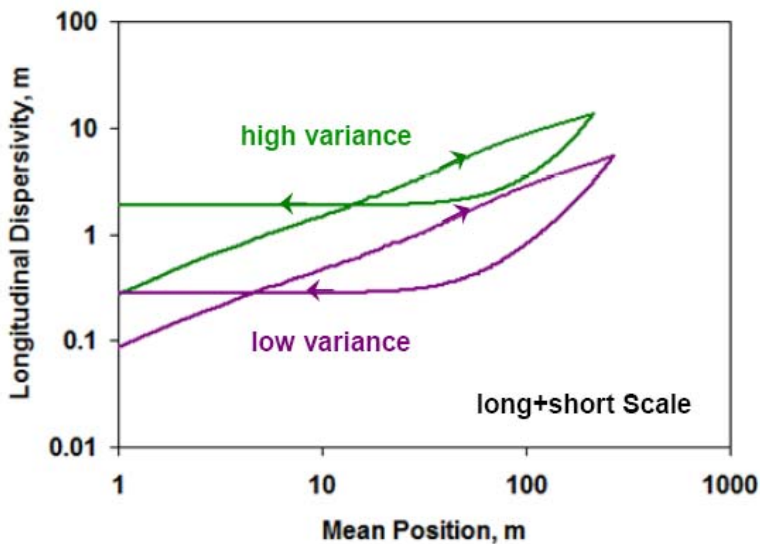


Figure 10 Comparison of dispersivities with change in permeability heterogeneity. The low variance case had a transmission dispersivity lower than that of the high variance case but its echo dispersivity is much lower (5% of transmission) compared to that of the high variance case (14% of transmission).

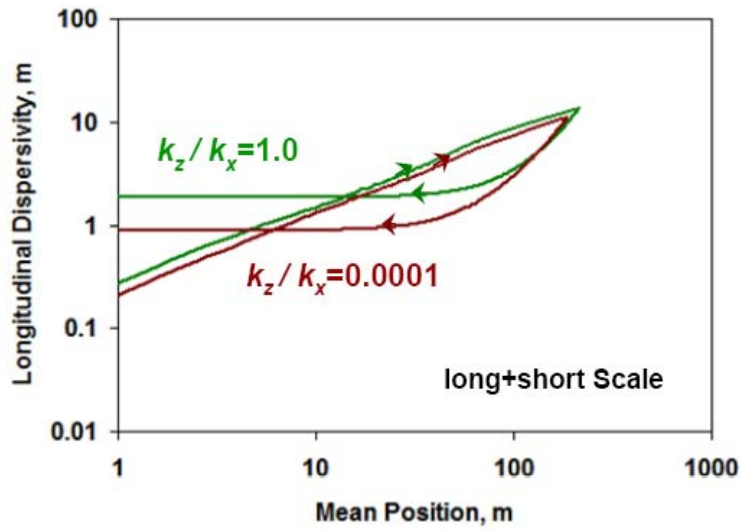


Figure 11. Comparison of dispersivities with change in permeability anisotropy (lowered from 1 to 0.0001). Both have identical transmission dispersivities but the echo dispersivity of the case with anisotropy is slightly smaller than that without anisotropy.

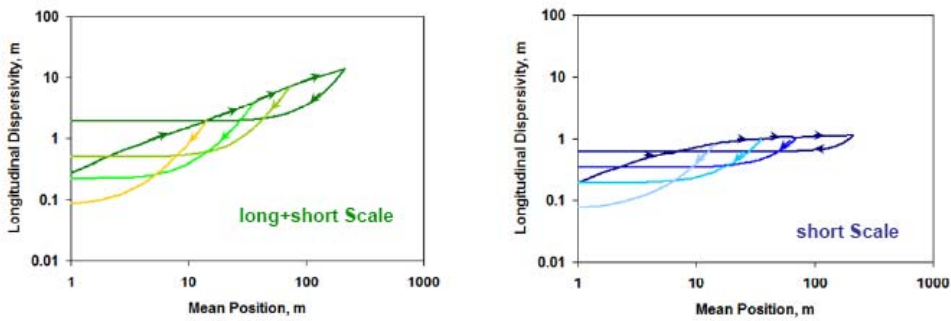


Figure 12 Comparison of dispersivities for change in travel time (penetration distance). Even for the shortest penetration distance (about 10 m) an echo dispersivity value (about 0.1 m) much larger than the input value is obtained. The same data for the uncorrelated field is presented on the right for comparison. In both cases, echo dispersivities increase with penetration distance.

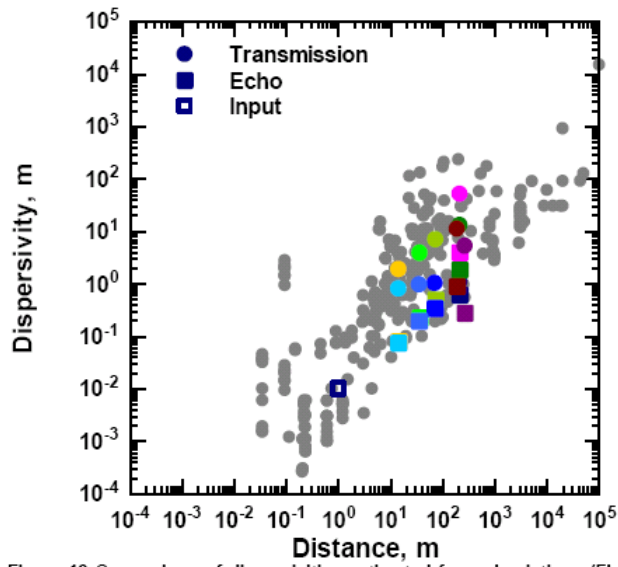


Figure 13 Comparison of dispersivities estimated from simulations (Figures 8-12) with the field measured values. Both echo and transmission values fall within the measured trend. The ambiguity in interpreting a transmission dispersivity value on the plot, is now reduced by having the corresponding echo dispersivity. The simulation results also help explain the large values of echo data estimated from single well tracer tests (Figure 3).

Topic 3b: Grain-scale analysis of flow reversal

Summary

Flow reversal studies provide insights about mixing mechanisms in flow through porous media. In these studies the direction of flow is reversed after the solute slug has penetrated into the medium (but not exited) to a pre determined distance. We simulated the effect of flow reversal on mixing in two-dimensional porous media using two different approaches. In the first approach, we perform direct numerical simulation of a solute slug transport (by solving Navier Stokes and convection diffusion equations) in a surrogate pore space. This approach allows a direct visualization of mixing occurring because of interaction between convective spreading and diffusion in simple flow geometries. The effect of flow reversal on mixing is investigated for several diffusion coefficients, penetration depths and flow geometries. The second approach uses particle tracking to simulate the effect of flow reversal at larger length scales. This approach is free of numerical dispersion, can be used in the absence of diffusion and has no limits on the size of the simulation. It is, however, limited to layered media flow.

The simulation studies presented in this paper explain the mechanism of mixing and the origin of the irreversibility of dispersion in flow through porous media. We also explain several experimental observations on flow reversal tests found in the literature.

Mixing in porous media takes place because of interaction between convective spreading and molecular diffusion. The converging-diverging paths and flow around impervious sand grains causes the solute front to stretch and split. In this process the area of contact between the solute slug and the resident fluid increases by an order of magnitude and diffusion becomes an effective mixing mechanism. This local mixing, caused by diffusion, is irreversible.

For purely convective transport, upon flow reversal solute particles retrace their path back to the inlet. Convective spreading gets cancelled and echo dispersion is zero. Diffusion even though small in magnitude, is responsible for local mixing and making dispersion in porous media irreversible. Thus it is important to include the effect of diffusion when analyzing miscible displacements in porous media.

Introduction

A solvent slug injected for a miscible enhanced oil recovery process mixes with the reservoir fluid at its leading edge and with the chase fluid at its trailing edge. This mixing dilutes the slug and reduces its displacement efficiency. Predicted oil recovery in such processes may differ by up to 15% of initial oil in place depending on the amount of mixing taking place in the medium (Johns et al., 2002). Therefore, understanding and quantifying mixing is important for determining the effectiveness of miscible floods.

Traditionally, mixing in flow through a porous medium is quantified by carrying out *transmission dispersion* experiments in which one miscible fluid displaces another entirely through a core sample. The flow averaged effluent concentration history is analyzed using a solution to the one-dimensional convection-diffusion equation to obtain the *dispersion coefficient* which is used to quantify mixing in flow through the medium (Lake, 1989; Bear, 1972).

The dispersion coefficient describes *apparent mixing* because it is averaged over the entire outlet and includes contributions (in inseparable form) from (i) *convective*

spreading, caused by variations in path lengths and velocities of solute particles traveling along different streamlines and (ii) *molecular diffusion*.

Transmission measurements do not give any information about the nature and origin of dispersion in flow through porous media. For example, we consider two different hypotheses for solute transport and mixing in homogeneous porous media which could explain the observed dispersion.

1. Convective Spreading Hypothesis: A solute particle travelling on a given streamline stays on that streamline until the exit (Fig. 1(a)). It has no interaction with the particles on adjacent streamlines. In this case dispersion is a result of convective spreading only (Coats et al., 2004). Diffusion being much smaller in magnitude can be neglected.

2. Local Mixing Hypothesis: Solute particles can jump to adjacent streamlines because of diffusion. Diffusion redistributes particles within the medium (Fig. 1(b)). In this case dispersion is a result of interplay between convective spreading and diffusion. Diffusion, being small in magnitude as compared to convective spreading has negligible effect on overall spreading of the solute slug.

Both hypotheses predict normally distributed solute concentration profiles and histories and explain experimentally observed dispersion behavior but they have an important fundamental difference. In the first hypothesis solute particles are just getting spread, not getting mixed. Spreading is the change of shape of the slug as it gets distorted in a medium consisting of high and low velocity regions. The solute concentration anywhere within the slug is not reduced (Kitanidis, 1994). Only when a cup-mixing average is taken the concentration appears to be reduced. On the other hand, in the second hypothesis the solute slug is undergoing local (in-situ) mixing and getting diluted. Local mixing is the true mixing and causes a reduction in solute concentration at a point scale.

Dispersion coefficient obtained from an averaged transmission effluent concentration history cannot distinguish between spreading and local mixing. Therefore, flow reversal studies are carried out where the direction of flow is reversed after the solute slug has penetrated into the medium (but not exited) to a pre determined distance. Backward effluent concentration history obtained at the outlet (original inlet) is analyzed to obtain *echo dispersion coefficient*. Echo dispersion coefficient can determine relative significances of convective spreading and local mixing in the dispersion process and provide insights about its nature.

Convective spreading hypothesis implies that on flow reversal the solute particles would retrace their paths and the injected slug will be received back at the inlet without any dissipation. The convective spreading of solute particles would thus be *reversible* and echo dispersion will be zero. Reversibility has been demonstrated for slow, laminar flows between disordered arrays of cylinders (Hiby, 1962) and flow between concentric cylinders (Taylor, 1972).

However, echo dispersion experiments on homogeneous core samples show dispersion to be *irreversible* (Hulin and Plona, 1989). The solute slug continues to disperse (and mix) as it moves back towards the original inlet. Dispersivities obtained from such flow reversal experiments on homogeneous core samples in the lab (Hulin and Plona, 1989; Rigord et al., 1990) and from single well tracer tests in field (Mahadevan et al., 2003) are as large as the corresponding transmission values. On the other hand, echo

dispersion experiments on layered media show largely reversible dispersion (Hulin and Plona, 1989; Rigord et al., 1990a; Rigord 1990b). Thus comparing the transmission and echo dispersivities gives information about heterogeneities of the medium and helps ascertain the nature of the dispersion mechanism. The irreversibility of dispersion (in homogeneous media) is contrary to the convective spreading hypothesis and indicates that there is local mixing taking place. The fraction of irreversibility of dispersion depends on the degree of local mixing taking place.

We studied impact of flow reversal on dispersion and mixing using two different numerical methods. In the first method, we carried out pore-scale simulations for miscible flow in several two-dimensional (2D) flow geometries. We used a multi-physics modelling software FEMLAB (2004) (now COMSOL) to solve the Navier-Stokes and convection diffusion equations directly for the given flow geometry. This approach allows investigation of solute transport and mixing from first principles without making assumptions about macroscopic dispersive models for mixing (Jha et al., 2006). We can directly visualize mixing in the medium because of interaction between convective spreading and diffusion. We also compute forward (transmission) and backward (echo) effluent concentration histories for comparison with the experimental observations. We carried out pore-scale simulations in several simple flow geometries to understand the mechanisms of local mixing and the factors influencing it. Then we use the insights gained to investigate effect of flow reversal on dispersion in more realistic models of porous media.

The second approach uses particle tracking to simulate solute transport at larger length scales. This approach is free of numerical dispersion, can be used in the absence of diffusion and has no limits on the size of the simulation field. We show results for the limiting case of flow through layered media. We explain the mixing mechanism and the reason for irreversibility of dispersion in porous media.

Mixing Mechanism and Effect of Flow Reversal on Mixing

We have carried out direct numerical simulation using FEMLAB in two-dimensional porous media consisting of a rectangular plate with circular holes in it (Jha et al., 2006). The holes represent the sand grains and the fluid can flow through the pore space between them. The size of the flow domain is 1800×800 micro meters. The grain diameter is taken as 100 micro meters. In each case, a solute slug is injected into the medium at a small velocity of 10^{-5} m/s for 20 seconds (which corresponds to 0.1 PV, approximately). The outlet face of the medium is maintained at atmospheric pressure. All other boundaries including the sand grain boundaries are of “no-slip” kind. The steady state velocity at each point inside the medium is obtained by solving the Navier-Stokes equation. The Reynolds number is very low in these simulations ($Re \approx 10^{-3}$) and inertial effects may be neglected. The solute concentration as a function of time and space is then determined by solving the two-dimensional convection-diffusion equation. This equation uses the computed velocities at each point and an input diffusion coefficient, $D_o = 10^{-11}$ m^2/s . When the slug reaches the center of the medium the direction of flow is reversed. Visualization of mixing occurring because of interaction between convective spreading and diffusion illustrates the mixing mechanism. Deviation of backward (or echo) effluent

concentration history from input concentration history also indicates the degree of irreversibility of dispersion which in turn indicates relative significance of local mixing in dispersion. We first present simulation results for simple flow geometries.

(i) Plug Flow in a Channel (Fig. 2) - In this case, the fluid velocity is uniform throughout the cross-sectional area of the medium. There is no local velocity gradient and convection plays no role in dispersion. Dispersion is caused solely by diffusion. Mixing and dispersion are the same in this case. Upon flow reversal, the slug encounters exactly the same conditions and behaves exactly same way that it would have done had it continued to move forward. Therefore, flow reversal has no effect on dispersion and dispersion is completely irreversible. Local mixing, as evidenced by concentration transition zones at the front and back of the slug, is small.

(ii) Parabolic Velocity Profile in a Channel (Fig. 3) - In this case the fluid velocity is a maximum at the center of the medium and zero at the walls. Because of velocity gradients the solute-front stretches and the contact area between regions of large and small solute concentrations increases (Taylor, 1953; Aris, 1959). Therefore, more local mixing takes place compared to case (i). However, convective spreading is much larger than local mixing. Upon flow reversal, the convective spreading cancels and dispersion is largely reversible (except for small local mixing).

(iii) Flow around a Grain (Fig. 4) - Here the solute slug encounters an obstruction in form of a sand grain. The grain being impervious and having no-slip boundaries, the solute front splits around the sand grain and then rejoins. Because the splitting increases the interface between large and small solute concentrations, mixing by diffusion is enhanced. Upon flow reversal, even though convective spreading vanishes, the local mixing is large as compared to that in Figures 2 and 3. Dispersion is not as reversible as in case (ii).

Experiments and simulations in a similar flow geometry show that the tracer transport is only partially reversible even with a very small diffusion coefficient (Flekkoy et al. 1995; Muzzio et al., 1992). However, this irreversibility is insignificant for the low Reynolds number ($Re \approx 10^{-3}$) in our simulations and not considered.

(iv) Flow around Three Grains (Fig. 5) - More grains cause more stretching, splitting and rejoining of the solute slug. This results in enhanced local mixing (Muzzio et al., 1992). Greater local mixing yields greater irreversibility of dispersion.

Discussion on Local Mixing Mechanism

A comparison of the backward (or echo) effluent concentration histories at the original inlet (which becomes the outlet during backward flow) for all the previous cases is shown in Figure 6 for $D_o = 10^{-11} \text{ m}^2/\text{s}$. These histories are velocity weighted averaged solute concentrations at the outlet face. The input concentration and slug size is same in all the cases. If dispersion were completely reversible, the effluent concentration history in each case would be the same, which in turn would be same as the input concentration history. The deviation of the effluent history from the input history indicates the degree of irreversibility of dispersion resulting from local mixing. In the examples presented

here, a longer contact area between large and small solute concentrations allows more local mixing to occur during same interval of time. The greater the local mixing, the greater is the extent of irreversibility.

The magnitude of diffusion affects local mixing significantly. Figure 7 compares the backward effluent concentration histories for the same cases for a smaller diffusion coefficient $D_o = 10^{-12} \text{ m}^2/\text{s}$. Reducing the diffusion coefficient has reduced the local mixing and all the curves shift towards the input concentration. In the limit of zero diffusion all the effluent concentration histories will coincide with the input concentration. On the other hand, if we increase the diffusion coefficient to $10^{-10} \text{ m}^2/\text{s}$, more local mixing will result (Fig. 8). Dispersion is irreversible in all the cases and all of the curves are nearly the same.

It is to be noted that we have made an assumption that upon flow reversal the solute slug attains steady state velocity immediately in the backward direction. It is a reasonable assumption for the slow velocity in our simulations. In reality, because of slower velocity during transient state there will be more time for diffusion to cause mixing. Therefore, by making assumption of instantaneous achievement of steady state we under-predict mixing slightly. Since our conclusions are qualitative in nature and not quantitative, we neglect this effect.

Flow Reversibility Simulations in a Disordered Pack

We test the insights gained from simulations in simple geometries by conducting flow reversal studies in a disordered arrangement of disks. Even though this model of a porous medium is two dimensional and has an unrealistically large porosity, it does capture the basic physics of the process and allows qualitative comparisons with experimental observations.

The dimensions of the flow domain and flow conditions are same as described for previous cases. The only difference is that now the medium has many disks representing sand grains and the diameter of the disks are half of that used previously.

The velocity inside the medium varies widely both in longitudinal and lateral directions. Therefore, the solute slug does not move uniformly throughout the cross-section of the medium. It spreads more in the regions of high velocity (Fig. 9 (a), (b)). The differential movement of different parts of the solute slug across the cross section grows with time and distance traveled. If the slug keeps on moving in the forward direction and effluent concentration is monitored at the outlet, it would not satisfy the 1D convection-diffusion equation (in other words, concentration history curve is non-Gaussian). However, if the flow direction is reversed and effluent concentration history is monitored at the original inlet, the backward or echo dispersion curve becomes Gaussian because the convective spreading gets cancelled upon flow reversal (Flekkoy et al., 1996) (Fig. 10). Cancellation of convective spreading is also evident if we compare solute concentration profiles at the same distance from the inlet in forward and backward flow (Figs. 9 (a) and (c)). The two profiles look similar in shape. However, the backward profile is more dispersed because of irreversible local mixing.

If the diffusion coefficient is increased, the solute spreads more in the lateral direction and greater local mixing takes place. The effect of heterogeneity on dispersion is reduced (Jha et al., 2006), the degree of irreversibility of dispersion increases and forward and backward concentration histories become similar (Fig. 11).

Figure 12 shows the effect of penetration depth on local mixing. In these simulations, solute is injected continuously into the medium and flow is reversed from different penetration depths of the solute front. The comparison of backward dispersion curves (evaluated at original inlet) along with transmission dispersion curve (evaluated at original outlet) is shown in Figure 12. The transmission curve is non-Gaussian and all the backward-dispersion curves are Gaussian. Greater penetration depth corresponds to greater time spent by the solute front inside the medium and hence increased local mixing. Therefore, we can see greater irreversibility of dispersion for greater penetration depth. Moreover, the flow reversal eliminates the non-Gaussian manifestation of the heterogeneous flow field.

All of these runs indicate that local mixing depends on diffusion coefficient, area available for diffusion between regions of large and small solute concentration throughout the process and time spent by the slug inside the medium.

Flow Reversibility Simulations in an Ordered Pack

Flow reversal simulations were also carried out for a regular arrangement of disks. In this case the local velocity does not vary widely from point to point and even small diffusion is able to eliminate radial concentration discontinuities in a pore (Jha et al., 2006). The solute slug appears to move like a plug. The effect of convection, splitting and rejoining around sand grains is to enhance the effective diffusion coefficient and mixing during flow is “diffusion-like”. It is analogous to case (i) (plug flow) but with a larger dispersion (effective diffusion) coefficient. Upon flow reversal, the slug behaves exactly same way while flowing backward that it would have done while flowing forward. Therefore flow reversal has no effect on dispersion and dispersion is completely irreversible (Hulin and Plona, 1989; Rigord et al., 1990) (Figs. 13, 14).

For zero diffusion, we would expect no local mixing (except for that arising from the numerical dispersion) and hence dispersion would be reversible. Simulations for small diffusion-coefficient tend to be numerical unstable. Since increasing the velocity has the same effect on local mixing as reducing the diffusion coefficient (Jha et al., 2006), we simulated the process for a diffusion coefficient 20 times smaller and twice the velocity (it has same effect on local mixing as reducing diffusion coefficient by a factor of forty). The results show partial reversibility of dispersion for this increased Peclet number (Fig. 15). If there is no diffusion at all the solute particles will move along individual streamlines. Upon flow reversal they would retrace their path to origin and dispersion will be reversible.

Flow Reversibility Simulations in Layered Flow

Memory limitations constrain the size of the porous medium in which we can explicitly represent the location of grains. To extend the above insights we simulate transport in a layered flow field using a particle tracking approach. The details of the particle tracking algorithm are as follows.

Particle tracking algorithm

The particle tracking procedure uses a given velocity field and molecular diffusion to compute the positions of point-like tracer particle released at the origin. The

velocities are parallel to the flow domain (y component is zero) and are constant along the entire length. The net displacement of a particle is the sum of the convective and diffusive displacements.

$$x_{n+1} - x_n = u_n \Delta t + \Delta r \cos \varphi_n \quad (\text{A.1})$$

$$y_{n+1} - y_n = \Delta r \sin \varphi_n \quad (\text{A.2})$$

$$\Delta r = \sqrt{2D_o \Delta t} \quad (\text{A.3})$$

where u is the velocity at point (x_n, y_n) and Δr is the diffusive displacement. D_o is the molecular diffusion coefficient, which in the runs shown here is constant at $D_o = 10^{-9} \text{ m}^2/\text{s}$. φ_n is the direction of the diffusive displacement at point (x_n, y_n) chosen randomly from a uniform distribution between 0 and 2π . Δt is a constant time step size and set to ensure a maximum dimensionless convective step size of at most 0.01 in the y -direction ($\Delta y/H$) and 0.001 in the x -direction ($\Delta x/L$).

The dispersion coefficient is computed from the spatial variance of the particles at a given time as

$$D_L = \frac{\sigma_x^2}{2t} \quad (\text{A.4})$$

The flow domain consists of five layers of equal thickness and different velocities as in Figure 16. The height of the medium is 1 m. For all cases, we begin with an ensemble (a swarm) of 2000 particles at $x = 0$ and move them to the right (forward flow) or left (backward flow) as required by the case being investigated. The base velocity v was varied from 0.3 ft/day to 0.003 ft/day. In each case, the evolution of spatial variance of the particles (from which the dispersion coefficient is derived) is computed with increasing time (equivalent to mean distance traveled) for both forward flow and reversed flow schemes.

For the case with no diffusion and with $v = 0.3 \text{ ft/day}$, the distribution of particle positions (the concentration profile) at two different times is shown in Figure 17 (a). On flow reversal, the tracer particles retrace their trajectory (on the same streamline) and echo dispersion is zero as shown in Figure 17 (b).

For the same flow rate but with diffusion ($D_o = 10^{-9} \text{ m}^2/\text{s}$), the profiles are in Figure 18. Note that even though the spreading in the transverse direction is because of diffusion alone, the concentration (number of particles/area) is beginning to homogenize in the transverse direction after traveling about 400 m in the positive x direction. On flow reversal, the particles no longer retrace their paths as they return to the inlet. The diffusive jumps cause them to travel on different streamlines on the return path. The large spread of the particles about the inlet indicates large mixing in both transverse and longitudinal directions.

Eq. A-4 above showed how we can summarize the particle positions with a dispersion coefficient. Figure 19 shows the evolution of the dimensionless dispersion coefficient (dispersion coefficient divided by diffusion coefficient) with mean distance traveled. The dimensionless dispersion coefficient increases to an asymptotic value of about 5000 (that is 5000 times larger diffusion) at about 2000 m (Fig. 19).

After flow is reversed from four different distances, the evolution of the echo dispersion coefficient is computed for the swarm as it returns towards the inlet. As they return, the echo dispersion coefficients decrease at first and then stabilize when the swarm nears the original inlet. The larger the travel distance, the smaller is the decrease to the point that when transmission dispersion stabilizes, the echo dispersion does not decrease at all. The echo dispersion coefficients progressively increase with the penetration distance finally reaching the same value as the asymptotic transmission value. The echo dispersion at this distance evidently has no convective component. This very large value (5000) indicates that local mixing is very large.

At smaller distances, the dispersion is still convection dominated (the transmission dispersion coefficient is still increasing). Since the echo dispersion at short distances abruptly decreases immediately on flow reversal there must be a substantial convective component to the transport.

The same simulation was repeated for lower velocities as summarized in Figure 20 where the results are compared at four length scales. Smaller velocities are equivalent to increasing the diffusion coefficient as expected in gas-gas binary flow. The same trend in dispersion coefficient growth occurs but the asymptotic value is reached much closer to the inlet (up to 200 m for the case with slowest velocity). The echo dispersion coefficients compare in the same way, being lower than the transmission values at short distances and equal to it at its asymptotic value. The fact that the echo dispersion coefficients also decrease with decrease in velocity indicates the significance of convection in enhancing local mixing.

This numerical experiment demonstrates that the large echo dispersion coefficients estimated in Mahadevan et al. (2003) are not unreasonable. Irreversible mixing takes place even in large-scale miscible displacements. For this case, the traditional definition of dispersivity does not apply because the dispersion coefficient does not scale linearly with velocity because of the unidirectional nature of the velocity field (Lake and Hirasaki, 1981). With the use of a heterogeneous velocity field, a linear scaling is expected as demonstrated in particle tracking done on pore-network models (Bruderer and Bernabe, 2001).

Summary and Conclusions

- The dispersion coefficient obtained from transmission dispersion experiments has effects of convective spreading and diffusion lumped together. Flow reversal tests (echo dispersion) discriminate between convective spreading and local mixing ("true" mixing). Echo dispersion for the former case approaches zero and in the latter case equals transmission dispersion. Fraction of reversibility of dispersion indicates the degree of local mixing.
- Pore scale simulations show that mixing caused by diffusion is enhanced by the local velocity gradients induced by the grain arrangement and because of splitting of the solute front along sand grains. Local mixing caused by diffusion is irreversible.
- Diffusion is the fundamental mechanism of local ("true") mixing at pore scale.
- In ordered arrangement of disks with no significant variation on flow velocity, a small amount of diffusion is enough to eliminate transverse differences in solute concentration and cause complete irreversibility of dispersion.

- In heterogeneous media local heterogeneity can cause wide variations in flow velocity. Convective spreading dominates transport and high diffusion is required to make the dispersion irreversible.
- Diffusion can cause irreversibility of mixing even at the field scale.

Nomenclature

C	Average concentration, M/L^3
D_0	Molecular diffusion coefficient, L^2/T
D_L	Dispersion coefficient, L^2/T
D_p	Grain diameter, L
L	Length of the medium, L
r	Diffusive displacement, L
T	Time, T
U	Velocity in x-direction (local)
V	Interstitial flow velocity, L/T

Greek Symbols

Δ	Increment
σ	Standard deviation

Superscripts and Subscripts

L	Longitudinal (to mean flow direction)
n	Step index in particle tracking

References

- Aris, R.: "Dispersion of a solute by diffusion, convection, and exchange between phases", Proc. Roy. Soc. (London) A252, 538-50, (1959).
- Bear, J.: *Dynamics of Fluids in Porous Media*, Elsevier, New York, (1972).
- Bruderer, C. and Bernabe, Y.: "Network modeling of dispersion: transition from Taylor dispersion in homogeneous networks to mechanical dispersion in very heterogeneous ones", Water Resources Research, 37(4), 897-908, (2001).
- Coats, K. H., Whitson, C. H. and Thomas, L.K.: "Modeling conformance as dispersion", paper SPE 90390 presented at SPE Annual Technical Conference and Exhibition, Houston, TX, (Sep, 2004).
- FEMLAB Chemical Engineering Module Users Guide, (Oct. 2004).
- Flekkoy, E.G., Oxaal, U., Feder, J. and Jossang, T.: "Hydrodynamic dispersion at stagnant points: simulations and experiments", Physics Review E, Volume 52, Number 5, (Nov. 1995).
- Flekkoy, E.G., Rage, T., Oxaal, U. and Feder, J.: "Hydrodynamic irreversibility in creeping flow", Physical Review Letters, Volume 77, Number 20, (Nov. 1996).
- Hiby, J. W.: "Longitudinal and transverse mixing during single-phase flow through granular beds", Symposium on the interaction between fluids and particles, Institute of Chemical Engineers, London, (1962).
- Hulin, J. P. and Plona, T. J.: "Echo tracer dispersion in porous media" Physics of Fluids A: Fluid Dynamics, 1(8), 1341-7, (1989).
- Jha, R.K., Bryant, S.L., Lake, L.W. and John, A.: "Investigation of pore-scale (local) mixing", paper SPE 99782 presented at SPE Improved Oil Recovery Symposium, Tulsa, Oklahoma, (Apr. 2006).
- Jha, R. K.: *Investigation of Local Mixing and Its Influence on Core Scale Mixing (Dispersion)*, Ph.D. dissertation, The University of Texas, Austin, (2008).
- John, A. K.: *Dispersion in Large Scale Permeable Media*, Ph.D. dissertation, The University of Texas, Austin, (2008).

- Johns, R.T., Sah, P. and Solano, R.: "Effect of dispersion on local displacement efficiency for multicomponent enriched-gas floods above the minimum miscibility enrichment", SPE Reservoir Evaluation and Engineering, Volume 5, Number 1, (Feb. 2002).
- Kitanidis, P. K.: "The concept of dilution index", Water Resources Research, 30 (7), 2011-2026, (Jul. 1994).
- Lake, L. W. and Hirasaki, G. J.: "Taylor's dispersion in stratified porous media", SPE Journal, 21(4), 459-468, (1981).
- Lake, L. W.: *Enhanced Oil Recovery*, Prentice Hall, NJ, (1989). Available through the author.
- Mahadevan, J., Lake, L.W. and Johns, R. T.: "Estimation of true dispersivity in field-scale permeable media", SPE Journal, (Sep. 2003).
- Muzzio, F.J., Swanson, P.D. and Ottino, J.M.: "Mixing distributions produced by multiplicative stretching in chaotic flows", International Journal of Bifurcation and Chaos, Volume 2, Number 1, 37-50 , (1992).
- Rigord, P., Calvo, A. and Hulin, J.P.: "Transition to irreversibility for the dispersion of a tracer in porous media", Physics of Fluids, 681, (May, 1990).
- Rigord, P., Leroy, C., Charlaix, E., Baudet, C., Guyon, E. and Hulin, J.P.: "Reversible and irreversible tracer dispersion in porous media", Journal of Physics, Condens. Matter 2, SA437-SA442, (1990).
- Taylor, G.: "Dispersion of soluble matter in solvent flowing slowly through a tube", Proc. Roy. Soc. (London) A219, 186-203, (1953).
- Taylor, G.I.: *Low Reynolds Number Flows*, The National Committee for Fluid Mechanics Films Released by Encyclopedia Britannica Educational Corp., Chicago, IL, (1972).

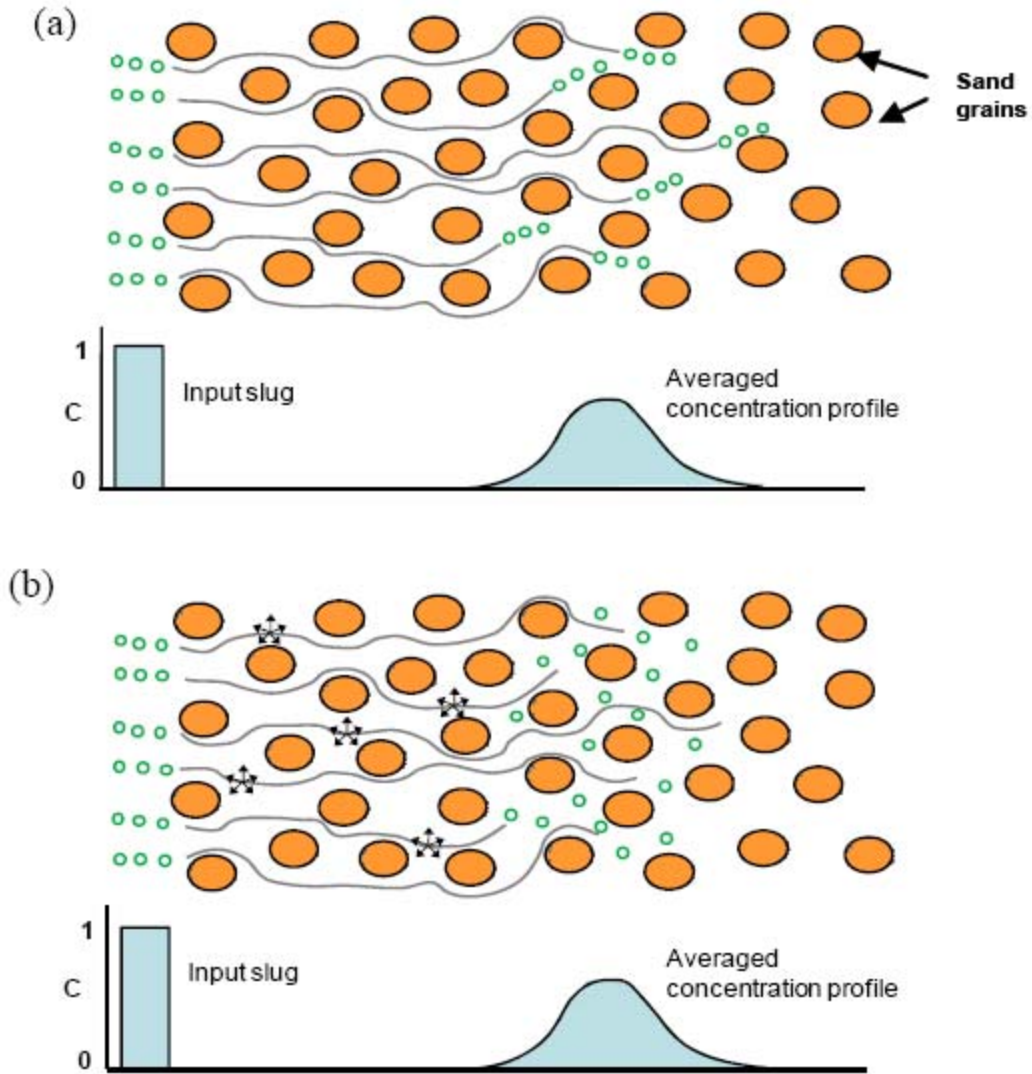


Figure 1: Hypotheses for solute transport and mixing in porous media (a) convective spreading hypothesis and (b) local mixing hypothesis. The averaged concentration profiles are very similar in both the cases. However, their implication towards local mixing is completely different.

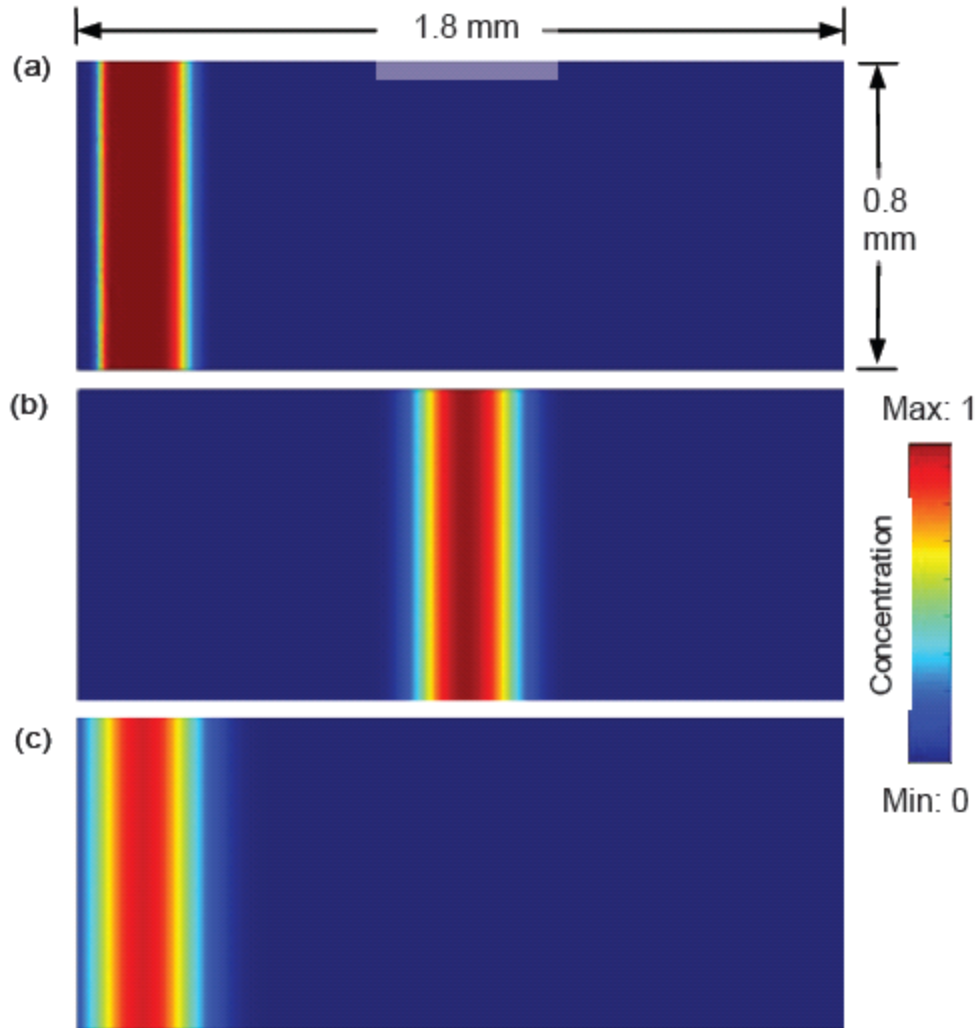


Figure 2: Solute concentration profiles for a plug flow of a solute slug (a) five seconds after injection, (b) at the time of flow reversal and (c) five seconds before exit. The solute slug is injected for 20 seconds. The velocity across the whole cross-section is constant at 10^{-5} m/s. Dispersion is caused by diffusion alone. Upon flow reversal the slug behaves exactly same way it would have done while moving forward. Mixing is irreversible. (1 PV \approx 200 s).

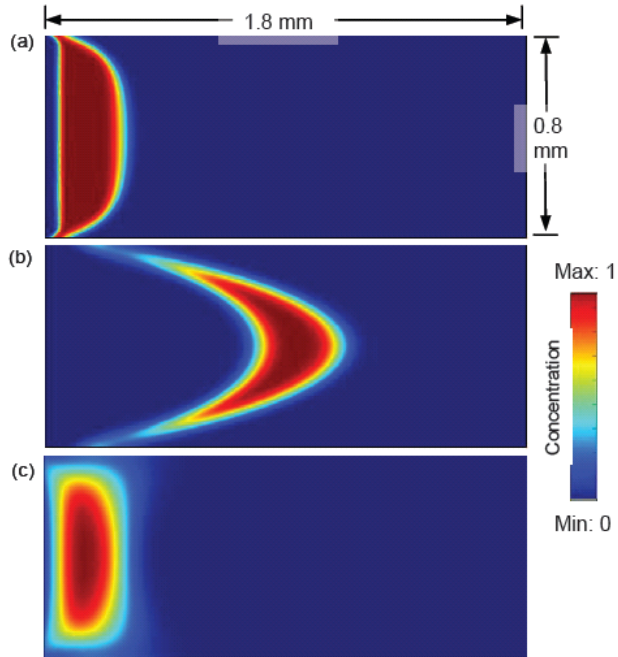


Figure 3: Solute concentration profiles for a slug with parabolic velocity (a) five seconds after injection, (b) at the time of flow reversal and (c) five seconds before exit. Stretching of solute front enhances mixing because of diffusion. However, convective spreading dominates mixing caused by diffusion. Upon flow reversal the convective spreading cancels and dispersion is largely reversible. (1 PV \approx 200 s).

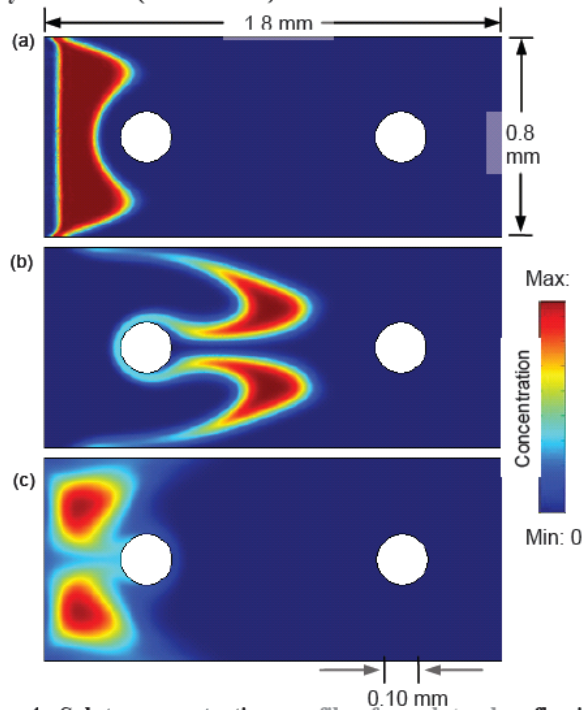


Figure 4: Solute concentration profiles for solute slug flowing around a sand grain (a) five seconds after injection, (b) at the time of flow reversal and (c) five seconds before exit. Splitting around sand grain increases area for diffusion and enhances local mixing. (1 PV \approx 200 s).

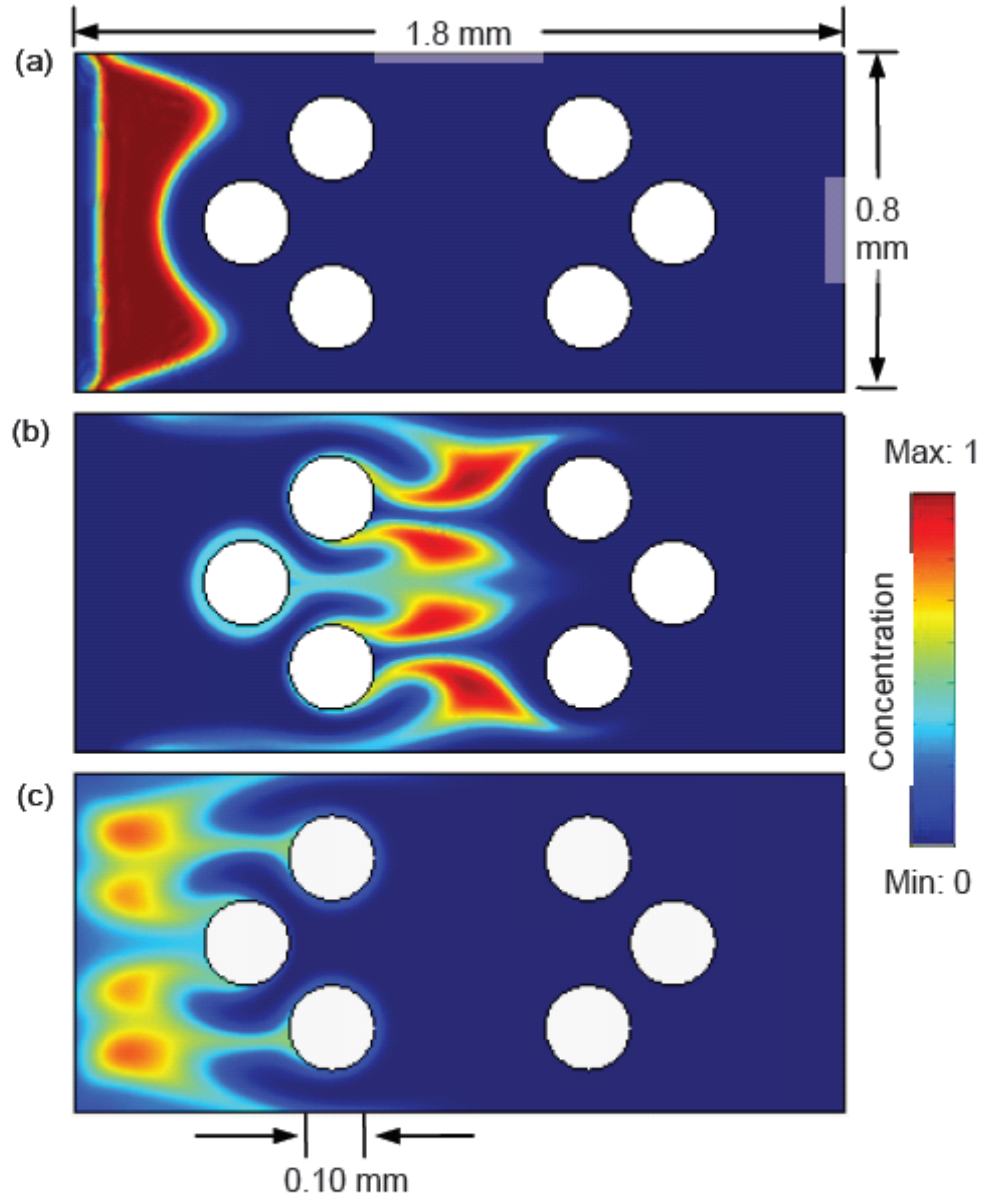


Figure 5: Solute concentration profiles for flow of solute slug around three grains (a) five seconds after injection, (b) at the time of flow reversal and (c) five seconds before exit. More grains correspond to more splitting of solute slug and hence enhanced local mixing and more irreversibility. (1 PV \approx 200 s).

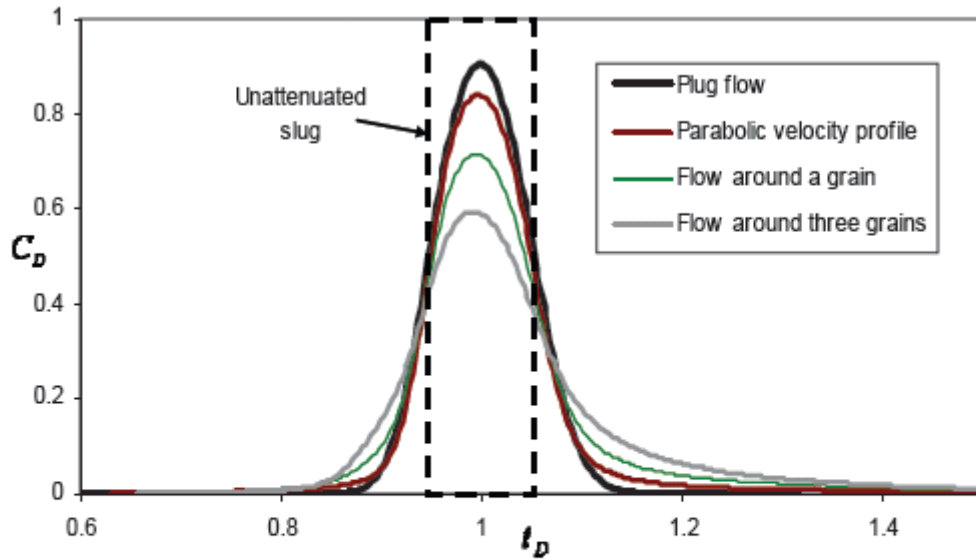


Figure 6: Comparison of backward solute concentration histories at the original inlet ($Do = 10^{-11} \text{ m}^2/\text{s}$). The falling peak of concentration indicates more local mixing.

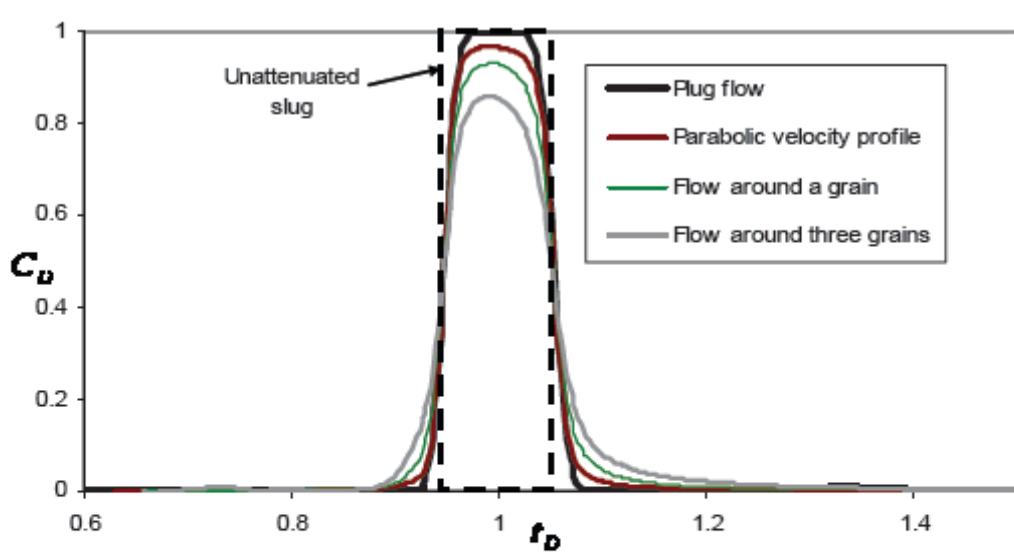


Figure 7: Comparison of backward solute concentration histories with a smaller diffusion coefficient ($Do = 10^{-12} \text{ m}^2/\text{s}$). Less local mixing causes greater reversibility of mixing.

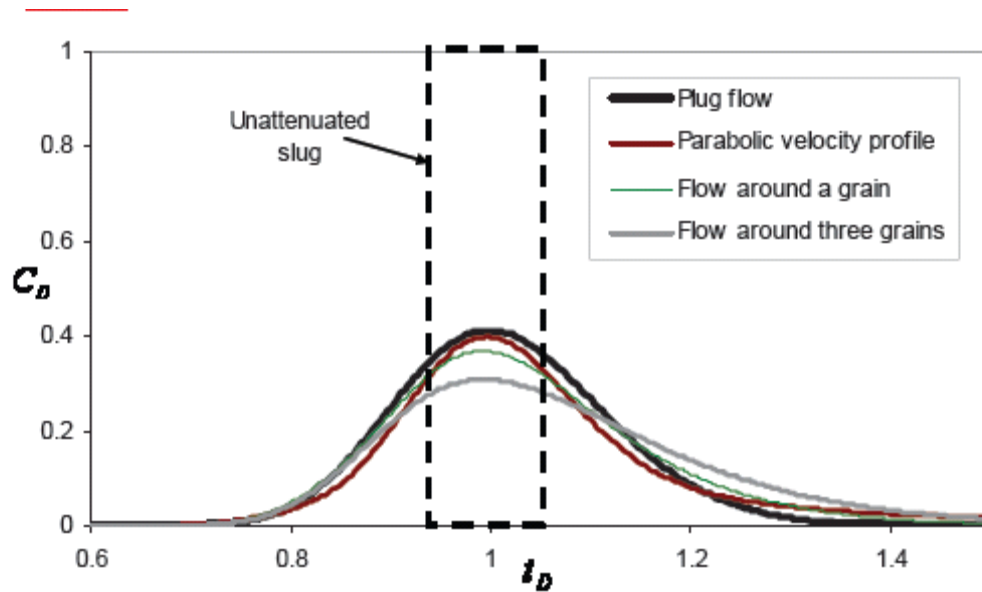


Figure 8: Comparison of backward solute concentration histories with larger diffusion coefficient ($Do = 10^{-10} \text{ m}^2/\text{s}$). Because of irreversibility of mixing, all the curves look same.

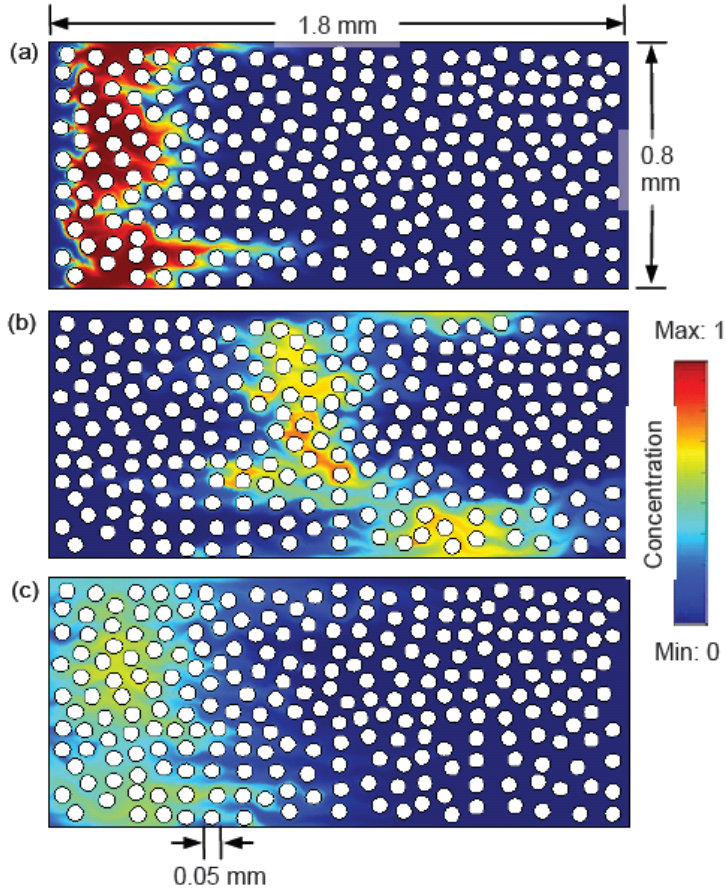


Figure 9: Solute concentration profiles for a slug in irregular arrangement of disks (a) five seconds after injection, (b) at the time of flow reversal and (c) five seconds before exit. Similarity in shapes of concentration profiles in parts (a) and (c) indicate cancellation of convective spreading. (1 PV \approx 110 s).

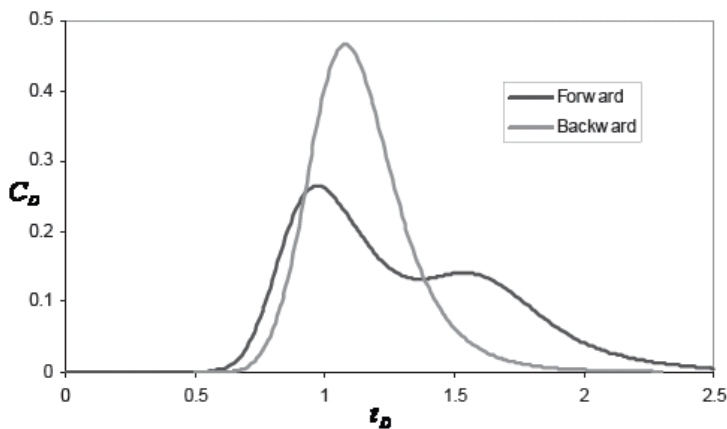


Figure 10: Comparison of solute concentration histories for a slug in irregular packing ($Do = 10^{-11} \text{ m}^2/\text{s}$). Forward curve (at original outlet) is non-Gaussian because of the heterogeneous nature of the medium. The backward curve (at original inlet) on the other hand is Gaussian as it results from local mixing.

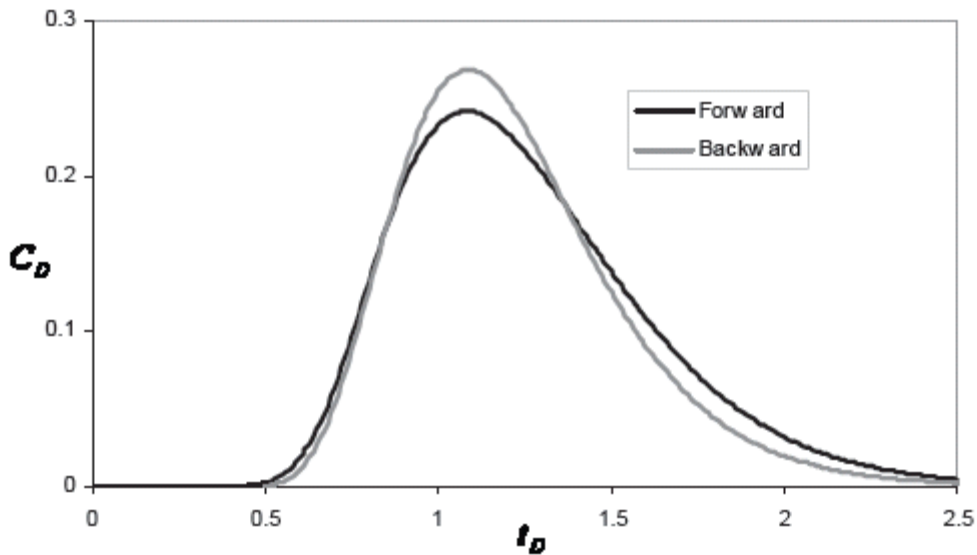


Figure 11: Comparison of solute concentration histories for a slug in irregular packing ($Do = 10^{-9} m^2/s$). Higher diffusion reduces effect of inhomogeneity on mixing. For diffusion dominated processes the forward and backward mixings are the same.

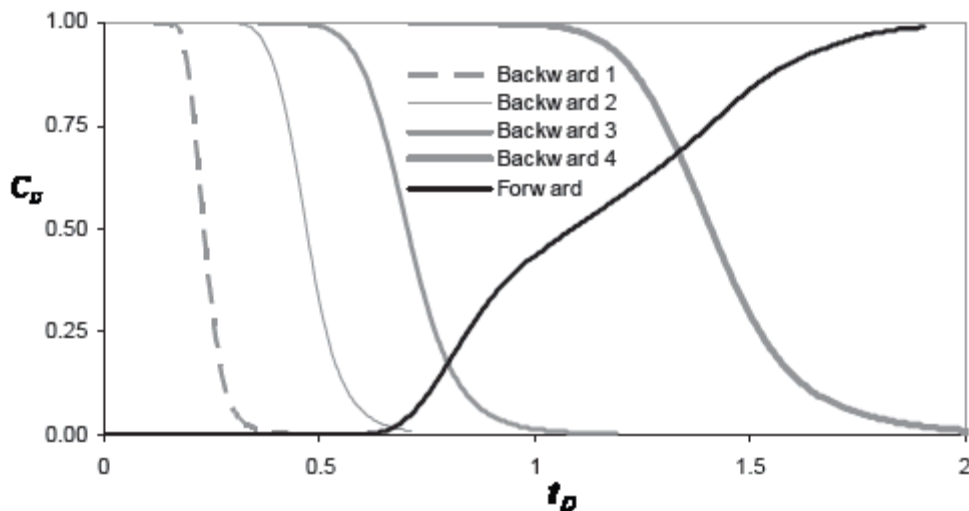


Figure 12: Comparison of backward concentration histories from different penetration depths with the forward concentration history. Forward curve is non-Gaussian. Backward curves are Gaussian. Greater depth of penetration corresponds to greater local mixing and higher irreversibility of dispersion.

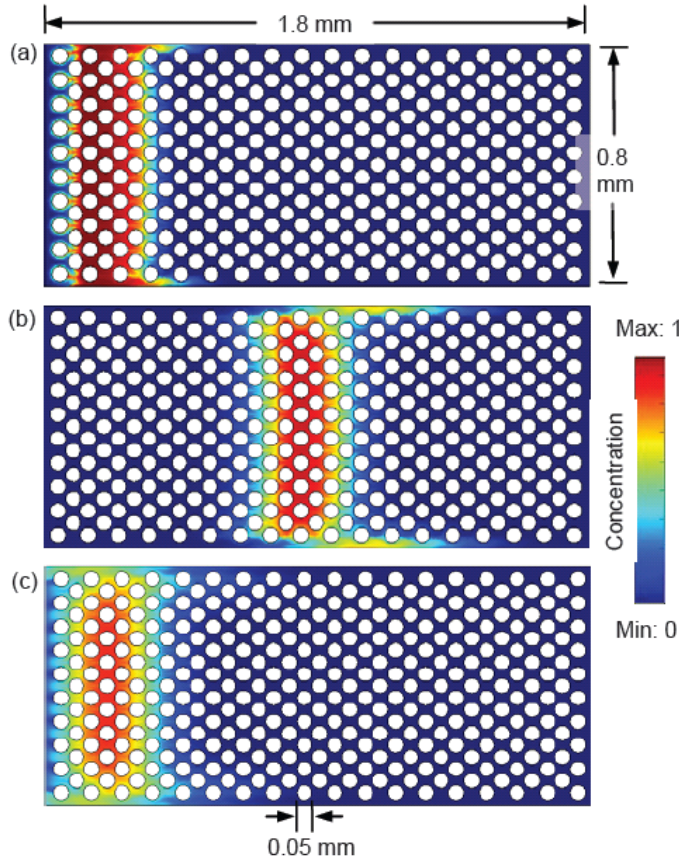


Figure 13: Solute concentration profiles for a slug in regular arrangement of disks (a) five seconds after injection, (b) at the time of flow reversal and (c) five seconds before exit. This process is diffusion-like. The role of solute front-splitting, rejoining and local mixing enhances effective diffusion coefficient. The slug behaves the same way on its way back as it would have done while flowing forward. Dispersion is completely irreversible. For a uniform medium a very small diffusion coefficient is able to homogenize solute concentration in radial direction. (1 PV \approx 110 s).

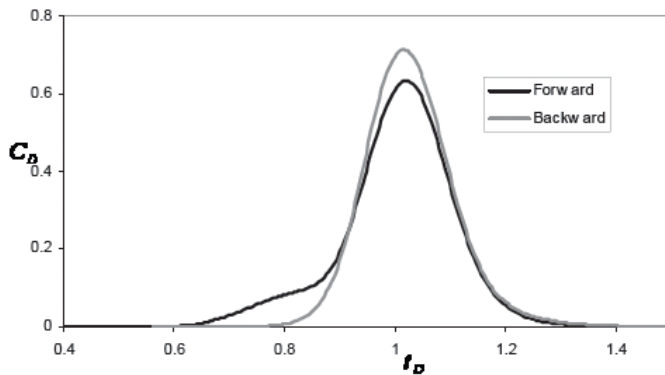


Figure 14: Forward and backward solute concentration histories for flow in a uniform pack ($Do = 10^{-11} \text{ m}^2/\text{s}$). Dispersion is irreversible.

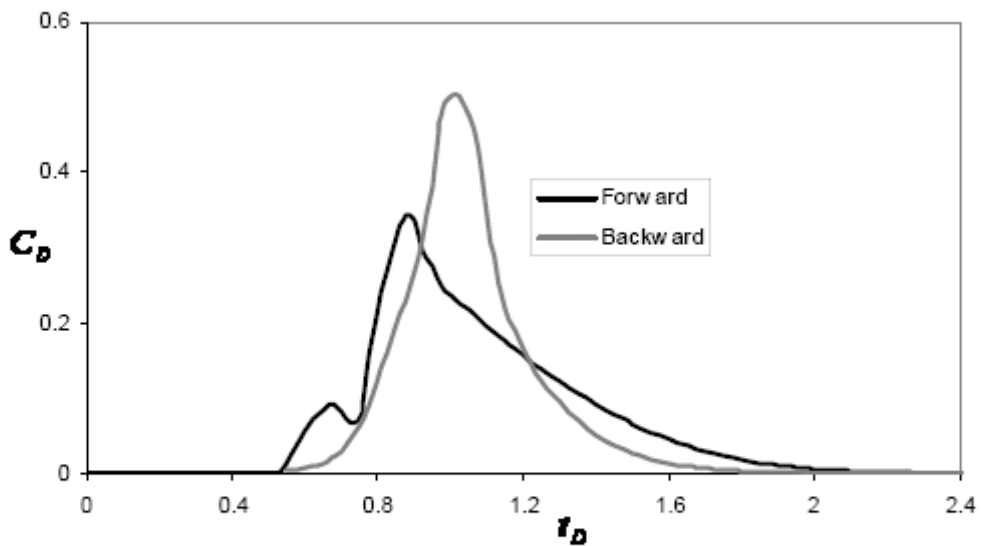


Figure 15: Solute concentration histories for flow in a uniform pack at forty times smaller effective diffusion coefficient. The backward dispersion shows partial reversibility.

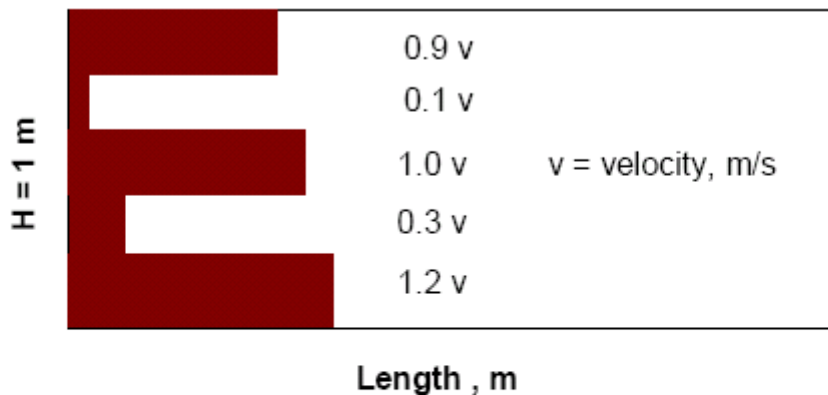


Figure 16: Model for layered flow. The velocity distribution can be changed by changing the average velocity v . Transport is simulated using particle tracking based on convective and diffusive steps. Transverse movements occur because of diffusion only.

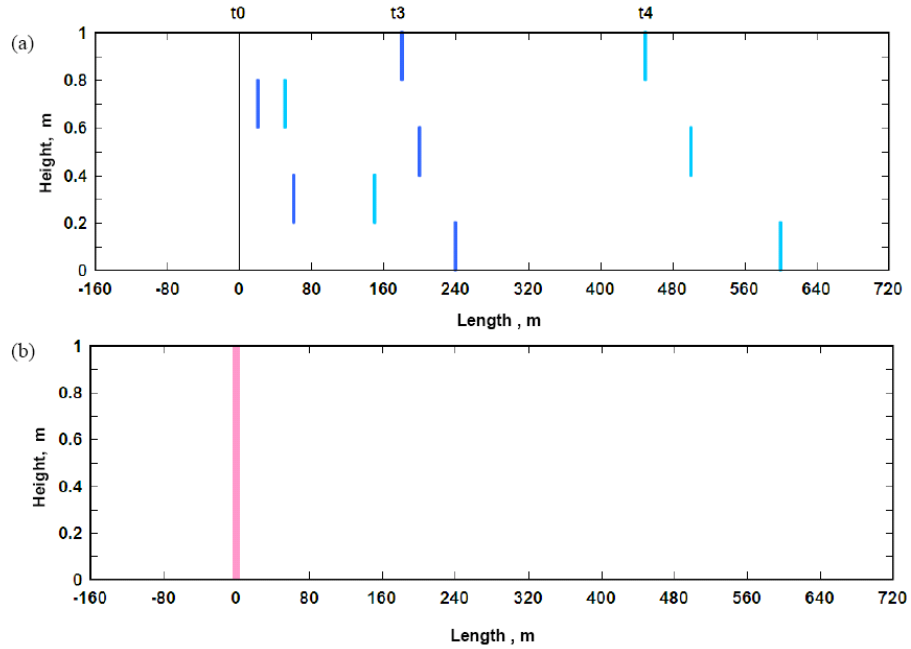


Figure 17. Transport with $v = 0.3 \text{ ft/day}$ and no diffusion. Particle locations plotted at two different times (a) in forward flow and (b) at flow reversal. The system never reaches transverse equilibrium. Echo dispersion is zero.

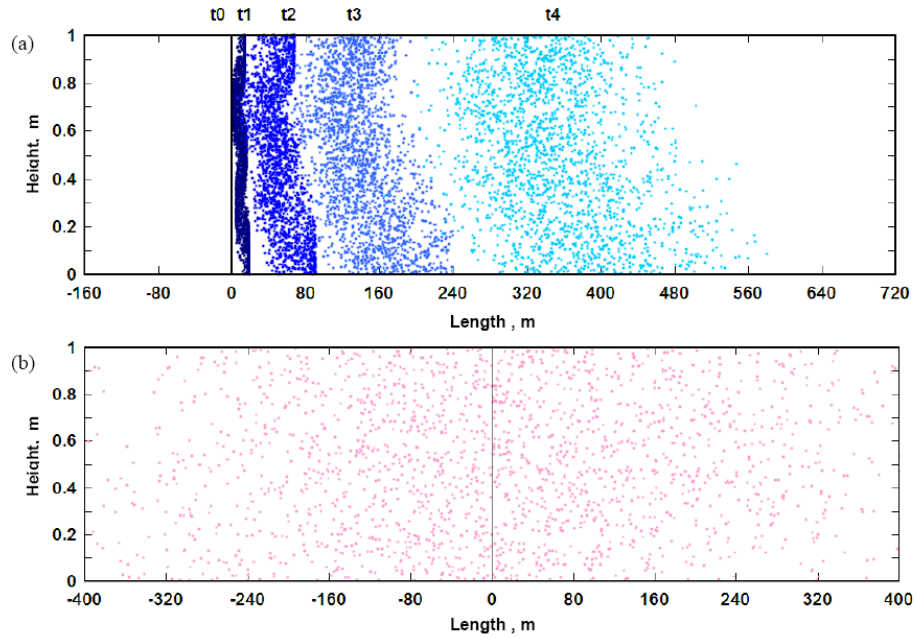


Figure 18: Transport with $v = 0.3 \text{ ft/day}$ and diffusion coefficient $Do = 10^{-9} \text{ m}^2/\text{s}$. (a) Particle locations plotted at four different times showing evolution of spatial variance and (b) at flow reversal (bottom). System is tending to transverse equilibrium under the action of diffusion alone. Echo dispersion is non-zero.

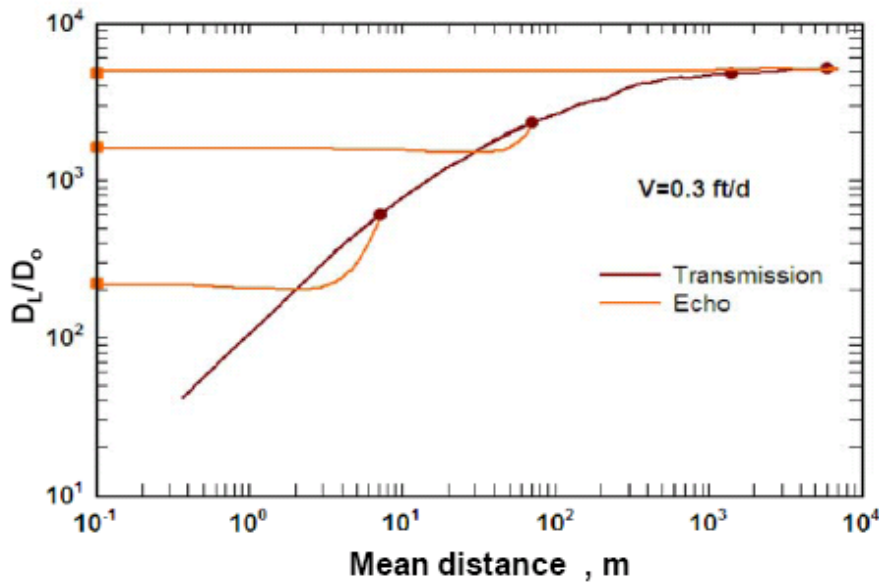


Figure 19: Evolution of dispersion coefficient with mean distance traveled in forward and reverse directions. Dispersion coefficient slowly increases and reaches an asymptotic limit. The echo values increase with penetration distance. Diffusion $D_0 = 10^{-9} \text{ m}^2/\text{s}$.

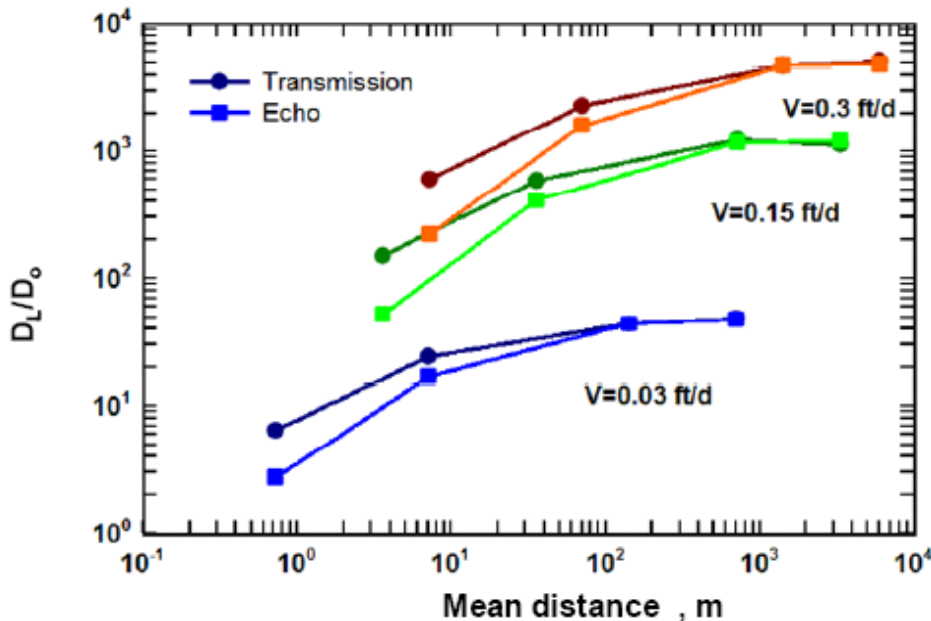


Figure 20: Comparison of forward (solid circles) and echo (solid squares) dispersion coefficients at different velocity ranges. At slower velocities (equivalent to higher diffusion) distance to reach asymptotic limit is less.

Topic 4: Impact of reservoir heterogeneity

Overview of heterogeneity effect

Reservoir heterogeneity in porous media increases oil and gas contact area, hence allow the diffusion to be magnified and ultimately increases reservoir mixing. Correlation length and variation of the permeability distribution are the parameters that affect reservoir mixing. For example considering the permeability distribution for four synthetic reservoir models given in Figure Ov1, where models detail is given in Table Ov1. As it can be observed all reservoirs have the same mean permeability and variations. The only difference is correlation ranges that vary from 250 m in reservoir 1 to 1 m (random heterogeneity) in reservoir 4. We performed tracer test (First Contact Miscible Displacement) on these reservoirs and we analyzed reservoir mixing. Figure Ov2 shows concentration profile at 0.5 PVI and Figure Ov3 shows average reservoir mixing versus traveled distance. Average reservoir mixing is not transmission dispersivity. It is the averaged local mixing over the cross section for various traveled distance. Local mixing is obtained by matching gridblock concentration history to the solution of 1D convection-dispersion equation. Average local mixing approximately estimate true level of mixing and it does not include convective spreading. It clearly can be seen from Figure Ov3 that reservoir mixing increases as correlation range is increased. Since numerical dispersion is equal for all models, this increased reservoir mixing compare to reservoirs 3 and 4 is due to increased fluid contacts that enhances reservoir mixing.

Figure Ov4 shows echo and transmission dispersivity for all reservoirs after the same traveled distance. Echo dispersivities are much smaller than transmission dispersivities for highly correlated reservoirs; however they are about the same for reservoir 4, which indicates that reservoir mixing is complete in reservoir 4. The increased echo dispersivity from reservoir 4 toward reservoir 1 indicates enhanced reservoir mixing due to reservoir heterogeneity.

Mixing due to reservoir heterogeneity:

Total dispersivity in a heterogeneous reservoir model is a summation of dispersivity due to reservoir heterogeneity, numerical dispersivity and physical input dispersivity.

$$\alpha_{tot} = \alpha_{num} + \alpha_{input} + \alpha_{hetro} \quad \Rightarrow \quad \alpha_{hetro} = \alpha_{tot} - \alpha_{num} - \alpha_{input}$$

We performed series of simulation on reservoir 1 by changing numerical and input dispersivity (gridblock dispersivity). In all these simulations we kept reservoir heterogeneity to be constant. Figure Ov5 shows the reservoir mixing versus traveled distance for heterogeneity of reservoir 1. It can be observed that dispersivity due to reservoir heterogeneity only depends on heterogeneity structure of the porous media and gridblock size or input dispersivity does not affect α_{hetro} . This understanding was the main idea to correlate dispersivity based on the heterogeneity and flow parameters.

Figure Ov6 shows a contour map that correlate dispersivity due to heterogeneity to V_{DP} and λ_x . It shows that dispersivity increases as correlation length and permeability variation is increased.

Appropriate gridblock size and reservoir heterogeneity:

We used reservoir models 1 and 4 to find the appropriate gridblock size that can be used to mimic true level of mixing. We upscaled each model by 8x2 and 16x2 gridblocks to one equivalent gridblock. Figure Ov7 shows the fine-scale and upscaled reservoir model and also their concentration profile at 0.7 PVI. Figure Ov8 shows the outlet concentration history or FCM recovery curve for both reservoirs and their upscaled model. As it can be seen from recovery curves and concentration profiles, reservoir 1 has almost the same recovery curve for fine-scale and upscaled model due to large reservoir mixing, however in reservoir model 4 the upscaled model has less recovery due to over mixing. It can be concluded that appropriate gridblock size depends on the reservoir mixing. Large correlation length imply that large gridblock sizes can be used (there is much room for upscaling).

To find the appropriate gridblock size we are required to know the amount of reservoir mixing in advance, so we should be able to estimate reservoir mixing from reservoir heterogeneity and flow parameters. In this study we performed inspectional analysis on a single phase multicomponent system for a first contact miscible displacement **2D** model to find scaling groups that may impact local reservoir mixing.

Inspectional analysis:

Our results indicate that concentration variation depends on 6 parameters and 4 scaling groups.

$$C = C(x_D, y_D, t_D; P_D, u_{xD}, u_{yD}; N_{pe}, N_d, R_L, M^o)$$

where dimensionless groups are:

$$G_1 = N_{pe} = \left[\frac{u_{inj} L}{\phi K_l} \right] \quad G_2 = N_d = \left[\frac{L}{W} \sqrt{\frac{K_t}{K_l}} \right]$$

$$G_3 = R_L = \left[\frac{L}{W} \sqrt{\frac{k_y}{k_x}} \right] \quad G_4 = M^o = \left[\frac{\mu_o}{\mu_s} \right]$$

Dimensionless heterogeneity parameters are:

$$G_5 = \lambda_{xD}$$

$$G_6 = \lambda_{yD}$$

$$G_7 = V_{DP}$$

Reservoir Dimension	512x64x1; 1 m gridblock size in each direction
Mean Permeability	1700 md
Permeability Standard deviation	$\sigma_{\ln k} = 1.0$
Binary correlation length	$\lambda_{x_1} = 1m \quad \lambda_{x_2} = 250m$ $\lambda_{y_1} = 1m \quad \lambda_{y_2} = 5m$
Reservoir-1 = $0.0(\lambda_1) + 1.0(\lambda_2)$	Reservoir-3 = $0.8(\lambda_1) + 0.2(\lambda_2)$
Reservoir-2 = $0.2(\lambda_1) + 0.8(\lambda_2)$	Reservoir-4 = $1.0(\lambda_1) + 0.0(\lambda_2)$

Table Ov1: Simulation model property

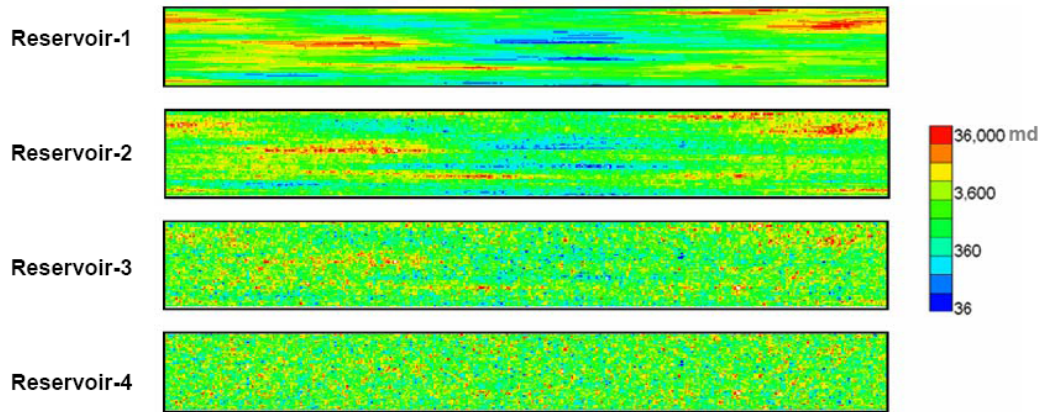


Figure Ov1: Permeability distributions.

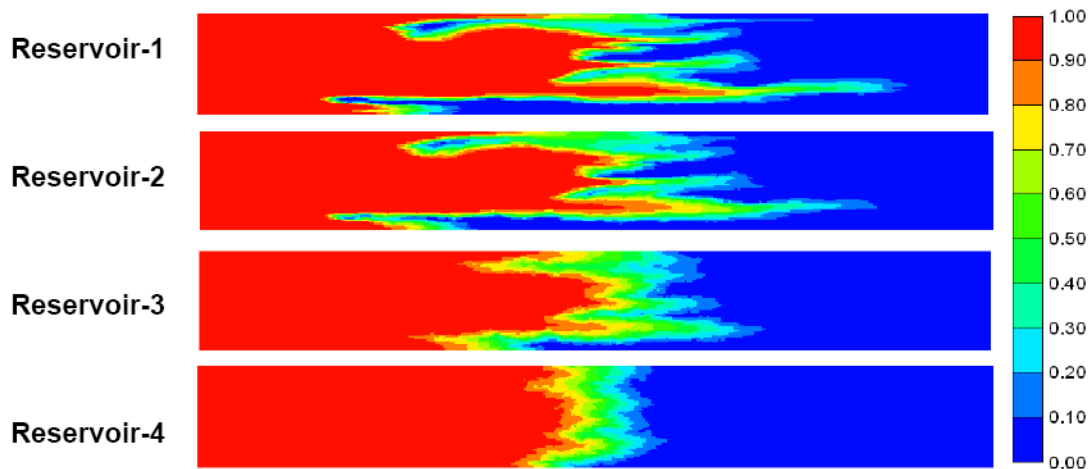


Figure Ov2: Tracer concentration profile at 0.5 PVI.

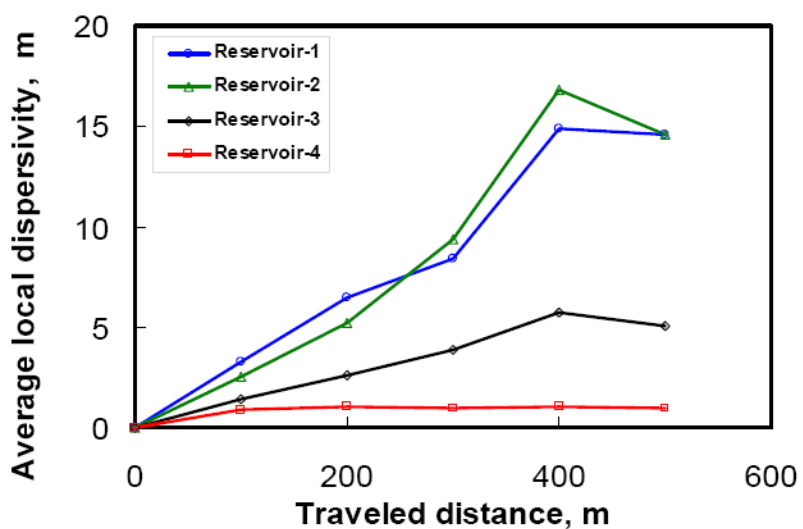


Figure Ov3: Average local dispersivity versus traveled distance for all reservoirs.

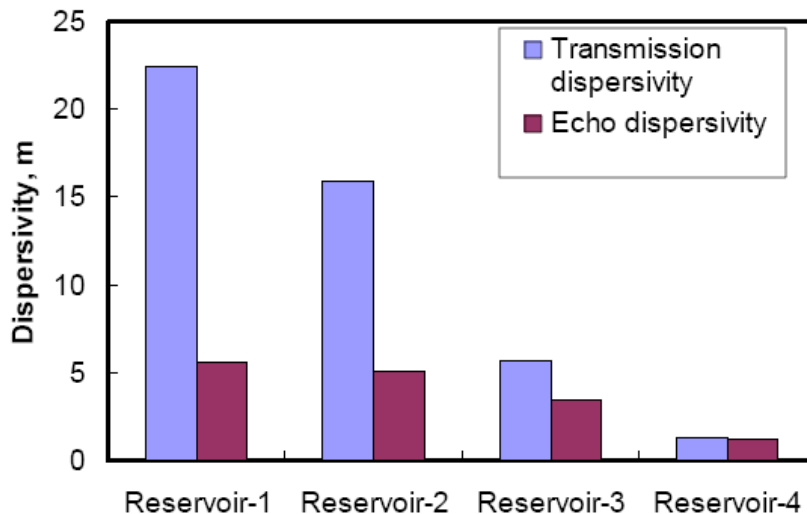


Figure Ov4: Echo and transmission dispersivity at production well. Echo was performed after 0.5 PVI and flow reversal was analyzed at the backward. (Total traveled distance is equal for both estimated dispersivity type)

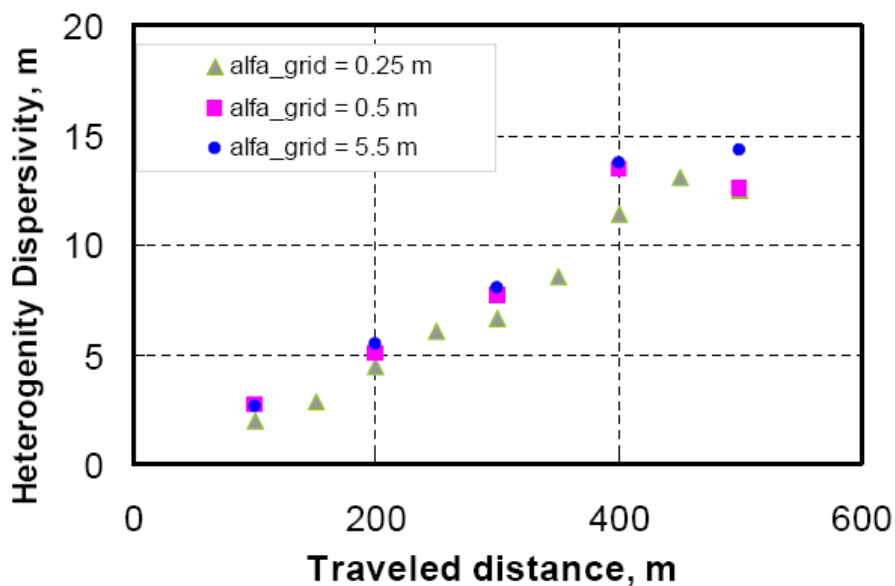


Figure Ov5: Dispersivity due to reservoir heterogeneity for reservoir 1 at different gridblock dispersivity value (physical + numerical).

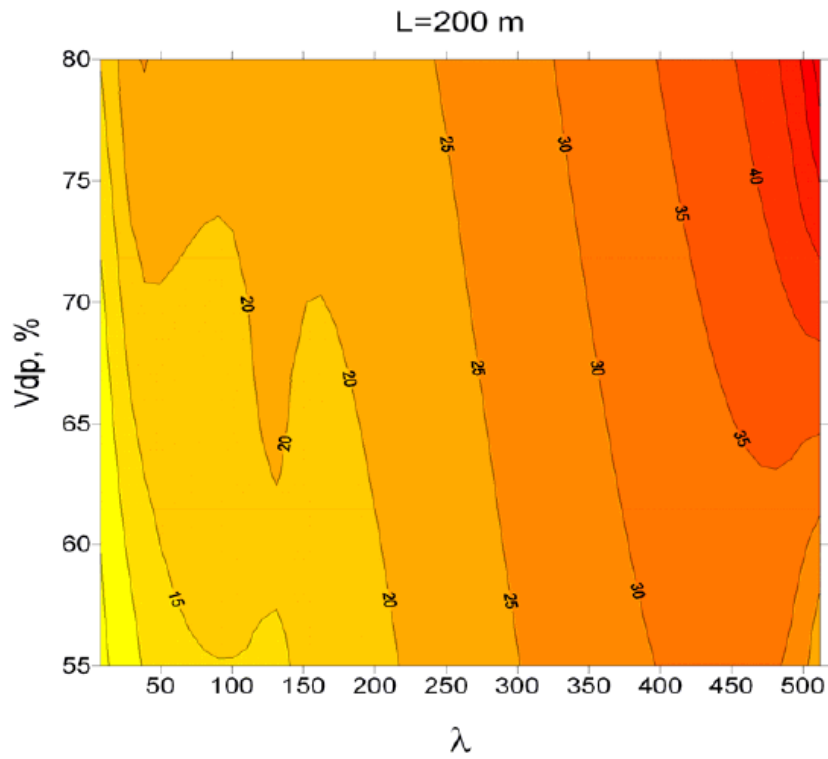


Figure Ov6: Dispersivity contours for various correlation length and permeability variations at traveled distance of 200 m.

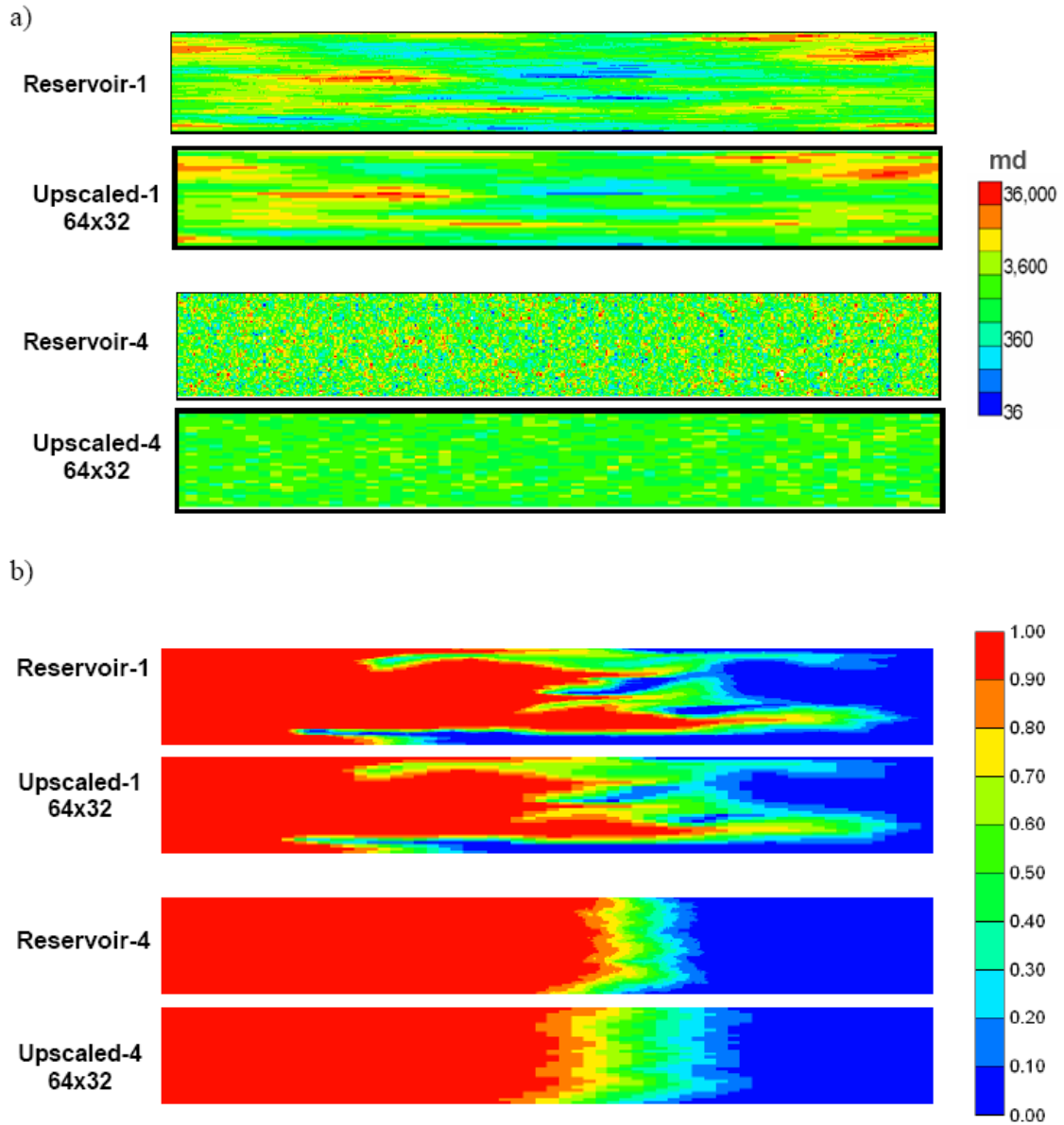


Figure Ov7: a) Original and upscaled permeability distribution. b) Concentration profile at $t_D = 0.7$ in original models and their upscaled model. Models have been upscaled by 8x2.

Analytical and Numerical Investigation of Heterogeneity--Discussion

Mixing of miscible gas with oil in a reservoir decreases the effective strength of the gas, which can adversely affect miscibility and recovery efficiency. The level of true mixing that occurs in a reservoir, however, is widely debated and often ignored in reservoir simulation where very large grid blocks are used. Large grid blocks create artificially large mixing that can cause errors in predicted oil recovery.

This paper examines mixing that occurs in porous media by solving for single-phase flow in a connected network of pores. We differentiate between true mixing that can reduce the effective strength of a miscible gas or surfactant from apparent mixing caused by convective spreading. This work differs from network models in that we directly solve the Navier-Stokes equation and the convection-diffusion equation to determine the velocities and concentrations at any location within the pores. Flow in series and layered heterogeneous porous media are modeled by using many grains in different arrangements. We consider slug, continuous, and partial injection as well as echo tests (single-well tracer tests) and transmission tests (interwell tracer tests). We match the concentrations from the pore-scale simulations to the analytical convection dispersion solution that includes both transverse and longitudinal dispersion coefficients.

The results show that for flow in series and in layers, echo and transmission longitudinal dispersivities become equal and reach an asymptotic value if complete mixing over a cross section perpendicular to flow has occurred. In practice, the asymptotic value of dispersivity may never be reached depending on pattern-scale heterogeneity and well spacing. Transverse dispersion coefficients also are scale dependent, but they decrease with traveled distance. We further demonstrate that the classical Perkins-Johnston relationship between longitudinal dispersion coefficient and fluid velocity is obtained. We conclude that echo dispersivities are reliable indicators of true mixing in porous media.

Introduction

Oil recovery from miscible gas floods is highly dependent on the magnitude of mixing at the field or pattern scale.¹⁻⁴ Mixing acts to drive the composition route further into the two-phase region and away from the critical locus in multicontact miscible floods. Because the composition route moves further away from the critical locus and deeper into the two-phase region, the local displacement efficiency is reduced, in some cases, by nearly half of incremental oil recovery (recovery post waterflood).³⁻⁴ If reservoir mixing is large, good recovery efficiency may require operating at pressures well above the minimum miscibility pressure (MMP) or beyond the minimum enrichment for miscibility (MME).³⁻⁵

Numerical dispersion is also present in reservoir simulations, which can significantly increase mixing when large grid-block sizes are used. Methods that achieve low mixing, such as those used in streamline simulation, may reduce the level of mixing below that which is expected at reservoir scale. Streamline simulations may also not adequately include crossflow between streamlines. It is important to determine the appropriate level of dispersion at reservoir scale so that we can attempt to model it correctly.

Mixing in a reservoir is primarily caused by molecular diffusion of solute (or gas) from one streamline to the next within the pores. Mixing causes dilution of the gas, which can decrease oil recovery. Reservoir mixing is enhanced by any mechanism that increases the area of contact between the gas and the oil, thereby allowing the effects of diffusion to be magnified. This is in essence the cause of scale-dependent dispersion. The longer the distance traveled of a solute the greater the surface area exposed to diffusion and the longer time diffusion has to work. The contact area grows primarily because of variations in streamlines and their velocities around grains and through layers of various permeabilities (heterogeneity). Crossflow, such as that caused by gravity, can also allow for greater mixing when a fluid of different density than the reservoir oil is injected. Mixing can also be enhanced by the effects of other neighboring wells (fluid drift), and by differences in chemical potentials between components in different phases, that is, by phase mass transfer. Drift can increase the contact area between the injection and reservoir fluids, which allows for enhanced mixing by diffusion.

The level of mixing in a reservoir is generally quantified by measuring the dispersion coefficient and its associated dispersivity (for 1-D flow $D_L = D_o + \alpha_L v$). Transmission dispersivities include both actual dilution (mixing) and convective spreading. Convective spreading at the pore scale occurs solely because of solute (or gas) taking different streamlines with varying velocities and arriving at different times to a fixed location. Convective spreading for continuum porous media is caused by flow through layers of differing permeability. Lake and Hirasaki⁶ considered this case and showed that complete mixing across layers occurs when the transverse dispersion number is greater than five. For layered flow with transverse dispersion numbers less than 0.2, transmission dispersion coefficients will never approach an asymptotic limit no matter the distance traveled. The transverse dispersion number is the ratio of the time required for solute to cross the medium longitudinally owing to convection to the time required for solute to cross the transverse direction owing to dispersion.

Measured concentrations are typically made in well-mixed boreholes where differentiation between convection spreading and actual mixing is not possible. Differentiation is only possible when local measurements of dispersion in the reservoir can be made.⁷ Figure 1 illustrates the differences between convective spreading and actual mixing for two levels of diffusion in a reservoir that contains four layers of varying permeability, and hence fluid velocity. The injection well (at the left of Fig. 1) introduces a concentration pulse that travels through the formation according to the velocity in each layer. For zero diffusion (Fig. 1a), there is no actual mixing of injected fluids with reservoir fluids and the concentration pulse travels through each layer without losing its peak strength. Local measurements of mixing (in a given layer) or that measured by an echo test would show one concentration pulse as is illustrated in the concentration profile of Fig. 1a. The concentration profile at the production well (outlet as measured during a transmission test), however, indicates that mixing occurred in the reservoir. This apparent mixing is what we term convective spreading.

When diffusion is present, as it always is, mixing occurs between layers and at fronts (see Fig. 1b). Mixing is enhanced in this case by the increased area of contact between layers. True mixing is not reversible by an echo test, as is shown in the concentration profile of Fig. 1b. True mixing can only be differentiated from apparent mixing by

comparing the overall composition profile (from a transmission test) to local measurements made by an echo test.

When mixing is complete in the transverse direction, mixing zone growth scales with the square root of time. This type of dispersion is Fickian, as opposed to NonFickian. NonFickian dispersion is caused by the presence of convective spreading, and therefore does not scale with the square root of time. Purely convective spreading, such as that indicated in Figure 1a, gives mixing zone growth for layered flow that scales linearly with time. The goal of reservoir engineers should be to understand how much mixing is occurring at the field scale compared to convective spreading because of their different impact on miscible gas and chemical enhanced oil recovery (EOR). Only true mixing causes the effect of strength of a mixing gas to be decreased or surfactant concentrations to be reduced. Because they have different impact on miscible displacement processes. That is the main purpose of this paper.

Mixing is an irreversible phenomenon,⁸ in that flow reversal will not cause the fronts to move back together at the injection well. Thus, echo tests (single-well tracer tests), which reverse flow, measure a level of mixing that is equal to or less than that obtained from transmission tests. This is because echo tests eliminate convective spreading that occurs in a porous media.

Mahadeven et al.⁹ examined single-well tracer tests (echo tests) that were specifically selected because of their small fluid drifts. Dispersivities estimated from those tests were on the order of 2 to 3 ft, substantially greater than laboratory dispersivities of approximately 0.01 – 0.03 ft. Thus, those field tests are a direct proof of the scale dependency of dispersion.

There are hundreds of papers that examine the scale dependence of dispersion for solute transport in homogeneous and heterogeneous aquifers.¹⁰⁻¹¹ A variety of complex dispersivity models and methods have been generated that exhibit scale-dependent dispersion in heterogeneous aquifers. Examples include random-walk models, fractional derivative models, time-dependent dispersivities, and non-local dispersivity models.¹⁰⁻¹³ Transmission dispersion in heterogeneous porous media has been well documented to depend on the permeability heterogeneity (correlation length and standard deviation), aquifer aspect ratio, and diffusion level (solute diffusion in gas versus water).¹⁴ Asymptotic values of dispersivity (Fickian dispersion) have been observed with continuum porous media simulations, and predicted by stochastic modeling studies.¹⁵ In several studies, macro-scale dispersivity are taken as a function of time until constant asymptotic values are reached, depending on the level of heterogeneity.¹⁶⁻¹⁷ Very few papers have discussed measurement of transverse dispersion, but transverse dispersivity is also likely dependent on the pore structure, grain size, and heterogeneity.¹⁸⁻²¹

In this research, we examine both transmission and echo dispersion at the pore scale to illustrate scale dependency of dispersion for a variety of boundary conditions and heterogeneities. We first present the simulation model and the equations that are used to solve for velocities and concentrations within the pores. Next, continuum simulations are performed to examine further the differences between convective spreading and mixing, and to better explain echo and transmission results. We then demonstrate for pore-scale models that the classical Perkins and Johnston dispersion curves are obtained as a function of the pore Peclet number. Unlike previous research, results for more realistic non-uniform, series, and layered pore-scale models are also given. Both two-dimensional

and three-dimensional pore morphologies are considered as well as transverse and longitudinal dispersion coefficients (D_L and D_T). Last, conclusions are presented.

Mathematical Model

We model solute transport for both continuum porous media and pore-scale models using the commercially available code COMSOL.²² When the continuum option is used, velocities and longitudinal/transverse dispersivities for each layer are specified and COMSOL only solves the convection-dispersion equation. Continuum simulations are not the focus of this research, but are used to illustrate spreading and mixing in layered media, as well as to explain the differences between echo and transmission tests.

For pore-scale simulations, COMSOL uses finite-element methods to solve first for the steady-state single-phase velocities in each pore using the Navier-Stokes and continuity equations. After velocities are calculated, solute concentrations are determined by solving the convection-diffusion equation in two or three-dimensions.

Fluid mass balance is described using the continuity equation for steady-state incompressible flow:

$$\nabla \cdot \mathbf{v} = 0 \quad (1)$$

where \mathbf{v} is the pore velocity vector. The simulations are at the pore scale in that grain boundaries are explicitly modeled as no-slip boundaries. No-slip boundaries give zero velocity both normal and tangential to the grain surface. For most simulations, we continuously injected solute at a constant velocity v_{inj} . At the injection boundary there are no grains so that the mean pore velocity must increase within the pores as grains are encountered. Pore velocities can vary significantly over small distances depending on the size of the grains and pores. The pressure at the outlet is constant at atmospheric pressure.

A momentum balance of the fluid is modeled using the incompressible Navier-Stokes equation:

$$\rho \frac{\partial \mathbf{v}}{\partial t} - \mu \nabla^2 \mathbf{v} + \rho (\mathbf{v} \cdot \nabla) \mathbf{v} + \nabla P - \rho \mathbf{g} = 0. \quad (2)$$

For steady-state flow where gravity is also negligible, the Navier-Stokes equation further reduces to

$$\mu \nabla^2 \mathbf{v} = \rho (\mathbf{v} \cdot \nabla) \mathbf{v} + \nabla P. \quad (3)$$

Equation (3) is used in this research where the fluid density is taken to be constant, and therefore independent of concentration.

The solution of Eqs. 1 and 3 give the pore velocities at each node of the finite element model. Typically, we used 20,000 to 100,000 elements to reduce discretization errors to negligible levels. Once pore velocities are determined, the solute concentrations are found by solving the time-dependent convection-diffusion equation:

$$\frac{\partial C}{\partial t} + \nabla \cdot (-D_0 \nabla C + C \mathbf{v}) = 0 \quad (4)$$

where D_0 is the diffusion coefficient of solute in the single-phase fluid and is generally taken to be $10^{-9} \text{ m}^2 / \text{s}$. We typically injected solute over the entire length of the pore-scale model, except as noted in the text. The strength of the solute is set to C_0 at the injection boundary, while the initial solute concentration is zero within the pore-scale

model. Solute flow owing to both convection and diffusion is zero at the top and bottom of the model, as well as at all grain boundaries. Zero diffusive flux is assumed at the outlet.

From Eqs. 1- 4 and the specified boundary conditions, the solution concentrations for two-dimensional pore-scale simulations are functions of six dependent variables, and six parameters. That is,

$$C = f(x, y, t, v_x, v_y, P, v_{inj}, \mu, \rho, D_p, D_o, C_o) . \quad (5)$$

We can combine the parameters to form dimensionless groups. For example, the dimensionless concentration is a function of six dimensionless variables and two dimensionless groups:

$$C_D = f(x_D, y_D, t_D, v_{Dx}, v_{Dy}, P_D; \text{Re}, N_{Pe}) \quad (6)$$

where the dimensionless variables and parameter groups are defined as,

$$C_D = \frac{C}{C_o}; \quad x_D = \frac{x}{D_p}; \quad y_D = \frac{y}{D_p}; \quad t_D = \frac{v_{inj} t}{D_p};$$

$$v_{Dx} = \frac{v_x}{v_{inj}}; \quad v_{Dy} = \frac{v_y}{v_{inj}}; \quad P_D = \frac{P}{\rho v_{inj}^2};$$

$$\text{Re} = \frac{\rho v_{inj} D_p}{\mu}; \quad N_{Pe} = \frac{v_{inj} D_p}{D_o} .$$

The ‘‘pore’’ Peclet number (N_{Pe}) is the ratio of the time for diffusion to cross a distance of one-grain diameter to the time for convection to travel the same distance. Thus, large Peclet numbers imply a convection dominated process.

The Reynolds number (Re) relates inertial forces to viscous forces. Small Reynolds numbers occur in laminar flow, while turbulent flow occurs at relatively large values. In general, Reynolds numbers are small in porous media and flow is laminar. Figure 2 for example shows flow around one circular grain for large and small Reynolds numbers. The results show that all streamlines are reversible for small Reynolds number, but are irreversible for large Reynolds number where inertial effects are more important (see Fig. 3). In this research, we only consider laminar flow so that streamlines are always reversible, regardless of the number of grains and their configuration. Thus, for uniform packing of grains the dimensionless concentrations are only functions of one parameter group, the pore Peclet number. We can still have irreversible dispersion even though streamlines are reversible.

Results from Continuum Simulations

In this section, we illustrate further the difference between convective spreading and mixing using continuum porous media simulations. We consider a ten-layer porous media where the velocities in each layer are constant temporally, but vary in each layer. The velocities vary by a factor of 2.0, where the smallest velocities represent layers with lower permeabilities. Table 1 gives the velocities for each layer, where the first layer corresponds to the bottom layer. Dispersion coefficients are calculated using $D_L = \alpha_L v$. For each layer, the transverse and longitudinal dispersivities are equal and constant at 1.0E-4 m. Thus, the dispersion coefficients in each layer vary by only a factor of 2.0. The dimensions of the 2D model is 1.0 m by 0.25 m. We used 20,000 finite elements to reduce numerical dispersion to negligible levels.

Figure 4a shows the concentration profile at 0.3 PVI (pore volumes injected) for injection of a solvent slug of size 0.125 PVI. The injection well is at the left of the model and the production well to the right. Figure 4b gives the transmission concentration histories for the local concentrations in layer 6 and the overall concentrations averaged over the cross section at $x=0.3$ m. As shown, the local response is less mixed than the overall concentrations, which is similar to the illustration in Fig. 1 for transmission tests. The overall concentrations appear to be well mixed, although in this case there is very little mixing as is evident from the concentration profile (see Fig. 4a). The overall concentration curves for Fig. 4b are clearly nonFickian.

Figure 5a illustrates the same displacement except where the input physical dispersivities are larger by a factor of 100. In this case, the local and overall concentration histories are nearly equal indicating that mixing is nearly complete over the transverse direction to flow. This is clearly evident in the concentration profile of Fig. 5a. Thus, dispersion for this case is Fickian and the level of dispersion (mixing) has reached its asymptotic limit. Once the asymptotic values are reached, dispersivities no longer increase with distance traveled.

Concentration histories from echo tests performed by reversing the flow at 0.3 PVI for the same ten-layer model of Figs. 4 and 5 are illustrated in Fig. 6. As shown, the nonFickian features of the layered model in Fig. 4 are no longer present in the echo concentrations because flow reversal compensates for pore-level convective spreading in each layer. Mixing from the overall concentration history, however, is greater than mixing for the local concentrations (taken at the inlet in layer 6). The greater level of mixing for the overall concentrations is the result of additional mixing made possible by viscous and diffusive crossflow between the layers. For both displacements in Figs. 4 and 5, whether large or small mixing, echo tests give estimates of true mixing for the overall ten-layer model. That is, no differentiation between convective spreading and true mixing is necessary with echo tests for these cases.

Echo tests for a greater travel distance (larger PVI at reversal) than in Fig. 6 show even more mixing from the overall concentration history compared to the local concentration history. This scale dependency results from more time and contact area available for crossflow between the layers when flow is reversed at 0.5 PVI instead of 0.3 PVI. We will show this same scale dependency using pore-scale simulations.

Results From Pore-Scale Simulations

We consider a variety of pore-scale simulations to demonstrate the scale dependence of dispersion.

Homogeneous Models. Consider first a homogeneous packing of spherical grains of size 0.02 mm as shown in Figure 7a. Figure 7a shows the concentration profile in the pore space for continuous injection at about 0.4 PVI. As shown, the level of mixing in this example is small, corresponding to a pore Peclet number of $N_{Pe} = 3$.

The longitudinal dispersion coefficient for the displacement in Fig. 7a is calculated by matching the analytical convection-dispersion equation to the transmission concentrations at the production well ($x_D = 1$). That value along with those calculated using various levels of mixing are plotted in Figure 7b normalized by the diffusion coefficient. As shown, the dispersion coefficient increases with the pore Peclet number. The ratio of D_L/D_0 approaches the tortuosity coefficient for the pore-scale model at small

values of the Peclet number, where diffusion dominates. At large values of the Peclet number, convection dominates and the increase in D_L/D_O with the Peclet number shows the conventional Perkins and Johnston²³ response. The slope, however, for this case is 1.89 instead of the classical 1.1 – 1.3 value for well-packed porous media.²⁴⁻²⁶

The difference in slope is likely the result of uniform grain distribution²⁷ and the large porosity of 61% in our pore-scale model, as well as that flow is two-dimensional here. Jha²⁸ showed that using an irregular grain distribution reduces the slope to about 1.2. The slope also decreases towards the classical range as the porosity is reduced by filling in the pore space of Fig. 7a by adding grains of smaller size (see Figs. 8 and 9). The Peclet number ranges from 0 to 500 for these values. Fig. 10 shows that the slopes decrease further for larger Peclet numbers, as was also observed by Bijeljic and Blunt.²⁹

The echo longitudinal dispersion for displacement of Fig. 7 was calculated by matching the reversed flow concentration at $x_D=0$. The calculated values using various levels of echo dispersion are compared with transmission dispersion and plotted in Figure 11. As shown, the echo dispersion has the same behavior as transmission dispersion in homogeneous uniform grain pack.

Figure 12 shows that the ratio of D_L/D_O decreases linearly with increasing porosity. This is the result of greater mixing in the pores owing to larger velocity fluctuations within the pore-scale model as porosity is reduced. Mixing is also greater when the mean pore velocity is increased owing to greater variations in velocity within the pores as well. When the mean pore velocity v is small, velocity variations within the pores are small, and mixing is primarily the result of diffusion.

Next, we performed transmission tests by continuous injection of solute into the homogeneous and uniform pore-scale model shown in Fig. 13a. The pore-Peclet number for this displacement is 20. We matched the longitudinal dispersivity from the transmission concentrations at various measured distances using the analytical CD solution.³⁰⁻³¹ As shown in Fig. 13b, the calculated transmission dispersivity increases with mean distance traveled, but eventually approaches a constant value (asymptotic limit). Figure 13b also shows the longitudinal dispersivities estimated from the echo tests, where flow was reversed after some mean travel distance into the pore-scale model. Thus, for echo tests, the travel distance out and back is plotted in Fig. 13b. As shown, the echo dispersivities also show scale dependence, but are always equal or less than the transmission values. Echo dispersivities do eventually approach the transmission dispersivities at the asymptotic limit. The echo dispersivities are generally smaller than the transmission values because flow is reversed in echo tests, which eliminates convective spreading caused by variations in streamline paths. The behavior at the pore-scale is similar to what is observed for permeability variations (or streamline variations) at larger scales.^{8, 34}

Consider next the continuous injection of solute, but only in the lower $1/10^{\text{th}}$ of the injection well. The pore-scale model is still homogeneous with uniform grain size and packing as shown in Figure 14a. As shown, the concentrations first move horizontal, but then must move around a grain in a decidedly vertical track. This behavior continues as the solute moves into the pore-scale model. The concentrations were then matched to the 2-D analytical convection-dispersion equation³²⁻³³ for a continuum porous media to obtain the “best fit” longitudinal and transverse dispersion coefficients, see analytical solution below. Figure 14b shows that the transverse dispersion coefficient D_T decreases

with distance traveled owing to the significant initial vertical movement around grains, whereas the longitudinal dispersion coefficient D_L increases somewhat to its transmission asymptotic limit.

Analytical Two-Dimensional CD Solution

We used the following two-dimensional convection-dispersion equation to model both transverse and longitudinal dispersion coefficients in the pore-scale displacements of Figs. 14 and 15:

$$D_t \frac{\partial^2 C}{\partial x^2} + D_t \frac{\partial^2 C}{\partial y^2} - v \frac{\partial C}{\partial x} = \frac{\partial C}{\partial t} .$$

The above equation assumes a continuum porous media and that the mean pore velocity in the vertical (y-direction) is zero, while the mean velocity in the horizontal (x-direction) is constant (see Fig. A). The initial and boundary conditions for the CD equation in an infinite porous media are

$$\begin{aligned} C(0, y, t) &= C_o & -a \leq y \leq a \\ C(0, y, t) &= 0 & \text{all other values of } y \end{aligned}$$

$$\begin{aligned} \lim_{y \rightarrow \pm\infty} \frac{\partial C}{\partial y} &= 0 \\ \lim_{x \rightarrow \infty} \frac{\partial C}{\partial x} &= 0 . \end{aligned}$$

We assumed that the upper boundary of our pore-scale model was not felt during the displacement. This is confirmed from the concentrations at that boundary.

The analytical solution to the above model is given³³ as

$$\begin{aligned} C(x, y, t) &= \frac{C_o x}{4(\pi D_L)^{1/2}} \exp\left(\frac{vx}{2D_L}\right) \int_0^t \exp\left[-\frac{v^2}{4D_L}\tau - \frac{x^2}{4D_L\tau}\right] \tau^{-3/2} \\ &\quad \left[\operatorname{erf}\left(\frac{a-y}{2(D_T\tau)^{1/2}}\right) + \operatorname{erf}\left(\frac{a+y}{2(D_T\tau)^{1/2}}\right) \right] d\tau . \end{aligned}$$

We used only half of the medium in the y-direction of our porous media because of symmetry.

The ratio of D_T/D_L is exactly equal to the ratio of the dispersivities (α_T/α_L) for the pore-scale model when diffusion is neglected. This result takes the pore-scale model as a continuum so that the mean pore velocity in the vertical direction is zero. In Fig. 14b the ratio of α_T/α_L is between about 2.0 to 6.0 instead of the classical values between 0.01 and 0.5 for well packed porous media. The large dispersivity ratio is solely the result of large porosity, in this case around 61%. If the displacements are repeated for smaller porosity and nonuniform grain sizes, the transverse dispersion coefficient is less than the longitudinal value and the ratio is decreased by an order of magnitude to values between

0.1 and 0.5 (see Fig. 15). This is the result of the smaller grains, which are now in the centers of the previously large pores of Fig. 14, blocking movement of the solute in the vertical direction.

Series and Parallel Models. In this section we demonstrate the scale dependence of dispersion that results from series and parallel layers in the pore-scale simulations. Figure 16a shows a parallel model where two homogeneous and uniform grain packs of different sizes are placed on top of each other. The pore-scale model is therefore doubled in height from the previous models. The grain sizes differ by a factor of two in the parallel model, and in the series model.

The results show that there is a large region where crossflow and diffusive mixing takes place between the layers (see Fig. 16a). Figure 16b shows that the echo dispersivities with crossflow increase without bound. When the layers are separate (no crossflow), the echo dispersivities are constant with distance traveled. The echo dispersivities with crossflow do not reach an asymptotic limit in this case because the rate of increase in the length of the crossflow region with time is much faster than rate of diffusive transport of solute across the layers (the transverse dispersion number as defined by Lake and Hirasaki⁶ for this case is less than 0.2). If this trend in echo dispersivities were to continue indefinitely, the dispersivity would be about 0.01 ft for a 3-ft core. Although extending this trend forward is speculative, it does indicate that the level of dispersivity calculated from the pore-scale simulations are consistent with those measured at the scale of laboratory cores. If one would continue the extrapolation even further, the trend is below, but on the order of mixing estimated from single well tracer tests.⁹ More heterogeneous pore models that contain permeability variations at larger scales would give greater echo dispersivities.

Figure 17 shows the concentration profiles for a pore-scale model with series layers or zones. Mixing in the first zone proceeds as if the model were homogeneous. That is, the transmission dispersivities quickly reach an asymptotic limit for this case at about 0.0105 mm (see Fig. 18). The pore velocities in that zone, however, increase prior to reaching the boundary of the next larger grain size zone. This occurs because there is a large pore space immediately in front of the first zone, and the velocities respond to that (i.e. there is no distinct boundary here). The transmission dispersivities, therefore, increase before reaching the second zone. A similar, but opposite effect occurs between the second and third zone. Once the solute is within the second zone, the transmission dispersivities increase to the larger asymptotic limit corresponding to the second layer (the second layer has a pore-Peclet number twice as large as the first layer). The transmission dispersivities in the third zone, however, do not decrease rapidly to the asymptotic limit of the third zone, which is identical to the first zone. That is, the effects of the middle layer are retained for a significant distance into the third zone.

The echo dispersivities in the series model (Fig. 18) have similar trends as the transmission values, but they are sometimes greater than the transmission dispersivities. This is because the middle zone is traversed twice by the echo dispersivities when flow is reversed at mean distances greater than 12 mm. Both the transmission and echo dispersivities in these cases represent true mixing, but over portions of the pore-scale model that were investigated.

Three-Dimensional Model. Consider the homogeneous three-dimensional model given in Figs. 19 and 20. Very few spherical grains are modeled because of the computational time required in the COMSOL simulations.

We calculated the longitudinal dispersivity for the three-dimensional model by averaging the concentrations over a cross section. We compared those estimated dispersivities to the 2-D model shown in Fig. 19b where the injection velocity was kept the same. The 2-D model corresponds to the horizontal cross section through the midpoint of the 3-D model. The transmission longitudinal dispersivities are somewhat greater in the 3-D model than in the 2-D model, likely the result of greater contact area between the solute and the uncontaminated fluid in 3-D. Furthermore, breakthrough of solute occurs earlier in the 2D model owing to differences in porosity (75% in 3D and 64% in 2D). In general, we expect that mixing and dispersivities from 3-D flow should be greater than in 2-D owing to increased contact surface area.

Conclusions

A variety of pore-scale models to demonstrate that dispersivities (or dispersion) is scale dependent. We also defined and explained the differences between convective spreading and mixing. Our main conclusions are

- Pore-scale simulations show similar features as those observed experimentally. That is, the simulations demonstrate the classical Perkins-Johnston relationship between longitudinal dispersion and pore-Peclet number.
- Our results confirm that single-well tracer tests (echo tests) are a more reliable measurement of the true level of mixing that occurs in a reservoir than interwell tracer tests (transmission).
- Both echo and transmission dispersivities increase with distance traveled. They may or may not reach an asymptotic limit depending on the heterogeneities encountered. The scale dependence results from an increase in the contact area between solute (gas) and resident fluid (oil) as heterogeneities are encountered, either at the pore scale or at the pattern scale. Mixing is increased with increasing contact area because the effect of diffusion is enhanced. That is, dispersivity increases as new scales of heterogeneity are encountered.
- Convective spreading is not mixing, but can cause mixing by diffusion to be enhanced.
- Transverse dispersivities are also scale dependent, but decrease with distance traveled. The ratio of the transverse dispersivity to the longitudinal dispersivity becomes small as porosities are reduced in pore-scale models.

Analytical and Numerical Investigation of Heterogeneity--Figures

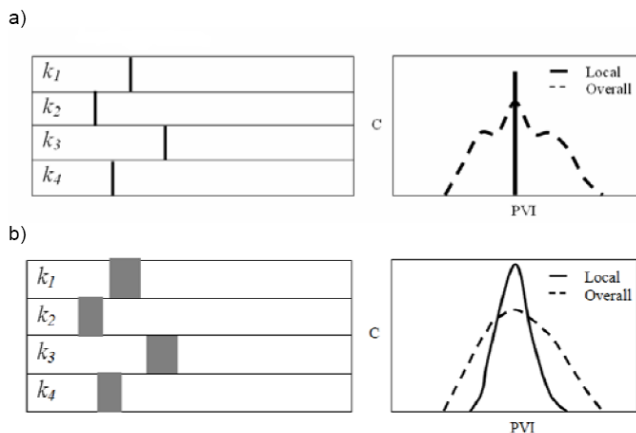


Figure 1: Illustration of the differences between convective spreading and mixing for a four-layered porous media with $k_3 > k_1 > k_4 > k_2$. Convective spreading causes no actual mixing. a) no mixing, b) some mixing.

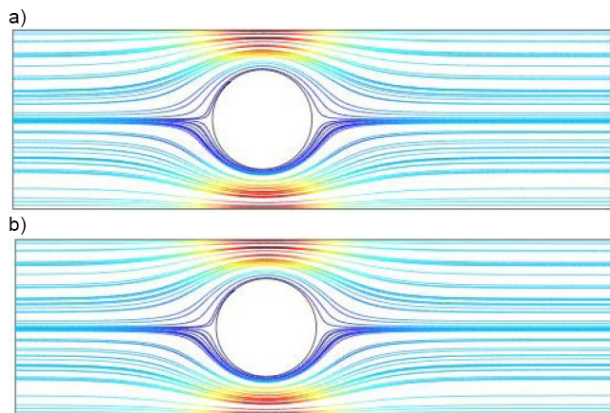


Fig. 2 – Streamlines for flow around one round grain with small Reynolds number, $Re=0.2$, (a) Direction of flow is to the right; (b) Direction of flow is to the left. The streamlines are reversible.

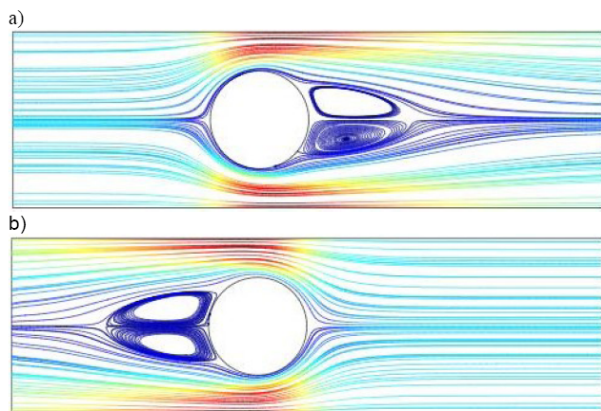


Fig. 3 – Streamlines for flow around one round grain for large Reynolds number, $Re=20$. (a) Direction of flow is to the right; (b) Direction of flow is to the left. Streamlines are irreversible in that flow eddies result owing to large inertial forces.

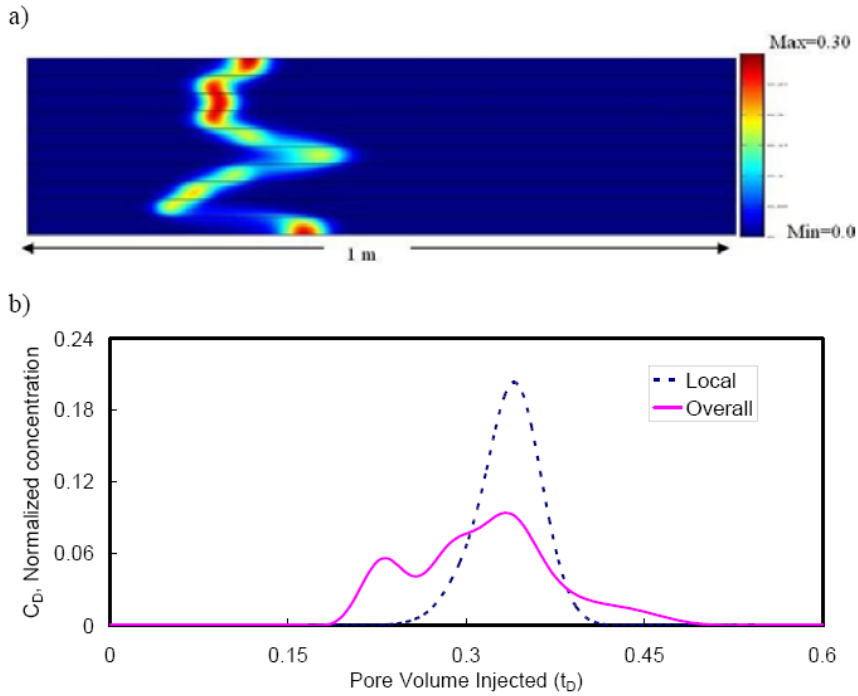


Figure 4: Comparison of transmission concentrations in porous media with ten layers, for the case of small mixing. a) concentration profile, b) concentration histories at $x=0.3$ m. The local concentration is from layer 6.

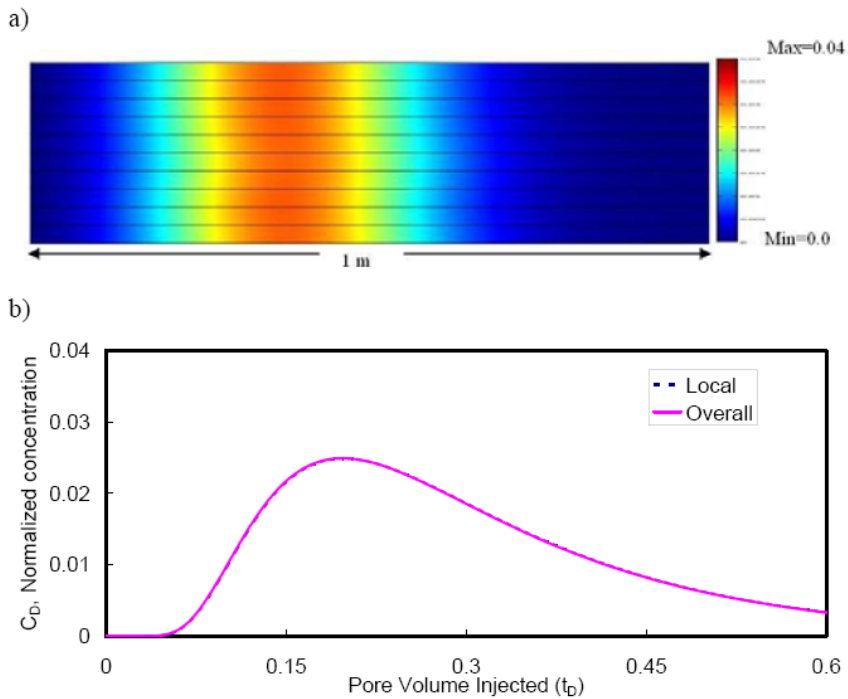


Figure 5: Comparison of transmission concentrations in porous media with ten layers, for the case of large mixing. a) concentration profile scaled to injected concentration, b) concentration histories at $x=0.3$ m. The local concentration is from layer 6.

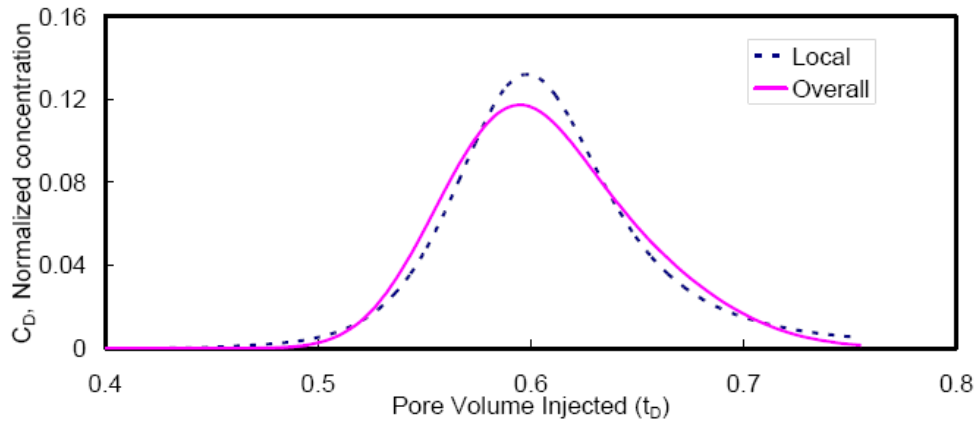


Figure 6: Comparison of local and overall echo concentrations measured at $x=0.0$ m (inlet) for the same model of Fig. 4 when flow reversal occurs at 0.3 PVI. The overall concentration history shows more mixing than the local curve owing to crossflow.

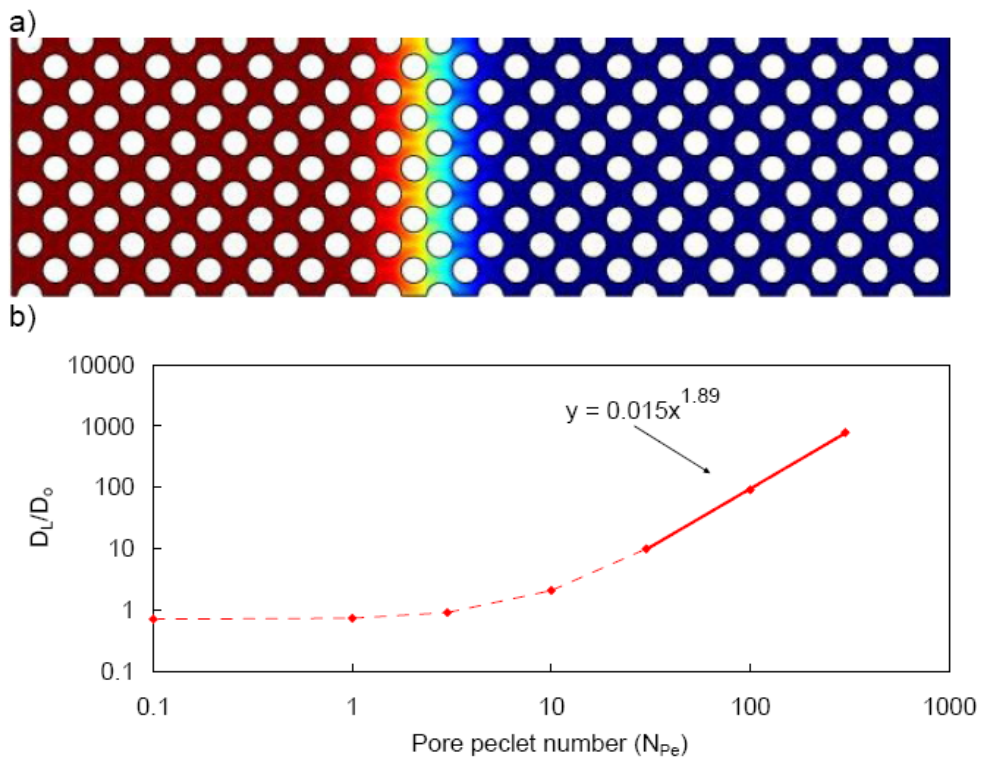


Fig. 7 – Transmission tests in homogeneous pore-scale model with uniform packing and $\phi = 0.61$. a) Concentration profile at 0.4 PVI for $N_{Pe} = 3$, b) Increase in mixing (longitudinal dispersion coefficient) with increasing pore Peclet number for concentrations at production well. The solid line gives the data regressed in the determination of slope.

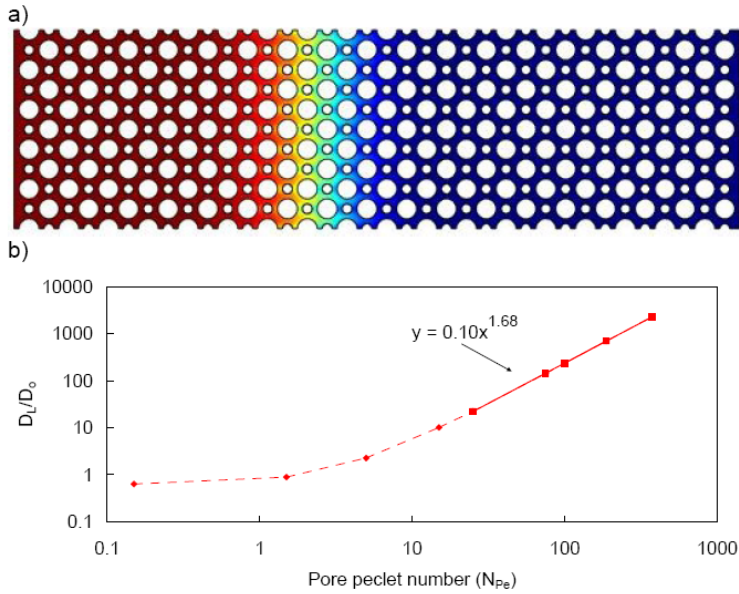


Fig. 8 – Transmission tests in homogeneous pore-scale model with non-uniform packing and $\phi = 0.51$. a) Concentration profile at 0.4 PVI for $N_{Pe} = 10$, b) Increase in mixing (longitudinal dispersion coefficient) with increasing pore Peclet number for concentrations at production well. The solid line gives the data regressed in the determination of slope.

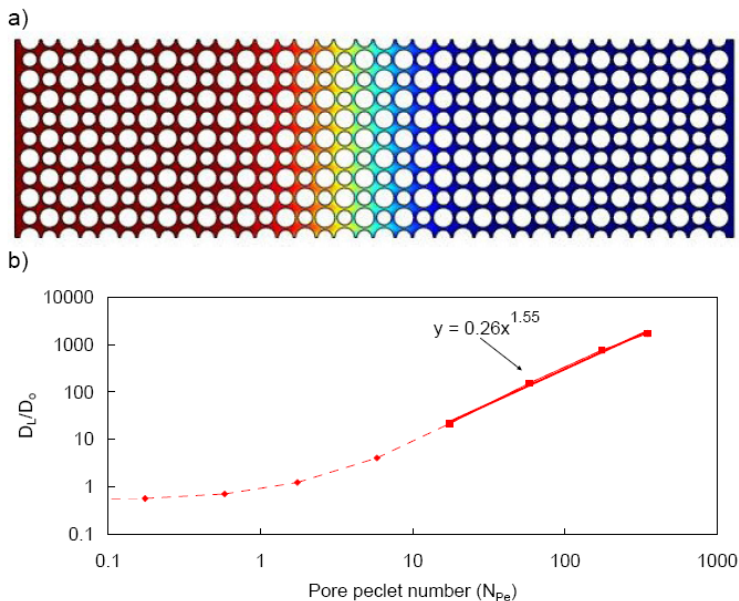


Fig. 9 – Transmission tests in homogeneous pore-scale model with non-uniform packing and $\phi = 0.39$. a) Concentration profile at 0.4 PVI for $N_{Pe} = 10$, b) Increase in mixing (longitudinal dispersion coefficient) with increasing pore Peclet number at production well. The solid line gives the data regressed in the determination of slope.

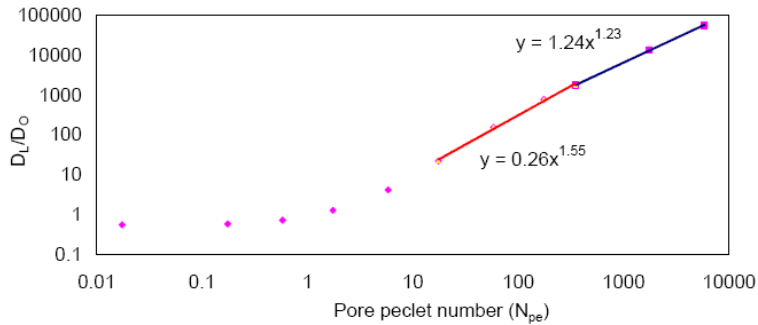


Fig. 10 – Transmission tests in homogeneous pore-scale model with non-uniform packing and $\phi = 0.39$. For $N_{Pe} > 400$ the scaling coefficient decreases further.

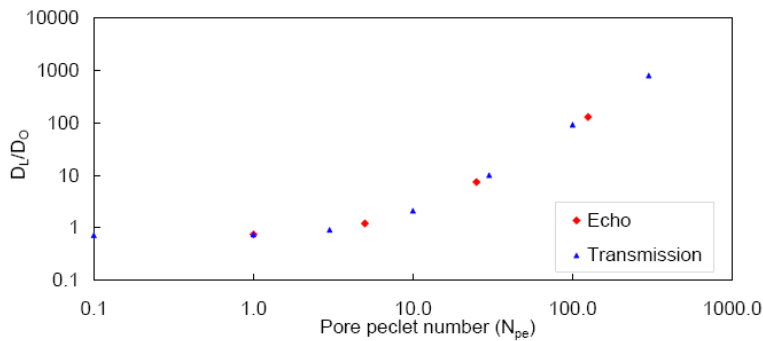


Fig. 11 – Comparison of echo and transmission dispersion for various pore-Peclet numbers.

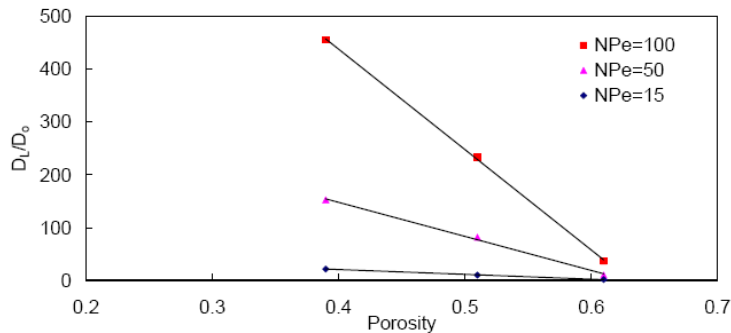


Fig 12- Comparison of the longitudinal dispersion coefficient with porosity and the pore-Peclet number from pore-scale simulations. For fixed pore Peclet number, the dispersion coefficient increases linearly with decreasing porosity.

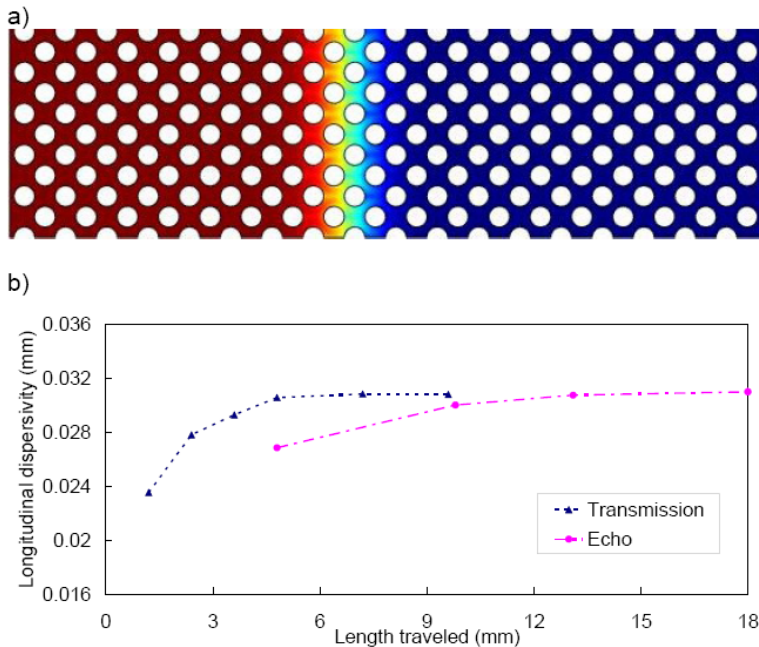


Fig. 13 – Continuous injection of solute across the entire injection well. a) Concentration profile of pore-scale model with uniform packing at 0.4 PVI, and b) resulting echo and transmission dispersivities versus mean distance traveled by the solute.

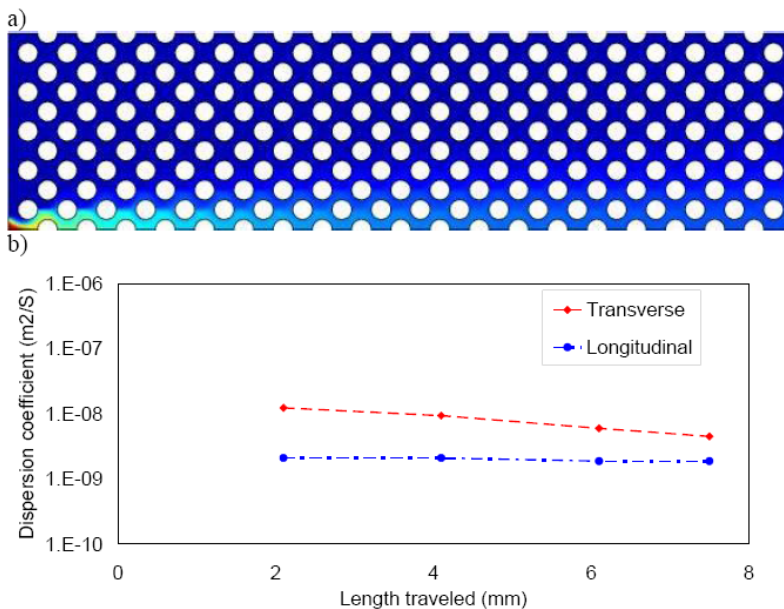


Fig. 14 – Continuous injection of solute in the bottom of the injection well. a) Concentration profile of pore-scale model with uniform packing with $\phi = 0.61$ at 2.0 PVI, and b) resulting transverse and longitudinal transmission dispersivities versus mean distance traveled by the solute.

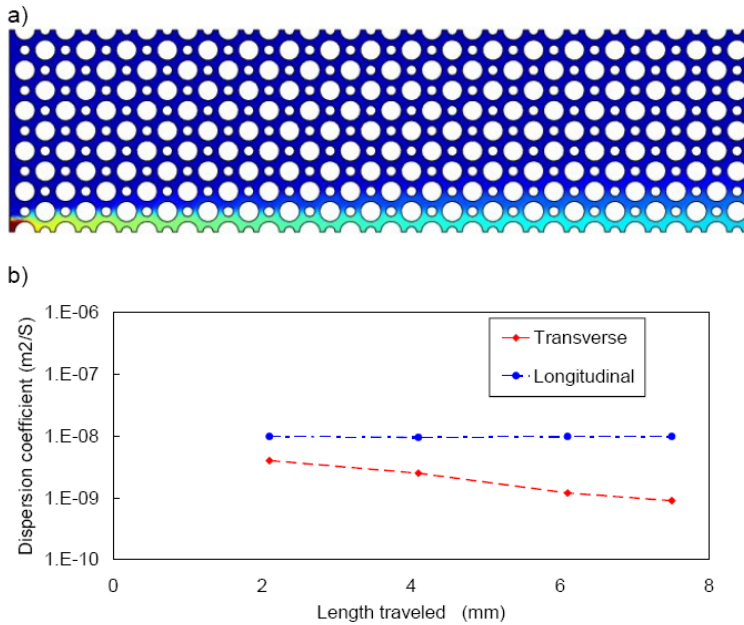


Fig. 15 – Continuous injection of solute in the bottom of the injection well. a) Concentration profile of pore-scale model with non-uniform packing with $\phi=0.51$ at 2.0 PVI, and b) resulting transverse and longitudinal transmission dispersivities versus mean distance traveled by the solute.

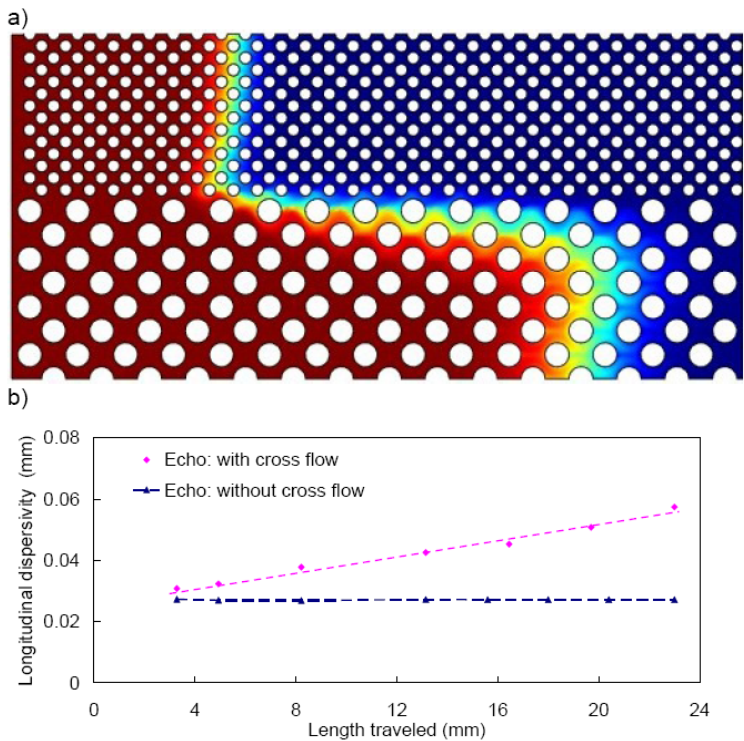


Fig. 16 – Continuous injection of solute across the two-layered pore-scale model. a) Concentration profile of pore-scale model with uniform layered packing at 0.45 PVI, and b) resulting echo longitudinal dispersivities versus mean distance traveled by the solute.

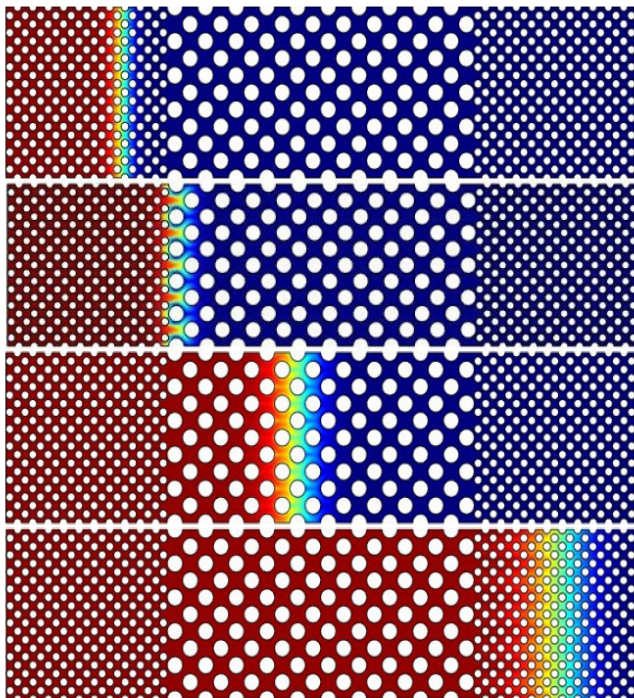


Fig 17 - Continuous injection of solute across a pore-scale model with a series of changing grain sizes. Concentration profiles at four injection times (PVI) are given to illustrate mixing with length traveled.

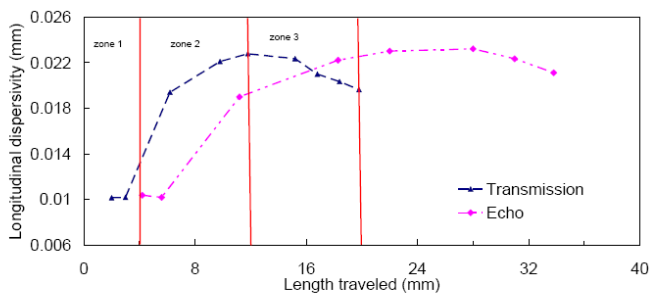


Fig 18 - Continuous injection of solute into the pore-scale model of Fig. 17. Both echo and transmission longitudinal dispersivities increase within the middle region, but decrease slowly at the trailing region.

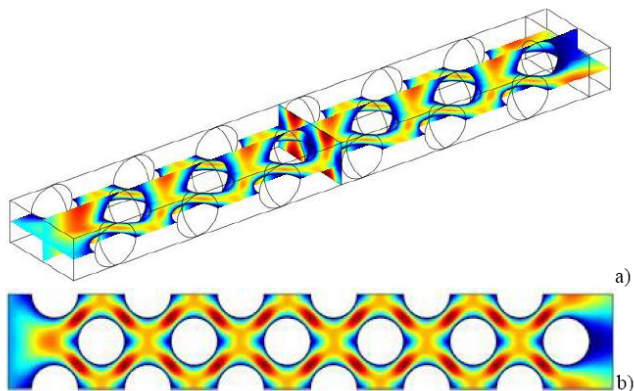


Fig 19 – Pore velocities in a) three-dimensional pore-scale model, and b) in the cross-section at the mid-point of the three-dimensional model.

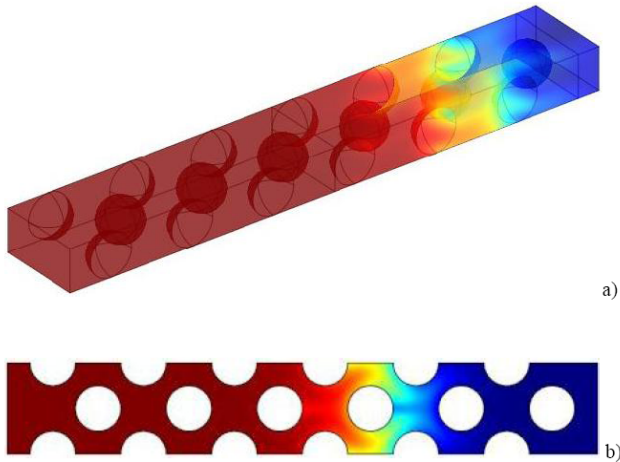


Fig 20 – Concentration profile in a) three-dimensional model at 0.8 PVI, and b) concentration profile for cross-section at the mid-point of the three-dimensional pore-scale model.

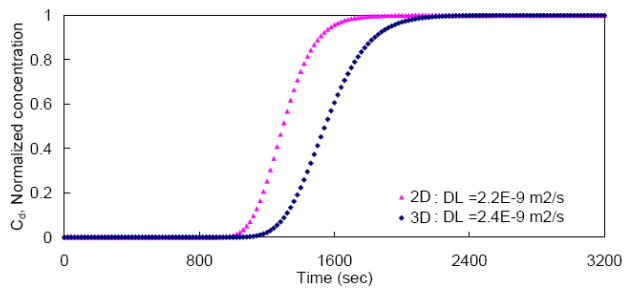


Fig. 21 – Comparison of two-dimensional and three-dimensional concentration histories for models of Figs. 19 and 20, and a two-dimensional model similar to the cross-section of Fig. 18b.

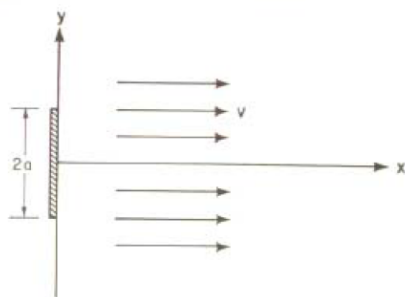


Fig. A – Injection of solute over a distance $2a$ in two-dimensional porous media with a constant velocity v (from [33]). This boundary condition is used with the 2-D CD equation in Appendix A.